Characteristics based Radiative Transfer for Parallel Adaptive Mesh Refinement Hydrodynamics

Dissertation zur Erlangung des Doktorgrades
an der Fakultät für Mathematik,
Informatik und Naturwissenschaften

Fachbereich Physik
der Universität Hamburg

vorgelegt von
Lars Buntemeyer

Hamburg, 2014

Gutachter der Dissertation:	Prof. Dr. Robi Banerjee Prof. Dr. Stefan Dreizler
Mitglieder der Prüfungskommission:	Prof. Dr. Robi Banerjee Prof. Dr. Peter Hauschildt Prof. Dr. Marcus Brüggen Prof. Dr. Günter Sigl Dr. Robert Baade
Datum der Disputation:	16.10.2014
Vorsitzende des Promotionsausschusses:	Prof. Dr. Daniela Pfannkuche
Leiter des Fachbereiches Physik:	Prof. Dr. Peter Hauschildt
Dekan der Fakultät für Mathematik, Informatik und Naturwissenschaften:	Prof. Dr. Heinrich Graener

Characteristics based Radiative Transfer for Parallel Adaptive Mesh Refinement Hydrodynamics

Abstract

We present an algorithm for solving the radiative transfer problem using adaptive mesh refinement and domain decomposition for massively parallel computations. The solver is based on the method of characteristics which requires an adaptive raytracer that integrates the radiative transfer equation. The radiation field is split into local and global components which are handled separately to overcome the non-locality problem. The solver is implemented in the framework of the magnetohydrodynamical computer code FLASH and is coupled to it by an operator-splitting step. The goal is to create a numerical tool that can be used to study radiative effects in the context of star formation simulations which requires a proper treatment of radiation physics that covers both optically thin as well as optically thick regimes.

Zusammenfassung

In dieser Arbeit wird ein neuer Algorithmus vorgestellt, welcher die Strahlungstransportgleichung auf adaptiven Gittern integriert und über die Gebietszerlegungsmethode parallelisiert ist. Der Algorithmus basiert auf der Methode der Charakteristiken, welche die Implementierung eines adpativen Raytracers erfordert. Das Strahlungsfeld wird dabei in eine lokale und eine globale Komponente zerlegt, welche separat berechnet und kombiniert werden, um das Problem der Nicht-Lokalität zu lösen. Der Algorithmus ist im Framework des magneto-hydrodynamischen Computer Codes FLASH implementiert und an diesen gekoppelt. Das Ziel der Arbeit ist es, ein numerisches Werkzeug zu entwickeln, mit dem Strahlungseffekte in Sternentstehungssimulationen studiert werden können, da diese eine angemessene Handhabung von Strahlungstransport sowohl in optisch dünnen als auch optische dichten Regionen erfordert.

Contents

1 Introduction 1
1.1 Motivation . . . 1
1.2 Radiative Processes in Astrophysics . . . 3
1.2.1 Electromagnetic Radiation . . . 4
1.2.2 Radiative Transfer . . . 5
1.3 The Star Formation Process . . . 8
1.3.1 From Molecular Clouds to Stars . . . 9
1.3.2 Circumstellar Discs . . . 17
1.3.3 Radiative Feedback in the Star Formation Process . . . 21
1.4 Numerical Radiation Magnetohydrodynamics . . . 25
1.5 Objectives . . . 29

2 Radiation Hydrodynamics 31
2.1 Radiative Transfer . . . 31
2.1.1 Radiative Quantities . . . 32
2.1.2 Interaction of Radiation with Matter . . . 34
2.1.3 The Equation of Radiative Transfer . . . 37
2.1.4 The Moment Equations . . . 39
2.2 Hydrodynamics . . . 41
2.2.1 Ideal Fluids . . . 42
2.2.2 Euler's Equations . . . 44
2.3 Hydrodynamics with Radiation . . . 47

3 Numerical Methods 49
3.1 Introduction . . . 49
3.2 Characteristics based Radiative Transfer . . . 53
3.2.1 Parameterization and Discretization of the Radiative Transfer Equation . . . 53
3.2.2 Raytracing on the decomposed AMR Grid . . . 57
3.2.3 The Lambda Formalism . . . 59
3.2.4 The Angular Discretization using HEALPix . . . 61

3.3 Numerical Hydrodynamics . . . 63
3.3.1 Hyperbolic Equations . . . 63
3.3.2 Riemann Solvers . . . 65
3.3.3 Godunov's Scheme . . . 65
3.4 FLASH/RT - Coupling the Radiation Solver . . . 68
3.4.1 The Radiation Solver in the FLASH Framework . . . 69

4 Tests 73
4.1 Testing the Radiation Solver . . . 73
4.1.1 Non-LTE 1D Atmosphere . . . 73
4.1.2 Hydrostatic Protostellar Disc . . . 75
4.1.3 Time-Dependent Radiative Transfer . . . 79
4.2 FLASH/RT - Testing the Radiation Hydrodynamics Solver . . . 82
4.2.1 1D Non-equilibrium Radiative Shock . . . 85
4.3 Performance . . . 88

5 3D Collapse Simulations 93
5.1 Collapse without Rotation . . . 94
5.2 Collapse with Rotation and Turbulence . . . 96
5.3 Binary Formation . . . 99
5.4 Summary . . . 101

6 Discussion 111
6.1 The Problem with Time Dependence . . . 112
6.2 The Problem with Energy Exchange . . . 113
6.3 The Problem with Reference Frames . . . 114
6.4 The Problem with the Communication Overhead . . . 116

Appendix A Appendix 121
A.1 Accelerated Lambda Iteration . . . 121

Bibliography 134

1 Introduction

1.1 Motivation

Astrophysics is a unique branch of theoretical physics. In many other research fields, one can more or less exactly design an experiment, which poses a specific question to the physical nature of the object of interest, for instance, quantum physics, particle physics and earth sciences. The theoretical model, on which the experiment is based, is verified by comparing its predictions with observations from the experiment and is either shown to be consistent or has to be modified or even rejected. In Astrophysics, the object of interest is usually very remote. In-situ measurements are very much restricted to our own solar system, and laboratory experiments usually can not resemble the extreme conditions under which astrophysical processes take place. Theoretical models in the field of, e.g., star formation are verified by comparing their predictions with observations, and the astronomer has to ”take what he gets”.

While analytical models are useful to understand the basic mechanisms behind the star formation process, detailed studies require advanced numerical computer simulations to account for a variety of physics involved, e.g., hydrodynamics, magnetic fields, gravity, chemistry and radiative

transfer. Furthermore, these simulations have to cover a wide range of scales in space, density and time since a star is a rather compact, tiny object compared to the interstellar medium (ISM), from which it is formed. The outcome of these simulations is used to generate synthetic observations in the form of, e.g., spectral energy distributions (SEDs), polarization maps, images or spectra. Since the first hydrodynamical numerical simulations of the star formation process by Larson (1969), a lot of advances took place in this field. Especially the subject of disc formation and evolution have become important since they are inextricably connected to the formation of a young star and a potential planetary system. Detailed numerical studies of protostellar and protoplanetary discs gave rise to the development of advanced numerical techniques and computer codes since they require multi-dimensional, magnetohydrodynamical (MHD) simulations on a wide range of length and time scales. Especially the role of turbulence and magnetic fields have been subject to many recent works (e.g. Machida et al., 2010; Seifried et al., 2012), and these authors solved a lot of problems concerning angular momentum transport and the formation of protoplanetary Keplerian discs, which are frequently observed around young stars (Evans et al., 2009).

Radiative feedback processes play another crucial role in the dynamics of star and disc formation. Radiative transfer is the dominant cooling process during the initial stages in which the protostar forms from the gravitational collapse inside a molecular cloud. Later on, when the young star develops significant luminosity from accretion processes and gravitational contraction, radiation determines the thermal structure and stability of the circumstellar disc. Finally, when the evolutionary stage of the star has reached the main sequence and starts burning hydrogen in its interior, the protostellar disc evolves into an irradiation dominated Keplerian disc, from which planets might form.

Despite the obvious importance of radiative transfer, it is often ignored or substantially approximated. The reason is the rather complex nature of radiative processes and their interaction with each other and the thermodynamics of the radiating medium. The radiation field in the limit of geometrical optics is described by an intensity field of 6 dimensions: 3 spatial dimensions, 2 directional + frequency. However, the numerical tool to study star formation is primarily a gravo-MHD code , which solves the equations of hydrodynamics including magnetic fields and self-gravity. Some of the current implementations of such a code (e.g. Stone et al., 1992; Flock et al., 2013; Zhang et al., 2013; Bryan et al., 2014; Bate et al., 2013) include radiative effects in the diffusion limit, which approximates the evolution of the radiation field by the diffusion equation. These codes lack the ability to model radiative transfer properly in the transition

from optically thin to optically thick regimes (Kuiper et al., 2010). But turbulence, accretion processes and disc formation are highly multi-dimensional problems, which require a proper treatment of the anisotropic radiation field in both optically thin as well as optically thick regimes.

In this work we present a new implementation of a radiative transfer solver based on the method of hybrid characteristics (Rijkhorst et al., 2006). The solver is implemented in the modular framework of the MHD code FLASH (Fryxell et al., 2000) and is coupled to it. Since FLASH uses a grid with adaptive mesh refinement (AMR) (Olson et al., 1999) and domain decomposition for parallel computations, the solver has to be integrated into this architecture. The hybrid characteristics method combines long and short characteristics and is able to properly solve the radiation transfer problem in optically thick as well as optically thin regimes and the transition region.

1.2 Radiative Processes in Astrophysics

Nowadays observations are mostly achieved using gigantic optical telescopes (e.g, the VLT), interferometers (e.g., LOFAR, ALMA) or satellites (e.g, Hubble), which can probe different ranges of the electromagnetic spectrum. The spectrum varies over a large range of wavelengths from the very short gamma- and X-rays through the ultraviolet, visible and infrared, into the microwave and radio regime. Understanding radiative processes in the different wavelength regimes has gained enormous insight in many fields of modern astrophysics. Despite the obvious importance of optical astronomy in the visible regime, many fundamental discoveries have involved, e.g., radio observations of quasars and AGNs (Matthews and Sandage, 1963), pulsars (Hewish, 1970) or the famous detection of the cosmic microwave background (CMB) radiation by Penzias and Wilson (1965), X-ray observations of black holes (Bolton, 1972) and infrared photometry of star forming regions (Dullemond and Monnier, 2010).
However, independent of the frequency regime, an observation of an astrophysical object always resembles the outcome from many interacting physical processes, which result in the emission, absorption or scattering of a photon, for instance, a stellar photosphere, a molecular cloud or the CMB. Hence, the information we are interested in is somehow encrypted in the electromagnetic wave we receive with an observational instrument. Decoding this information is the basic motivation of theoretical astrophysics and requires a thorough understanding of radiative processes and the theory of radiative transfer.

1.2.1 Electromagnetic Radiation

Electromagnetic radiation is a phenomenon that shows different behaviour at different scales. In classical mechanics, it is described by the solutions of Maxwell's equations for an electric and magnetic vector field. The solutions represent planar waves propagating at the speed of light and oscillating perpendicular to each other and on the direction of propagation. At the microscopic level of quantum mechanics, light shows particle-like behaviour, which goes beyond the scope of Maxwell's equations. In quantum theory, the electromagnetic field is quantized by photons. The photon is an elementary particle that carries a discrete energy $E = h\nu$ depending on its frequency ν, and it obeys Bose-Einstein statistics. Together with the density of quantum states in an enclosed cavity (a black body) of temperature T, the energy density of electromagnetic radiation in thermodynamic equilibrium is given by Planck's function

$$B(\nu, T) = \frac{2\nu^2}{c^2} \frac{h\nu}{e^{h\nu/kT} - 1}. \tag{1.1}$$

The first factor $\propto \nu^2/c^3$ describes the number of states (standing waves) per unit volume per solid angle per frequency in the cavity. The second factor is a consequence from the quantization of the electromagnetic field, and it describes the energy ($h\nu$) times the occupation number of photons of this energy in the cavity. If we consider the bolometric flux of from the surface of such a black body, which is the total radiative energy emitted by the surface into any direction, we have to integrate Planck's law over all frequencies and obtain the Stefan-Boltzmann law

$$F(T) = \pi \int_0^\infty B(\nu, T) d\nu = \sigma_{\mathrm{SB}} T_{\mathrm{eff}}^4, \tag{1.2}$$

where σ_{SB} denotes the Stefan-Boltzmann constant. If we, for instance, measure the bolometric flux of the sun from a satellite in an earth orbit, we can assign the sun an effective temperature of $T_{\mathrm{eff}} \approx 5780K$, which would be the temperature of the solar photosphere if it would be a perfect black body radiator. This idea stands at the basis of stellar classification.
Planck's law describes the spectral distribution of thermal emission by an idealized black body at temperature T. However, it is not restricted to the ideal case of a closed cavity but can be applied to any system that is in thermodynamic equilibrium, e.g., in the interior of a star, thermal emission by dust or the CMB radiation. Planck's law allows us to assign an effective temperature to any emitting surface that might be approximated by a black body emitter.

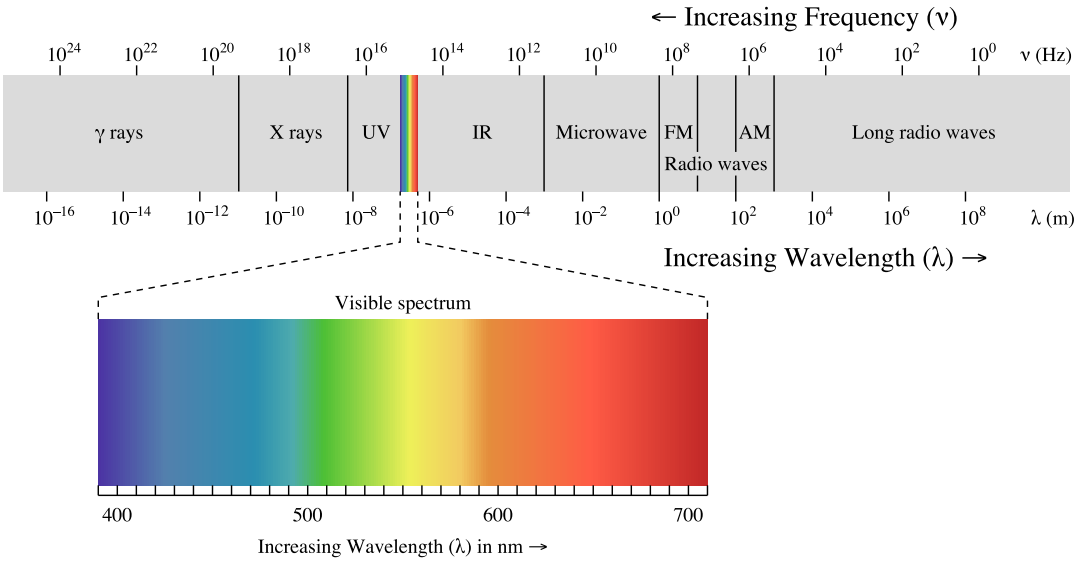

Figure 1.1: The electromagnetic spectrum from the energetic γ-rays to the radio regime with a zoom-in on the optical regime. From http://en.wikipedia.org/wiki/File:EM_spectrum.svg.

Although Planck's law is valid to describe thermal emission, it does not necessarily describe the spectrum of the radiation field itself. Scattering processes (e.g., Rayleigh scattering, Mie scattering or Compton scattering) can significantly change the spectral distribution of the radiation field by the transfer of radiative energy independently of the thermal emission. In a scattering dominated situation (e.g., a stellar atmosphere or Mie scattering on dust grains), matter and radiation are not in thermal equilibrium any more. This requires a proper theory of radiative transfer.

1.2.2 Radiative Transfer

The theory of radiative transfer deals with the transport of energy by the propagation of light through a medium. In astrophysics, the scales on which we deal with radiative transfer are usually much larger than the wavelength of radiation. In this limit of geometrical optics, light propagates along rays and is described in terms of the specific intensity I_ν that is flux per steradian. If we measure, for instance, the flux of the sun on earth and divide it by the solid angle, which the sun covers on the sky, we get the specific intensity, which does not depend on the distance. If we would do the same experiment on Mars, we would receive less flux but at the same time, the solid angle that is covered by the sun would be smaller as well. Since both the flux and the solid angle scale with r^{-2} (where r is the distance), the flux per solid angle stays constant. Consequently, in

vacuum the specific intensity is constant along a ray of direction $\mathbf{n}$ which is expressed by

$$\mathbf{n} \cdot \nabla I_\nu(\mathbf{n}) = 0. \tag{1.3}$$

But in general, as soon as light travels through a medium, we have to take interaction processes into account. In the limit of geometrical optics, interaction processes can be understood as being responsible for removing and/or injecting energy into a ray. If radiation is removed, this is considered an absorption process, and the efficiency is expressed in terms of the photon mean free path l_{free}. The mean free path is usually a function of frequency and depends on the density of the medium. But independently of the complexity of the physics involved to calculate the absorption efficiency, in the theory of radiative transfer this is handled in the form of a macroscopic absorption coefficient, which is an inverse mean free path. This allows to define the optical properties of an interacting medium in terms of the optical depth

$$\tau = \frac{L}{l_{\text{free}}}, \tag{1.4}$$

where L denotes the typical scale of interest. Hence, the optical depth is a geometrical property that measures the number of mean free paths. If we consider the specific intensity entering such a medium of thickness L with an optical depth τ, we can account for the absorbed energy and calculate the intensity that leaves the medium according to

$$I_{\text{out}} = I_{\text{in}}\, e^{-\tau}. \tag{1.5}$$

If the optical depth of the medium were $\tau = 1$, on average 36.8% of the photons would pass the medium without being absorbed. This process is called extinction. If the optical depth is $\tau \gg 1$, the medium is considered to be *optically thick* while in the case of $\tau \ll 1$, it is referred to as being *optically thin*.

If energy is injected into a ray, this is called an emission process, which is handled by the emissivity η_ν. The emissivity measures the radiative flux per solid angle per unit length, which is injected into a ray. Both absorption and emission processes appear as source terms on the right-hand side of Equation (1.3) to guarantee energy conservation:

$$\mathbf{n} \cdot \nabla I_\nu(\mathbf{n}) = \eta_\nu - \chi_\nu I_\nu, \tag{1.6}$$

where χ_ν is the frequency-dependent extinction coefficient. It does not only account for "true" absorption processes, in which a photon is in fact destroyed by some interaction process, but any process that can change the direction of propagation of a photon. This means that also scattering processes are effectively handled as extinction processes although the photon is not truly absorbed. But since scattering does remove a photon from a ray of a certain direction and adds it to another one, it acts as an effective contribution to the extinction coefficient and the emissivity.
Formally, the time-independent radiative transfer equation (RTE, 1.6) can be solved if χ_ν and η_ν are known. However, absorption of radiation crucially affects the thermodynamical state of the medium, which in turn determines opacities and emissivities, which we do not know in advance. Radiative cooling processes (e.g., cooling by dust), quantum states (occupation numbers) of atoms and molecules or the chemistry and ionization physics of the ISM crucially depend on the thermodynamical state of the matter and hence on the radiation field. This makes the solution of the RTE already quite challenging, even if the medium is locally in a thermodynamic equilibrium (LTE). But even if the temperature structure of the medium is known, the radiation field might not only be determined by thermal emission but also by scattering contributions. If the mean free path of a photon is significantly larger than the scale on which the temperature changes, the radiation field decouples from the local thermodynamical properties of the medium. In this non-LTE (NLTE) situation, the radiation field can transport energy over large distances and affect the medium globally.
Another complexity of radiative transfer theory is the high dimensionality of the radiation field. The complete description of the scalar field of specific intensities requires 6 dimensions: 3 spatial dimension, 2 directional + frequency. To describe the radiation field completely, one has to consider incoming radiation from the whole 4π-sky at each point in space in the frequency range of interest. E.g., one has to deal with an enormous amount of data to observe the complete CMB radiation that is collected by instruments like WMAP or Planck only for a restricted frequency range from our point of view at the Earth.
Further complexities arise from the large propagation speed of light ($c \approx 2.998 \times 10^{10}\,\mathrm{cm\,s^{-1}}$) if radiative transfer has to be solved in parallel with the hydrodynamics of the medium. The timescale of radiative transfer is usually much shorter than the timescale of, e.g., hydrodynamics, chemistry or ionization physics. One the one hand, this means that radiative transfer can often reasonably be treated as being time-independent if considered on large timescales (as implied by Equation (1.6)). On the other hand, this makes the transport of energy by radiation a highly non-local process, which has to be solved implicitly together with the equations of hydrodynamics.

Despite or maybe even because of all these complexities, the solution of the RTE with multi-dimensional computer simulations gave rise to a variety of different numerical techniques. Radiative transfer has been playing a substantial role in the modelling of, e.g., synthetic stellar and planetary spectra or SEDs of young stellar objects (YSOs) and circumstellar discs. These models require a thorough understanding of LTE and NLTE radiative transfer as well as continuum and line transfer and the time dependence of the radiation field.

1.3 The Star Formation Process

How stars are being formed in detail is one of the most challenging questions in modern astrophysics. Stars are the key (baryonic) constituent of the universe standing at the basis of large scale structures like our own Milky Way. Galaxies containing up to a few 10^{11} stars form clusters and superclusters, which make up the large scale filamentary cosmic web. In our own galaxy, stars and star clusters show ages on a wide range of time scales from a few million years to very old clusters observed in the galactic halo. The oldest of these clusters have ages on the order of the age of the universe itself (e.g., $\sim 10^{10}$ years), indicating that star formation has been taking place since very early times and is still continuing. Looking at much smaller scales, it seems more and more likely that stars typically host planetary systems as increasing confirmed observations of extrasolar planets indicate (exoplanet.eu). The formation of planetary systems seems to be a natural "side effect" of the formation of a host star and its circumstellar envelope and disc and is therefore inextricably connected to the star formation process itself.

Stars have a profound effect on the ISM, from which they are formed. Since stars burn hydrogen in their interior and produce heavier elements, they enrich the ISM's metallicity by stellar winds or supernova explosions. Stellar radiation heats the ISM and thus determines its thermodynamic properties, and stellar outflows and jets during the the birth of a star inject large amounts of kinetic energy into the ISM. The life and death of stars therefore directly influences the oncoming generation of new stars. which form from an ISM that is crucially determined by the feedback of passed generations.

Although the general nowadays picture of the star formation process made significant advances in the last decades (e.g., since the first computer simulations of Larson (1969)), the detailed processes are still rather poorly understood due to both observational and theoretical constraints. On the one hand, YSOs in the early Class 0 phase are difficult to observe since they are mostly embedded in dusty envelopes, which remain after the initial formation of the YSO. Though

the ISM consists only of a small fraction of cosmic dust (about 1%), it is the main source of continuum opacities in the optical regime. Dust absorbs the main fraction of the primary YSO's emission and reprocesses it into longer wavelength regimes. Therefore, observations have to cover the near, mid and far infrared regimes from a few microns up to the (sub)millimeter wavelengths, which are restricted in their spatial resolution due to their relatively large wavelengths. Recent developments in IR interferometry achieved remarkably high spatial resolutions, which revealed details of the inner structure of protoplanetary discs on the scale of less than 1 AU for the solar neighbourhood (e.g., a few $100\,\mathrm{pc}$). These observations confirmed "standard models" to explain the infrared excess in SEDs (Figure 1.2) observed earlier but also posed new questions concerning details of the protostellar evolution of a star and its disc and envelope (e.g., the review of Dullemond and Monnier (2010)).
Another difficulty in understanding the star formation process theoretically lies in the variety of physics involved. Hydrodynamics, gravity, magnetic fields, thermodynamics, turbulence, chemistry and radiative transfer interact with each other on a large range of different scales in length, density and time. E.g., a computer simulation of the formation of a single star like our sun needs to resolve roughly 6 orders of magnitude in length scale (from a few $0.1\,\mathrm{pc}$ ($\sim 10^{16}\,\mathrm{cm}$) of the initial cloud down to stellar radii (e.g., $\mathrm{R}_\odot \sim 10^{10}$ cm), about 20 orders of magnitude in density (from a few 10^5 particles per cm^3 to 10^{24} per cm^3 and roughly 11 orders of magnitude in time (from a few million years to seconds). It is therefore an extremely challenging task, and until today still impossible, to model the star formation process self-consistently in its entirety with a 3D computer simulation.

In the following, we give a brief introduction into the basic theory behind the star formation process, the evolution of a protostar and the mechanisms behind the formation of a protostellar disc, always with an emphasize on the effects of radiation and radiative transfer. This review is mainly based on the textbook by Bodenheimer (2011).

1.3.1 From Molecular Clouds to Stars

Nowadays star formation takes place in giant molecular clouds (GMCs), which form the densest part (a few 10^5 particles per cm^3) of the diffuse ISM in a galaxy like our Milky Way. GMCs contain a significant fraction of the total ISM mass with typically more than $10^4\,\mathrm{M}_\odot$ per cloud on a scale of a few $100\,\mathrm{pc}$. They reveal a highly hierarchical and turbulent structure, in which the

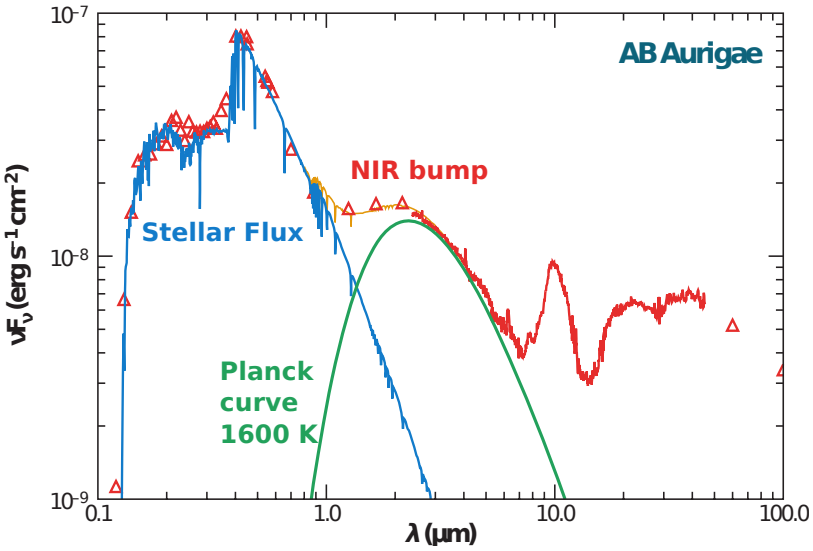

Figure 1.2: The spectral energy distribution of the Herbig Ae star AB Aurigae. Red symbols and lines show the measured emission and the blue curve is a synthetic stellar Kurucz spectrum. The infrared flux ("IR-excess") is the thermal emission from dust in a circumstellar disc. The near infrared (NIR) bump originates from the inner hot rim of the disc, which is approximated by the green Planck curve of $T = 1600\,\mathrm{K}$, similar to the evaporation temperature of cosmic dust. From Dullemond and Monnier (2010).

densest parts are referred to as *clumps*. These clumps are gravitationally bound overdense regions containing a few $100\,\mathrm{M}_\odot$ on the scale of a few pc, from which stellar clusters might form. Single stars or binary systems originate from the fragmentation of such a clump into gravitationally unstable cloud cores with a typical sizes of a few tenth of a parsec and containing up to a few solar masses.

The driving mechanism behind the collapse of such a molecular cloud core is its self-gravity. To generally quantify gravitational instability in an isothermal and uniform medium of density ρ_0, one has to consider gravitational and pressure forces acting against each other. This leads to the Jeans length

$$\lambda_\mathrm{j} = \sqrt{\frac{\pi c_s^2}{G\rho_0}}, \tag{1.7}$$

which describes the maximum extent on which the density distribution is gravitationally stable. The isothermal sound speed c_s in the gas is determined by the temperature of the cloud core (e.g., $\sim 10\,\mathrm{K}$). The Jeans length is directly associated with the Jeans Mass

$$M_\mathrm{j} = \frac{4}{3}\pi\rho_0\left(\frac{\lambda_\mathrm{j}}{2}\right)^3 \tag{1.8}$$

if we assume a spherical density distribution. E.g., the Jeans length for a 10 K ISM gas of a few 10^5 hydrogen atoms per cm^3 is about $0.1\ \mathrm{pc}$, which would be the typical scale of a core to condense out of a molecular cloud due to its self-gravity. The timescale of the collapse is determined by the sound speed crossing time, which dictates the hydrodynamical response of the gas on the global scale of a core. If the gas is considered to be in a free-fall collapse by neglecting the thermal pressure, the associated timescale is the free-fall timescale

$$t_{\mathrm{ff}} = \sqrt{\frac{3\pi}{32 G \rho_0}} \tag{1.9}$$

in which G is the gravitational constant. The free-fall timescale is the typical time on which the initial cloud collapse happens until the formation of a hydrostatic core, in which the thermal pressure is able to stop the gravitational contraction.
The free-fall time for a cloud core is typically on the order of a few 10^5 years. However, GMC's lifetimes from observations (e.g., by measuring velocity dispersions) reveal to be roughly one order of magnitude higher than the free-fall time. This already indicates that more complex physics are involved, e.g., turbulence and magnetic pressure, but the free-fall assumption nevertheless gives a rough approximation of the timescale of the first collapse of a molecular cloud core.

Formation of the first Hydrostatic Core

Once a cloud core becomes gravitationally unstable and starts to collapse, it releases a large amount of gravitational energy. Initially, this energy is radiated away freely as long as the cloud core stays optically thin. The heating of the gas by contraction is therefore always balanced by the rate of radiative cooling and hence, the cloud's temperature stays constant (isothermal) typically at a few 10 K. As inferred by Equation (1.9), the free-fall timescale decrease with increasing density, which leads to an accelerated "run-away" collapse of the entire core while the inner regions become more and more highly peaked in their density profile.
The isothermal collapse starts to decelerate as soon as the collapsing core becomes opaque and radiation gets "trapped" inside a small region in the center of the core. At densities about $10^{-13}\,\mathrm{g\,cm^{-3}}$ (Larson, 1969), the compressional heating rate starts to dominate the efficiency of radiative cooling and consequently, the temperature and pressure in the central core start to rise rapidly (Figure 1.3). The following contraction becomes approximately adiabatic and after roughly one free-fall time, a central hydrostatic core of a few $10^{-2}\mathrm{M}_\odot$ with a radius of $5 - 10$ AU

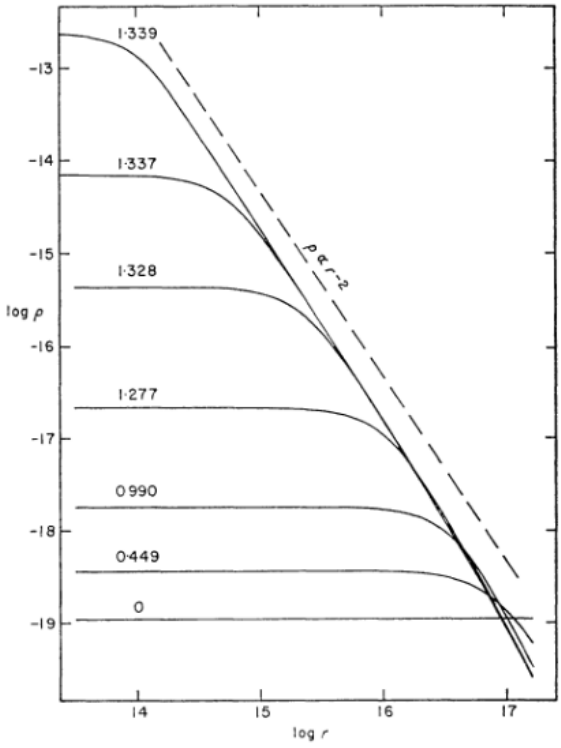

Figure 1.3: The time evolution of the density distribution of a collapsing protostar from the 1D calculations of Larson (1969). Units are in CGS, and the curves are labelled in units of the free-fall time ($\sim 10^{13}$s). Note how the density distribution approaches a profile of the form $\rho \propto r^{-2}$.

and a central temperature of a few 100 K has formed inside the envelope. This hydrostatic core is commonly referred to as the first core or the first protostellar core. The term 'protostar' is somehow not clearly fixed but we will refer to it as being any hydrostatic core that forms after the initial isothermal collapse including a possible accretion disc.

The protostar starts accreting material from its surrounding infalling envelope and accretion disc and the first core continues to contract. According to the virial theorem, half of the released gravitational energy is converted into thermal energy and the other half diffuses outward radiatively. Shortly after the first collapse, the main bulk of the core material is still in the envelope while the first core contains only a few $10^{-2}\,\mathrm{M}_\odot$. Its luminosity is determined by

$$L_{\mathrm{acc}} = \frac{GM_*\dot{M}}{R_*} \tag{1.10}$$

of the first accretion shock front, where the infalling material is abruptly decelerated and accumulated in the first core. L_{acc}, R_* and M_* are the protostar's accretion luminosity, core radius and mass respectively, and $\dot{M}$ denotes the accretion rate.

Formation of the second pre-stellar Core

Before the first core had a chance to accumulate much mass from the envelope, it continues to contract until the central temperature reaches a value of about $2000\,\mathrm{K}$ with a central density of about 10^{-8} g cm^{-3}. At this point, hydrogen molecules start to dissociate. The dissociation reduces the ratio of specific heats since atomic hydrogen lacks the possibility to be excited rotationally and the pressure rises less steeply with increased density. Since most of the released gravitational energy is consumed by the dissociation processes, the core starts to cool again and enters another quasi-isothermal second collapse phase. As soon as nearly all hydrogen molecules are dissociated ($\sim 8000\,\mathrm{K}$), the central pressure rises again rapidly until a second hydrostatic core is formed with a typical central density of 10^{-4} - 10^{-2} g cm^{-3}, a few $\mathrm{R}_\odot$ in radius and a central temperature of a few 10^4K for a solar-like protostar, thus approaching stellar conditions.
The second collapse inside the first hydrostatic core happens again on a free-fall timescale and the second core initially only contains a few $10^{-3}\mathrm{M}_\odot$ while the bulk of the core mass is still located in the isothermal envelope at densities of $10^{-18} - 10^{-19}$ g cm^{-3}. While the second core also develops an accretion shock front, the first core is soon depleted and accreted into the second pre-stellar core. This second core is still embedded in a dense infalling envelope of material which produces an accretion shock at the point where the material falls onto the central hydrostatic core. Observationally this earliest phase in the star formation process is characterized by a source which is extremely faint in the optical and infrared. It emits mainly in the submillimeter regime which originates from the massive envelope's reprocessed radiation of the protostar's accretion luminosity at temperatures about $15 - 30\,\mathrm{K}$ (Class 0 / Class I phase). Since during this phase the envelope becomes more and more opaque to radiation and the radius of the hydrostatic core decreases, the total luminosity of the protostar decreases and it follows an almost vertical path down on the Hertzsprung-Russell diagram (Hayashi track, Figure 1.4).

On the Way to the Main Sequence

The subsequent evolution of the protostar evolves quasi-statically while hydrogen in the hot pre-stellar core is ionized. However, the ionization does not alter the effective ratio of specific heat very much since the densities are already high enough for the gas to act non-ideally. The core therefore stays in hydrostatic equilibrium and no further collapse occurs. The pre-stellar core now enters the main accretion phase in which the remaining mass of the massive envelope continues to collapse on the pre-stellar core (and the accretion disc).

Behind the accretion shock the kinetic energy of the infalling gas is almost entirely converted into radiative energy which diffuses outward and is absorbed by the opaque envelope. The luminosity of the protostar is therefore determined by the accretion luminosity and the intrinsic luminosity of the contracting core

$$L_* = L_{\rm acc} + L_{\rm int}. \tag{1.11}$$

During the early accretion phase, the envelope is still collapsing onto the protostar and the accretion luminosity dominates during another few free-fall times. Until roughly 1 million years after the initial core collapse, the envelope is depleted and was either accumulated by the pre-stellar core or has fallen onto the accretion disc.

The protostar has now probably developed a rotationally supported Keplerian disc and is commonly referred to as a pre-main-sequence (PMS) star. At this point, the star has gained about half of its final mass while still accreting mass from the accretion disc. However, the total luminosity of the PMS star is now mainly determined by its intrinsic luminosity due to the quasi-statical contraction which reads

$$L_{\rm int} \approx -\frac{1}{2}\frac{d\Omega_G}{dt}, \tag{1.12}$$

where Ω_G denotes the gravitational potential of the central hydrostatic core. Since the circumstellar envelope was depleted, the subsequent evolution of the PMS star is not determined by the free-fall timescale anymore but by the Kelvin-Helmholtz (KH) contraction timescale:

$$t_{\rm KH} \approx \frac{GM_*^2}{R_* L_{\rm int}}. \tag{1.13}$$

The KH-timescale is an order of magnitude larger than the free-fall timescale (~10^6 years), and because the PMS star contracts further, R_* decreases, and the evolution slows down, which makes is much easier to observe a PMS star approaching the main sequence than an early protostar on the Hayashi track. Since the PMS star still accretes mass but is contracting, its luminosity only increases slightly. Hence, the evolution on the KH-timescale in the HR-diagram is characterized by an almost horizontal path until the PMS star reaches its final effective surface temperature (Henyey track, Figure 1.4). After a few KH-timescales (e.g., 10^7 years), the PMS star approaches the main sequence, and its central temperature is finally high enough (e.g., a few 10^6 K) to ignite hydrogen burning. At this time, the protostellar disc has probably been depleted significantly, and from the debris that is left, a planetary system might form (Figure 1.5).

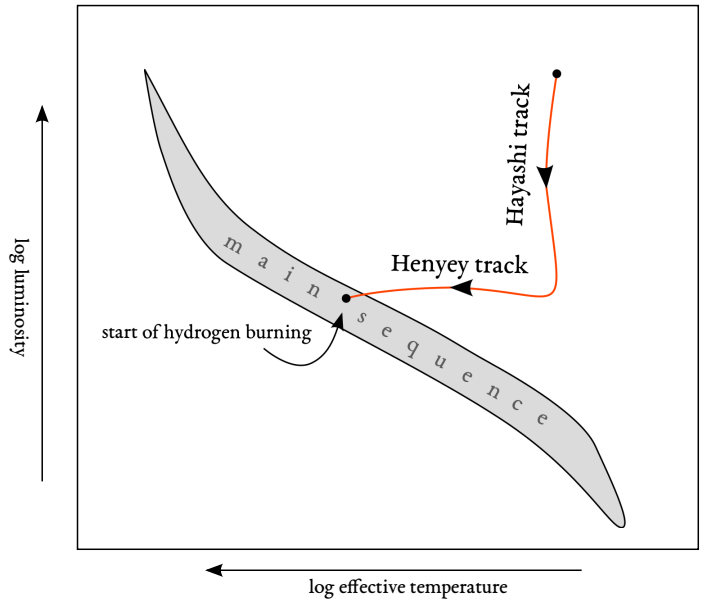

Figure 1.4: Schematics of the Hayashi and Henyey tracks in the Hertzsprung-Russell diagram for a star of one solar mass. The protostar in quasi-hydrostatic equilibrium first appears above the main sequence on the Hayashi track, when the dissociation of H2 molecules starts. Its luminosity decreases since radiation gets trapped due to the increasing density of the gaseous envelope. After the formation of the second pre-stellar core, the protostar maintains a more or less constant luminosity during the Kelvin-Helmholtz contraction phase (Henyey track) until it reaches the main sequence.

Massive Star Formation

We have concealed that our review of the star formation process so far is actually the common picture of low mass and intermediate mass star formation we have today. The formation of massive stars ($\gtrsim 8\,\mathrm{M}_\odot$) is in some ways similar to low-mass star formation but for several reasons, the details of the early evolutionary phases are much less well understood. The formation of massive stars in general happens much faster than that of their low-mass counterparts, and it is therefore less likely to observe massive stars in their early evolutionary phases. Since massive OB-Stars naturally form in the most dense clumps of a GMC, containing up to a few thousand solar masses on the scale of a few tenth of a parsec, they are deeply embedded in massive, circumstellar and dusty envelopes, which makes them much harder to observe. Zinnecker and Yorke (2007) identify four phases of massive star formation: compression, collapse, accretion and disruption. In the compression phase, turbulence and gravitation form dense clumps in the parent GMC by localized compression of the gas. These clumps are either disrupted again or might undergo a gravitational collapse (collapse phase) and form several hydrostatic cloud cores. During the accretion phase, a massive star already starts hydrogen burning in its interior while still accreting significant amount

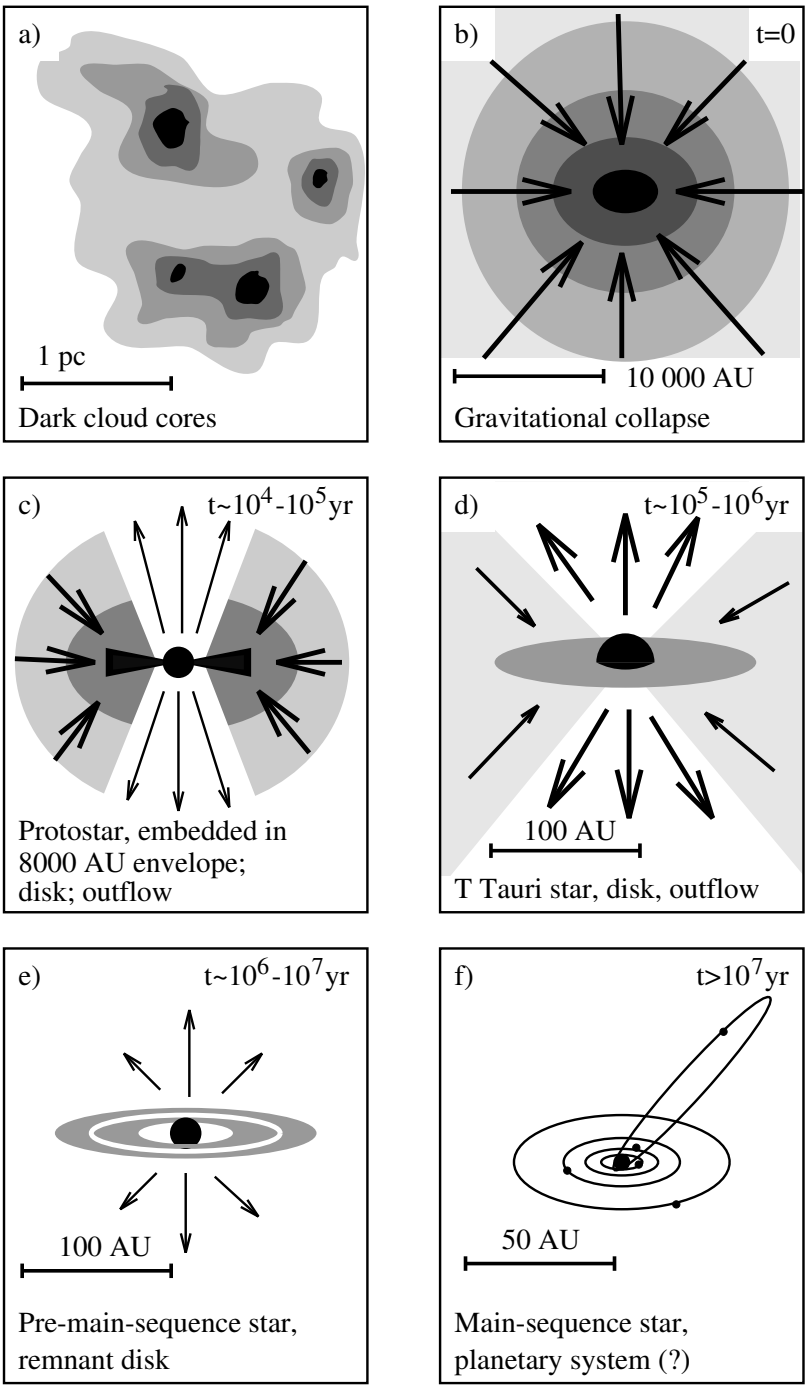

Figure 1.5: Schematics of the different phases of the low/intermediate mass star formation process; From Hogerheijde, M. (1998), PhD Thesis, Leiden University, Holland.

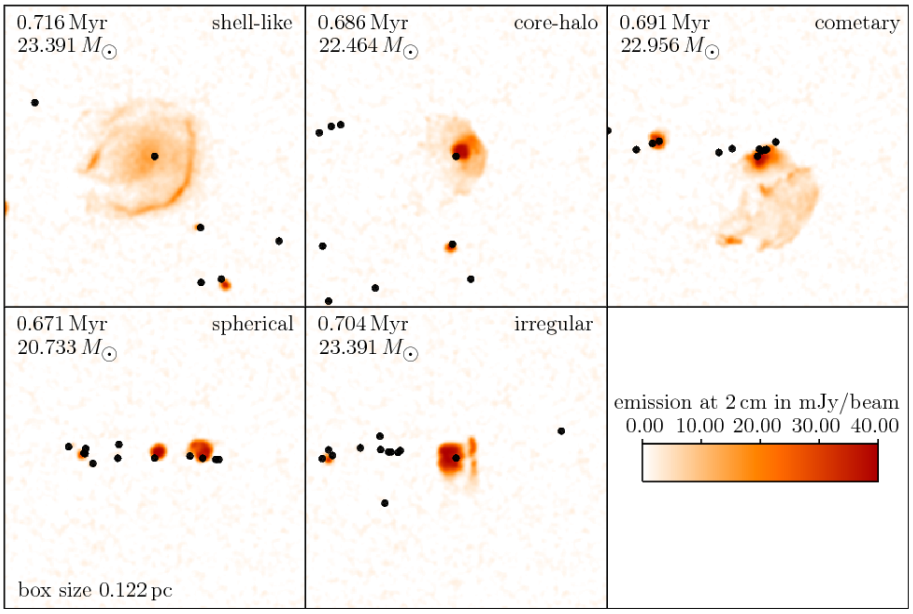

Figure 1.6: Various HII region morphologies from hydrodynamical simulations of massive star cluster formation including heating by both ionizing and non-ionizing radiation. The simulations were performed with the FLASH code and the hybrid characteristics method by Rijkhorst et al. (2006), image from Peters et al. (2010).

of masses from its surrounding envelope. Massive stars strongly influence their surroundings by stellar winds, outflows and energetic UV-radiation. Hence, they significantly determine ongoing star formation in an OB-cluster. After a short lifetime of a few million years, OB-stars go off as energetic supernovae and may even disrupt the cloud, from which they formed, preventing further star formation. It is still not clear how massive stars can accrete large masses of up to more than $100\,\mathrm{M}_\odot$. Radiative pressure should be able to stop accretion processes while, due to energetic UV-photons, large regions of ionized hydrogen (HII-regions, Figure 1.6) emerge around massive stars.

1.3.2 Circumstellar Discs

During our discussion of the star formation process, we neglected the effects of rotation. Since rotation is inherit in the Milky Way, molecular cloud cores reveal some amount of rotational energy. Although the rotational energy makes up only a small fraction of the total energy content of the gas (e.g., a few percent), the conservation of angular momentum becomes crucial as soon as a clump fragments and forms stars. The importance of discs is obvious since they are assumed to be the birthplace of planetary systems, which are believed to form from a thin

Keplerian disc which remains after the host star has accreted its final mass.

In the following, we describe the basics of disc formation, evolution and dissolution based on the book by Bodenheimer (2011) and the reviews by Li et al. (2014) and Dullemond and Monnier (2010).

Disc Formation

If we consider a gas package of mass m orbiting with an angular velocity Ω in the envelope around a recently formed protostar at distance r from the pre-stellar core, the angular momentum

$$l = m\, r^2 \Omega \tag{1.14}$$

is conserved during the infall of the gas package onto the protostar. Since r decreases during the infall, the angular velocity Ω has to increase. The gas package is accelerated in its orbital motion until it reaches the centrifugal barrier at which the gravitational acceleration is compensated by the centrifugal force. Consequently, instead of falling directly on the central hydrostatic core, momentum conservation forces a significant amount of infalling gas from the envelope to accumulate into a circumstellar disc instead of being accreted directly into the pre-stellar core.
Initially, the mass of the newly formed circumstellar disc is comparable to the mass of the central core and hence, the early disc itself might be prone to gravitational instabilities. Whether the centrifugal force caused by the angular motion can counteract a gravitational instability is indicated by the Toomre parameter (Toomre, 1964)

$$Q = \frac{\kappa c_s}{\pi G \Sigma}, \tag{1.15}$$

where Σ denotes the surface density of the disc (e.g., $\Sigma = \frac{M_{\rm disc}}{\pi R^2}$), and κ is the epicyclic frequency, which describes the dependence of angular momentum on radius (e.g., $\kappa = \Omega$ in a Keplerian disc). If Q is larger than ≈ 1, the gas in the disc is locally stable against gravitational instabilities since the angular differential motion will disrupt it. Examining the Toomre parameter reveals that even low mass discs with $M_{\rm disc}/M_* \approx 0.1$ should be gravitationally unstable and fragment although observations indicate that discs of comparable mass typically exist around PMS stars and that they have probably been even more massive initially. However, since the accretion of the disc mass starts with a rather low surface density Σ, the Toomre parameter Q is initially larger than

1, and before Q actually is near 1, gravitational instabilities can generate spiral waves. The waves cause gravitational torques to transport angular momentum outward from the inner regions of the disc and heat up the disc, which can stabilize the disc against fragmentation. After a few 10^5 years, the disc becomes stable, and angular momentum transport by gravitational torques becomes ineffective.
Observationally, the early formation of a massive disc is difficult to observe since it happens inside the massive gaseous envelope. Discs are more likely to be observed after they have already evolved into Keplerian protoplanetary (see next section) discs which have already lost a significant amount of mass to the PMS star in its center and become observable (Class II stage). The key properties described so far are therefore mostly based on numerical simulations (e.g. Yorke et al., 1993).

Disc Evolution

The early formation process of the disc is characterized by gravitational forces and instabilities while the disc is still massive. Such a disc is referred to as a protostellar disc (Figure 1.7). The evolutionary timescale is roughly given by $t_{\rm grav} \approx \Omega^{-1}(M_*/M_{\rm disc})^2$ and hence, it is evolving quite rapidly in the beginning when its mass is still comparable to that of the central stellar core. After a few 10^5 years, when the disc has lost most of its mass to the central star, its subsequent evolution is determined by angular momentum transport through viscous and magnetic torques which occur on a much slower timescale. Since these discs have lifetimes of a few 10^6 up to 10^7 years, there is enough time for them to create planets, which is why they are referred to as protoplanetary discs. Such a disc is assumed to be geometrically thin, in Keplerian rotation $\Omega_K = (GM_*/r^3)^{1/2}$ and its self-gravity is negligible compared to the central star ($M_{\rm disc} \ll M_*$). There are a number of analytical models to describe the evolution of a protoplanetary disc. Shakura and Sunyaev (1973) assume the vertical sound crossing time in the disc to be much shorter than the radial drift of gas and hence split the problem. The vertical structure is assumed to be isothermal and in hydrostatic equilibrium at all times, and the evolution of the surface density and the radial drift of gas is determined by a viscosity coefficient. The idea is that the differential rotation in the disc causes frictional torques which transport angular momentum from the inner fast rotating to the outer slower rotating regions of the disc. This allows a gas package to loose angular momentum and drift inwards, where it is accreted. The viscosity coefficient also causes the disc to actively heat itself, and Shakura and Sunyaev (1973) define a viscous heat source term which depends on the accretion rate and the angular velocity in the disc. Approximating the disc with a black body

emitter allows to model the temperature structure in the disc. Shakura and Sunyaev (1973) do not explicitly define the source of viscosity but rather assume a constant parameter, the alpha viscosity, which may account for all present viscosity sources. The alpha viscosity is a free parameter in their model which can be used to fit the model to the infrared excess slope of an SED and determine the accretion rate.

Shakura and Sunyaev (1973) assume the accretion disc to be flat and infinitely large. However, a disc has a finite size and as matter moves inward, some matter in the outer regions has to absorb the angular momentum. This leads to a spreading of the disc (Lynden-Bell and Pringle, 1974; Hartmann et al., 1998), and as it turns out, viscous torques alone (e.g., molecular viscosity) are too slow to guarantee sufficient angular momentum transport.

Recent numerical simulations have shown that turbulence and magnetic fields have a profound effect on the disc's evolution. Turbulence acts as another source of viscosity, and especially magnetic fields have proven to be a rather effective mechanism to transport angular momentum outwards. In those simulations assuming ideal MHD (e.g. Mellon and Li, 2008; Hennebelle and Fromang, 2008; Seifried et al., 2012; Santos-Lima et al., 2012), the magnetic field is frozen into the gas density and hence, the densest inner regions of the protostar become strongly magnetized. Since the magnetic field lines rotate with the gas, they get twisted by the differential rotation. This causes a tension in the field lines which tends to slow down the inner fast rotating regions of the disc. In fact, this mechanism is so efficient in the ideal MHD limit that simulations showed no build-up of Keplerian discs at all, although they assume initial magnetic field strengths similar to those obtained by observations. This so called magnetic braking catastrophe indicates that non-ideal MHD effects have to be taken into account (e.g., ambipolar diffusion, Ohmic dissipation (Dapp et al., 2011) and the Hall effect) to understand the formation of Keplerian protoplanetary discs. The magnetic braking catastrophe also emphasizes the importance of turbulence since magnetically driven angular momentum transport might be substantially weakened by the tangling of field lines in a turbulent medium (Seifried et al., 2012).

The assumption of a flat disc by Shakura and Sunyaev (1973) ignores any external irradiation since they originally aimed at modelling accretion discs around black holes. The resulting effective temperature distribution reveals to be $T_{\text{eff}} \propto r^{-3/4}$ which results in an infrared excess slope of $\nu F_\nu \propto \nu^{4/3}$. Fitting the slope with the flat disc model tends to overestimate the accretion rates of observed SEDs of T Tauri and Herbig Ae/Be stars. Chiang and Goldreich (1997) present an analytical model of a flared disc, in which the vertical structure of the disc is determined by the irradiation of the central star. They assume that the radiation is absorbed by dust grains in an

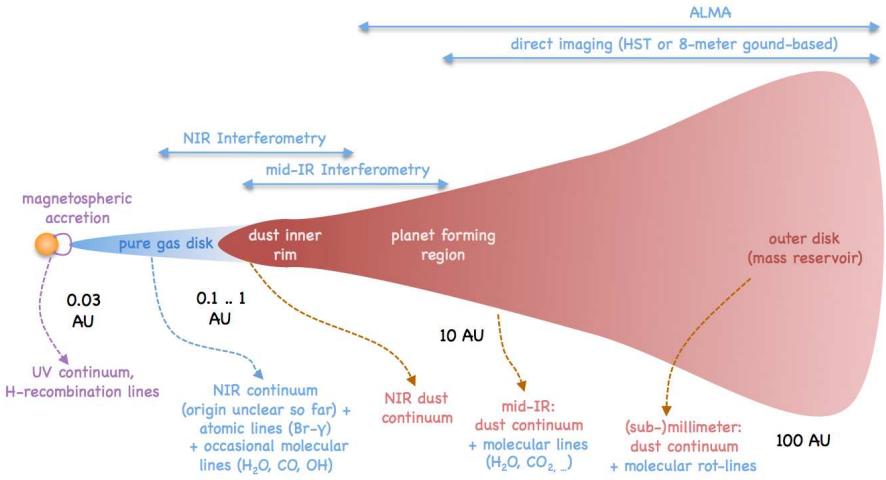

Figure 1.7: Pictogram of the structure and spatial scales of a flared protoplanetary disk. Above the pictogram is shown which instruments are capable of resolving which part of the disc. Below the pictogram is noted from which part of the disc which kind of emission originates. From Dullemond and Monnier (2010).

outer hot surface layer (photosphere), and half of the reemitted thermal radiation then heats the interior layer. Since the disc has a flared structure, the amount of absorbed energy depends on the angle under which radiation enters the photosphere. A simple 1D vertical radiative transfer model accounts for the heating of the internal layer. Chiang and Goldreich (1997) assume the internal layer to be isothermal and derive a Gaussian vertical density distribution. In the flared disc model, the ratio of scale height to radius increases with radius, which causes the outer layers to intercept more radiation than in the flat disc model. This causes the temperature structure to vary less rapidly than $T_{\rm eff} \propto r^{-3/4}$ and fit the typical observed infrared slopes in SEDs of TTauri stars much better than under the assumption of a flat disc. This indicates that the outer regions of a Keplerian protoplanetary disc is rather dominated by external radiation than by viscous heating and emphasizes the importance of radiative transfer not only in analytical models but especially for numerical simulations.

1.3.3 Radiative Feedback in the Star Formation Process

Radiative feedback mainly affects the ISM by heating and cooling processes. Dust is commonly present in the ISM at temperatures below $\approx$ 1500 K and strongly affects radiative transfer by its continuum opacities. At higher temperatures, the dust is evaporated and line opacities of the

gas dominate (Semenov et al., 2003). The importance of radiative heating and cooling is analytically motivated by the Jeans length in Equation (1.7) which can be rewritten in terms of the gas temperature:

$$\lambda_{\mathrm{j}} = \sqrt{\frac{\pi c_s^2}{G\rho}} \propto \left(\frac{T}{\rho}\right)^{1/2}. \tag{1.16}$$

However, radiative feedback of low and intermediate mass stars does not have such a strong influence on the overall cloud structure as, e.g., the magnetic field (Price and Bate, 2010). The magnetic pressure can have a dramatic influence on the structure of low mass star forming regions since it can can create magnetically supported voids in the GMC. But in regions where massive star formation occurs this picture dramatically changes. The most prominent example is probably the Orion nebula in which a small number of young, luminous, massive OB stars (e.g., the five Theta Orionis trapezium stars, Figure 1.8) is able to ionize the entire cloud. Massive stars emit a large number of UV photons which are able to heat up their surroundings to a few 10^4K by ionizing hydrogen atoms. The following build-up of large HII regions can dramatically change the cloud structure (Figure 1.6).

Radiative feedback also becomes important during the early formation of massive stars. Since massive stars already start hydrogen burning while still accreting mass, they exert a significant radiative pressure on the infalling material. At some point, the radiative pressure should prevent the star from accreting more mass and thus starving it out. It is still not clear how massive stars then can accrete large masses of up to more than $100\,\mathrm{M}_\odot$. Recent simulations of clusters of massive stars emphasize the need for 3D effects such as accretion through a protostellar disc (e.g. Peters et al., 2010; Kuiper et al., 2012).

However, on smaller scales, low mass and intermediate mass protostars also significantly influence their surroundings by radiative feedback. By increasing the fragmentation scale, radiative heating (from the accretion luminosity) can completely inhibit further fragmentation in a radius of several AU and prevent, e.g., the formation of a binary system (Price and Bate, 2010). Consequently, the cloud tends to produce less but more massive stars which results in a reduction of the star formation efficiency in the low mass regime of the initial mass function (IMF). Regarding the formation and evolution of protostellar and protoplanetary discs (Section 1.3.2), we already discussed the influence of radiation on the structure of the disc (Chiang and Goldreich, 1997). Furthermore, during the early formation of the protostellar disc, radiative heating becomes

crucial as one can see from the temperature dependence of the Toomre parameter:

$$Q = \frac{\kappa c_s}{\pi G \Sigma} \propto T^{1/2}. \tag{1.17}$$

Thus radiative heating should significantly influence the fragmentation behaviour of a self-gravitating protostellar disc. Offner et al. (2009) investigated the IMF and the star formation rate (SFR) by comparing 3D MHD simulations of low mass star formation with and without the effects of radiative transfer. They found that the thermal support of a protostar's accretion luminosity suppresses further fragmentation in the cloud core as well as in the protostellar disc. The SFR in their simulations is about half the value of the simulations without radiative transfer and the mass distribution of protostars of very low mass ($M_* < 0.1\mathrm{M}_\odot$) is significantly reduced. Bate (2009) finds similar effects.

The formation and evolution of a protostar up to a main sequence star with a planetary system is inexplicably connected by the interplay of a number of effects in different stages (see Section 1.3.2). It is evident from observations that after a few 10^5 years after the initial core collapse, gaseous rotationally supported Keplerian discs are present around low and intermediate mass stars (Evans et al., 2009). Keplerian discs have been subject to a large number of analytical and numerical studies and also the initial formation of massive discs during the Class 0 phase has been investigated using hydrodynamical and MHD simulations (e.g. Yorke et al., 1993; Mellon and Li, 2008; Machida et al., 2010; Seifried et al., 2011). Seifried et al. (2013) emphasize the importance of turbulence to explain the formation of Keplerian discs even if strong magnetic fields are present. Despite a large number of studies, the actual transition from the early self-gravitating protostellar disc (Class 0) to the Keplerian protostellar disc is still poorly understood. Recent observations (e.g. Tobin et al., 2012) indicate that Keplerian discs might form very early during the protostellar evolution and the analytic study by Forgan and Rice (2013) emphasizes the effects of radiative processes.

However, the effects of radiative transfer have usually been neglected so far or were substantially approximated. The self-consistent modelling of the formation and early evolution of protostellar discs therefore creates the need for new numerical methods to make 3D radiation MHD simulations feasible.

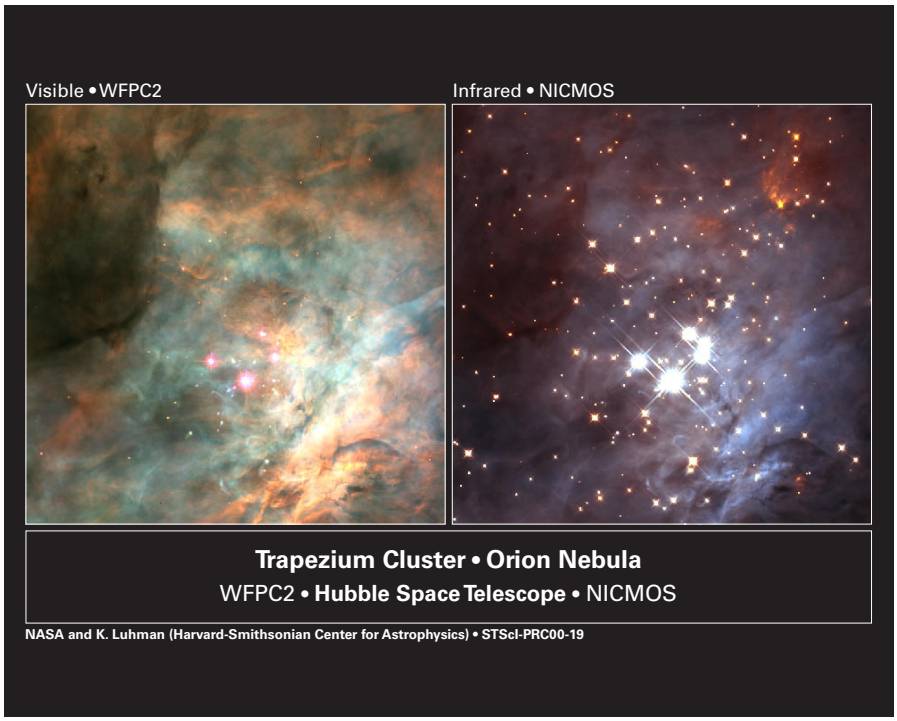

Figure 1.8: The Theta Orionis Trapezium constellation in the Orion Nebula as observed by the Hubble space telescope; *left:* optical image (WFPC2), *right:* infrared (NICMOS). The five Trapezium stars resemble a relatively young cluster of massive stars (15-30 $\mathrm{M}_{\odot}$) which illuminate and ionize their surroundings. Note that in the infrared many more stars are seen while in the optical image dust absorption blocks their light.

1.4 Numerical Radiation Magnetohydrodynamics

Depending on the level of approximation that is involved, numerical radiative transfer is a rather costly computation compared to other numerical tasks like hydrodynamics. Although the radiation field is rather straightforward to compute if all injection rates and absorption coefficients are known, the scattering problem or the successive thermal absorption and reemission are challenging task to deal with. Non-local problems in computational physics usually lead to large systems of differential equations which are tightly coupled. Although these systems are linear (in terms of radiative quantities) and could in principle be solved by inverting a coefficient matrix, this is not practical in terms of computational costs and memory requirement since the coefficient matrix is far from being sparse (e.g., lots of non-zero and non-diagonal entries). Since in a computer code for radiative transfer the explicit construction of a coefficient matrix would require to compute the radiative exchange rates of each discretization point with each other, this would very easily exceed reasonable memory requirements in 2D and 3D simulations. Furthermore, the inversion of a highly non-sparse matrix itself would be rather costly and inefficient as well. Naive approaches of iterating for self-consistent solutions turn out to be very inefficient because they are costly, slow converging and may even give unreliable results. Nevertheless, in the last decades, several powerful techniques have been developed to deal with these problems more or less accurately and efficiently. These techniques include fundamentally different approaches like the discrete ordinate method of long and short characteristics as well as statistical approaches, like the Monte Carlo (MC) method, and approximate solutions, like the flux-limited diffusion (FLD) approximation, which is commonly used for radiation MHD calculations. Radiative transfer also comes in a variety of parallelizations for high performance computations, including AMR with domain decomposition for the FLD approximation, angular parallelization for discrete ordinate methods or photon package parallelization in MC codes.

However, all the difficulties of numerical radiative transfer become even more complex when coupled to the mechanical dynamics of the medium the radiation originates from. This is the topic of radiation hydrodynamics and, including magnetic fields, radiation MHD. Handling radiative transfer in parallel with MHD poses several problems. First, the timescales of both problems are very different. The timescale of radiative transfer is determined by the speed of light and is much shorter than the timescale of MHD, which mainly depends on the sound speed of the gas and the characteristic magnetic Alfvén wave speeds. Castor (2007, Section 11.1) discusses the Courant limit for the combined equations of radiative transfer and hydrodynamics in the diffusion limit,

which requires that

$$\frac{K_R \Delta t}{\rho C_v (\Delta x)^2} = \frac{16 \sigma_{\rm SB} T^4}{3 \rho C_v T V} \frac{1}{\kappa_R \rho \Delta x} \frac{V \Delta t}{\Delta x} < 1, \tag{1.18}$$

where κ_R is the Rosseland mean opacity, V is the typical flow speed and C_v is the heat capacity of the radiating fluid with temperature T and density ρ. The first factor on the right-hand side is basically the inverse of the Boltzmann number, which gives an estimate of the relative importance of thermal and radiative energy. The second factor is the inverse of the optical depth of a single computational cell of linear size Δx, and the third factor is the usual Courant number of hydrodynamics. The inverse Boltzmann number is the factor that can cause the combined Courant limit to easily exceed a factor of about 100 which makes the explicit handling of radiative transfer unfeasible unless some "reduced speed of light" approximation is used (e.g., the RAMSES code (Rosdahl et al., 2013)). This leads to the idea of operator splitting in which the problem of radiation MHD is split into a successive solution of the MHD equations and the equation of radiative transfer one after the other. Since radiation MHD computations should be handled on the MHD timescale, the radiative transfer step then has to be solved implicitly. Since the radiation field is coupled to the thermodynamics of the gas mainly by heating, cooling and momentum source terms, this leads to a large system of differential equations for the unknown temperature of the gas.

In the following we give a brief overview of current "state-of-the-art" methods which are used for radiation MHD computations.

The Flux-Limited Diffusion Approximation

The flux-limited diffusion approximation has been extensively used to model the evolution of the radiation field for MHD simulations since it was introduced by (Levermore and Pomraning, 1981). The diffusion approximation treats the radiation field like a diffusive fluid that is evolved in parallel with the thermal gas and can exchange energy and momentum. In general, this approximation requires the medium to be optically thick, so that all terms $\propto 1/\chi$ can be neglected (χ is the opacity) in the moment equations of the RTE. This leads to *Eddington's approximation* and a system of hyperbolic equations for the radiation field. However, the large propagation speed of light still forbids to solve this system of advection equations explicitly like it is done in MHD. Instead the time dependence of the radiative flux is neglected which makes it only proportional to the gradient of the radiative energy (Fick's law). This leads to a single diffusion-like equation

for the radiative energy:

$$\frac{\partial E_\nu}{\partial t} - \nabla \cdot \left(\frac{c}{3\chi_\nu} \nabla E_\nu \right) = 4\pi\eta_\nu - \chi_\nu c E_\nu. \tag{1.19}$$

where E_ν and η_ν are the radiative energy and emissivity respectively. The diffusion approximation in this form requires Eddington's approximation to eliminate the radiative pressure from the equation by assuming it to be isotropic:

$$P_\nu = \frac{1}{3} E_\nu. \tag{1.20}$$

Usually the radiative pressure is a 3×3 tensor matrix which includes the anisotropic information of the radiation field. Consequently, the diffusion approximation in the form of Equation (1.19) has lost all angular information of the radiation field making it comparable to the diffusion of a usual fluid. The loss of angular information is due to the assumption of an optically thick regime in which radiation in fact diffuses isotropically. Despite this restriction, the diffusion approximation is also often used in optically thin regimes where an ad hoc assumption about the propagation speed has to prevent the radiative flux from emerging at unphysical speeds. This leads to the concept of flux-limiters (Levermore and Pomraning, 1981) which depend on the gradient of the radiative energy. Eddington's approximation then becomes the limit of the flux-limiter λ in the case of high optical depths ($\lambda = \frac{1}{3}$). The FLD approximation has been implemented in a number of Eulerian grid based MHD codes (e.g. Stone et al., 1992; Flock et al., 2013; Zhang et al., 2013; Bryan et al., 2014) and also within SPH-Codes (Bate et al., 2013). Though the FLD approximation is very efficient in modelling the diffusion limit, it is invalid especially in transition regions from optically thick to thin regimes. The main reason for this is the loss of the anisotropy of the radiation field which allows the radiative energy to slowly diffuse into shadow regions. For instance, Kuiper et al. (2010) have shown an example of an irradiated circumstellar disc with highly anisotropic optical depths based on the benchmark by Pascucci et al. (2004). The thermal structure inside the disc should mainly be determined by the reprocessed radiation from the photosphere of the disc since only the outer layers are exposed to the primary stellar irradiation. Kuiper et al. (2010) use a hybrid method where the stellar irradiation is followed by a raytracing approach while the diffuse reprocessed radiation is added using FLD. Their results are in excellent agreement with the Pascucci et al. (2004) benchmark, while using exclusively FLD is not able to model the transition region in the disc's photosphere accurately.

Characteristics based Radiative Transfer

Characteristics based radiative transfer is a discrete ordinate method based on the geometrical optics limit. Light propagation is described in terms of rays along which the radiative intensity is integrated. The limit of geometrical optics is valid in regimes where spatial scales are much larger than the wavelength of radiation, which is clearly the case in most astrophysical applications. Along with the spatial discretization, the RTE is also discretized in the angular dimension, hence preserving the anisotropy of the radiation field. Olson et al. (1986) introduced the method of characteristics to solve the scattering problem in a 1D plane-parallel NLTE atmosphere. For multi-dimensional radiative transfer computations the method of characteristics is based on reducing the partial differential form of the RTE to a series of ordinary differential equations along a parameterized characteristic which covers a certain opening angle. For astrophysical computations the time dependence of the radiation field is often neglected avoiding the need for storing the full angle-dependent field of intensities.
For radiation MHD computations, the method of characteristics is not as popular as the FLD approximation since it is much more computationally expensive for 3D simulations. Nevertheless, if dominant point sources of radiation (e.g., a stellar source) are present in the computational domain, characteristics based methods have become popular to account for at least the most energetic primary emission (e.g. Rijkhorst et al., 2006; Peters et al., 2010; Flock et al., 2013). Since the solution of the RTE along a characteristic usually requires raytracing through the computational domain, it is rather difficult to work in accordance with the parallel design of modern MHD codes which combine AMR techniques with spatial domain decomposition. Nevertheless, AMR MHD codes have been successfully combined with characteristics based radiative transfer codes mainly in the field of stellar atmosphere physics (e.g. van Noort et al., 2002; Heinemann et al., 2006; Hayek et al., 2010; Davis et al., 2012), though some of these approaches reduce the unavoidable communication overhead by using short characteristics.

The Monte Carlo method

The Monte Carlo (MC) method is a statistical approach for handling radiative transfer. Despite the spatial one, the MC method avoids any further discretization by taking advantage of the statistical nature of photon propagation. The paths of single photons or photon packages are explicitly followed until they are either absorbed, scattered or leave the computational domain. The probabilities for absorption and scattering events are calculated from optical depths and the frequency

(re)distribution is naturally determined by Planck's law. Several optimizations have been introduced, e.g., photon package peel-off (Lucy, 1999), immediate reemission (Bjorkman and Wood, 2001) and some advancements have been made in dealing with highly optically thick regimes (Min et al., 2009). The MC method is rather successful in post-processing the outcome from MHD simulations to generate synthetic SEDs, polarization maps or images but has rarely been used for time-dependent radiation MHD simulations. The reason for this is that MC codes are usually parallelized by photon packages since each package can be followed independently from each other. Because the path a photon package will take is determined statistically, MC codes are difficult to work with AMR MHD codes that employ domain decomposition. However, Acreman et al. (2010) used the MC method in an SPH Code for modelling circumstellar discs with 3D radiation hydrodynamics, and Harries (2011) presented a time-dependent algorithm for MC radiative transfer, although both works were rather restricted in their spatial resolutions due to the parallelization scheme involved.

1.5 Objectives

In this work, we present a new implementation of a radiative transfer solver based on the method of hybrid characteristics. The solver is implemented in the framework of the MHD code FLASH, which is a versatile well tested and widely used hydrodynamical and MHD computer code written in Fortran. The theory behind radiative transfer and the solution of the radiative transfer problem is presented in Chapter 2. In Chapter 3, we discuss in detail the method of hybrid characteristics, the radiative transfer solver and how it is implemented in the AMR framework. Test results from the radiation solver and its coupling to the FLASH code are presented in Chapter 4, and results from full 3D radiation hydrodynamical simulations are shown in Chapter 5. Finally, in Chapter 6 we summarize our work and discuss some possible improvements to optimize our implementation.

2

Radiation Hydrodynamics

In this chapter, we describe the theoretical background concerning radiative transfer (Section 2.1) and hydrodynamics (Section 2.2). We also present the theory that lies behind our approach of solving the radiative transfer equation (RTE). The combined equations of hydrodynamics with radiation are discussed briefly in Section 2.3. A more detailed description of the actual coupling of our radiative transfer solver with the FLASH code can be found in the following Chapter 3 which deals with the details of the implementation that is based on the theory in this chapter.

2.1 Radiative Transfer

The theory of radiative transfer, we describe in this section, is based on the well known work by Mihalas and Weibel Mihalas (1984) and the textbook by Castor (2007). And last but not least, we also got very helpful insight from the excellent lecture scripts by Prof. Dr. Cornelis P. Dullemond[1].

[1] http://www.ita.uni-heidelberg.de/ dullemond/lectures/radtrans_2012/index.shtml

2.1.1 Radiative Quantities

In this section, we describe the basic quantities necessary to describe the transport of radiation. Instead of dealing with rather large numbers of single photons, we use a macroscopic approach in which the radiation field is described by the total amount of energy that is occupied by photons in a specific range of volume, direction of propagation, frequency and time. Therefore, we will mainly deal with radiative intensities, fluxes and mean intensities. We write scalars in roman italics (e.g., I_ν), tensors and matrix quantities in "sans-serif" upright (e.g., P), and vector quantities are denoted in roman bold upright (e.g., $\mathbf{F}$).

Specific Intensity

Astrophysical radiative transfer is based on the concept of the monochromatic specific intensity I_ν. This approach avoids dealing with a phase space distribution function of a photon gas by focussing on the geometry of light propagation on astrophysical scales. Strictly speaking, electromagnetic radiation is a problem determined by Maxwell's equations, which is a rather complex problem to deal with. It is, indeed, necessary when one has to compute scattering coefficients, e.g., for dust particles. But since astrophysical scales are obviously much larger than the wavelength of radiation, we use the approximation of geometrical optics and assume that radiation is propagating along rays through a macroscopic medium. However, both approaches are entirely equivalent, in fact, the definition of the specific intensity is based on the photon distribution function $f(\mathbf{x}, \mathbf{p}, t)$ as being proportional to f via

$$f(\mathbf{x}, \mathbf{p}, t)\, d\mathbf{p} = \frac{1}{h\nu c}\, I(\mathbf{x}, \mathbf{n}, \nu, t), \tag{2.1}$$

where $\mathbf{p}$ is the momentum of the photon, ν is its frequency, $\mathbf{n}$ is the direction of propagation of the photon, and h is Planck's constant. Dealing with radiative transfer in the form of intensities is an intuitive concept as we describe radiation mainly by its flux and energy, avoiding any reference to single photons. This approach is closely connected to astronomical observations in the form of spectra, spectral energy distributions (SEDs) or even images as they mainly describe frequency-dependent radiative energies that are collected by an instrument during a certain exposure time. However, the quantum mechanical characteristics of radiation in this picture come in the form of cross sections and emissivities which determine the interaction of radiation with matter. To stay in this macroscopic picture of radiation, we give another definition of the intensity equivalent to

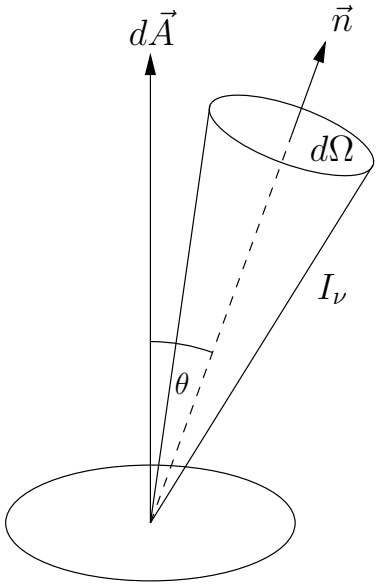

Figure 2.1: The geometrical situation for the definition of the specific intensity I. The vector $d\vec{A}$ is perpendicular to the unit area dA and $\vec{n}$ describes the direction of propagation of the specific intensity.

Equation (2.1):

$$dE = I(\mathbf{x}, \mathbf{n}, \nu, t)\, \frac{A_1 A_2}{r^2}\, dt\, d\nu. \tag{2.2}$$

In this geometrical definition, the specific intensity denotes the radiative energy in the spectral range $[\nu, \nu + d\nu]$ that is emitted in the time interval $[t, t + dt]$ from an area A_1 and gathered by another surface A_2 at a distance r. If r is much larger than the diameter of A_2, the energy reaching A_2 is proportional to the opening angle $d\Omega = \frac{A_2}{r^2}$ (Figure 2.1). Because the specific intensity, in general, is not isotropic, it is a 6-dimensional scalar quantity (3 spatial dimensions, 2 directional + frequency). When we describe the numerical approaches in Chapter 3, we often deal with the so called *grey* approximation in which we use frequency-averaged intensities and opacities. The frequency dependence is then neglected. However, in this chapter, we deal with the theoretical concepts of radiative transfer and for the the reader's convenience, we will not always denote all dimensions explicitly but follow the convention

$$I_\nu = I(\mathbf{x}, \mathbf{n}(\phi, \theta), \nu, t), \tag{2.3}$$

and emphasize specific dependencies by explicitly denoting them. Note that the units of the specific intensity are erg s^{-1} cm^{-2} ster^{-1} Hz^{-1} ("flux per solid angle").

2.1.2 Interaction of Radiation with Matter

As soon as radiation propagates through a medium, it interacts with the present matter. If we consider a beam of radiation travelling through an interactive medium in a certain direction, there are two kinds of interactions that can take place: radiative energy is removed from the beam and/or added. The first event is called an *absorption process* and the latter is regarded as an *emission event*. Either way, there are numerous kinds of absorption and emission processes on the molecular or atomic level that can take place, e.g., photoexcitation, photoionization and recombination, free-free absorption and bremsstrahlung. Photoionization is an important absorption process responsible for the formation of large HII regions around short lived massive stars, which emit radiation mainly in the ultraviolet and are able to ionize their surrounding atomic hydrogen gas. The kinetic energy of free electrons from the ionization process is efficiently thermalized by inelastic collisions which heats up the gas to a few 10^4K and emits energetic photons back into the gas. Another important absorber in GMCs is cosmic dust. Because dust particles are a few micrometer in size, they can efficiently absorb photons in the optical and reemit in the near and far infrared regime. Despite the diversity of absorption and emission processes that can take place in the ISM, interaction processes are usually expressed in the form of a single cross section which includes all absorption processes of interest. Similarly, emission processes are summed up and represented by the emissivity.

So far we discussed absorption and emission processes concerning their effect on the thermal energy of the interacting medium. However, there is another way of removing energy from a beam of radiation without necessarily involving a photon being absorbed. Such an event is called a *scattering process*, and it turns out to be a challenging task to deal with during the numerical solution of the radiative transfer problem. A scattering event occurs if a photon is absorbed by the medium while the energy of this absorption process is not converted into thermal energy. Instead, the molecule or atom, which is excited by the absorption process (e.g. by an photoexcitation process), immediately reemits the photon with only a slight change of its initial energy. While the frequency of the reemitted photon more or less conserves the energy of the originally absorbed photon, the direction of propagation is not (except in a stimulated emission event). This has an effective contribution to the absorption cross section as well as to the emissivity since the scattered photon is removed from a beam of a certain direction and added to another one. In a scattering dominated medium, multiple scattering processes of a photon can transport energy independently of the thermal energy of the medium and couple different regions to each other

in terms of energy exchange. Consequently, the radiation field does not only depend on the local thermal properties of the medium but also on the non-local exchange.
A similar problem occurs if a photon is absorbed, and its energy is actually converted into thermal energy. Since the medium is heated by the photon, it will emit thermal radiation corresponding to the new temperature. Hence, a photon at a different frequency is reemitted into the medium and can be absorbed somewhere else. In this case, radiative transfer in the form of successive absorption and reemission processes can significantly determine the thermal structure of the medium and is very similar to the scattering problem in a numerical sense. We will see that the scattering problem as well as thermal absorption and reemission processes have a profound effect on the RTE.

Extinction Coefficient

To include absorption and scattering events into the radiative transfer model, we introduce the extinction coefficient, which is also often referred to as the *opacity*. The extinction coefficient in general contains a thermal absorption contribution as well as a scattering part:

$$\chi_\nu = \chi_\nu^a + \chi_\nu^s, \tag{2.4}$$

where χ_ν^a and χ_ν^s denote the frequency-dependent coefficients for (thermal) absorption and scattering respectively. The coefficients have the dimension of an inverse photon mean free path (1/length) and are usually calculated from a mass specific cross section κ_ν and the density of the medium ρ by

$$\chi_\nu = \kappa_\nu \rho. \tag{2.5}$$

If the medium is described as a collection of particles, e.g., dust-particles, the mass specific cross section can be regarded as the cross section σ_ν of a single particle divided by its mass m:

$$\kappa_\nu = \frac{\sigma_\nu}{m}. \tag{2.6}$$

For macroscopic particles with a diameter much larger than the wavelength of the radiation involved, the cross section could be regarded as the geometrical cross section, e.g., $\sigma = \pi a^2$ (a is the radius of a spherical particle). In this pure geometrical approach, the cross sections and opacities become frequency-independent (grey). E.g., the typical size distribution of cosmic dust is less than a few tenth of a micrometer which makes them a very efficient absorber in the optical

regime. Nevertheless, in the near, mid and far infrared regimes, the wavelength λ of radiation is typically of the order of the size of the dust particles or less, which requires to treat their cross sections by solving Maxwell's equations with Mie's theory. Other effects like Rayleigh scattering also play a crucial role in the case of $\lambda \ll a$. However complex the theory behind the radiative interaction behaviour might be, the extinction coefficient is the "interface" between these theories and the model of radiative transfer.
Using the inverse mean free path in the form of Equation (2.4) allows us to define the rate of energy density which is removed from a beam by absorption and scattering processes:

$$dE_\nu^- = \chi_\nu I_\nu \, d\Omega. \tag{2.7}$$

Emissivity, Kirchhoff's Law and the Source Function

If we consider a radiative medium, it can also inject radiation into a beam by an emission process. This could be any kind of emission event we discussed above, including a scattered photon which also has an effective contribution to the beam it is added to after the scattering event took place. Formally, we introduce the emissivity η_ν by splitting it into a (thermal) emission and a scattering part

$$\eta_\nu = \eta_\nu^e + \eta_\nu^s. \tag{2.8}$$

The total emissivity then determines the rate of radiative energy density that is injected into a beam:

$$dE_\nu^+ = \eta_\nu d\Omega. \tag{2.9}$$

If the medium acquires a radiative equilibrium state, the radiation field will be completely determined by its temperature T and Planck's law $B_\nu(T)$ respectively. In this case, the medium will always emit the same amount of energy it absorbs which means that

$$\eta_\nu = \chi_\nu B_\nu(T), \tag{2.10}$$

and consequently

$$\frac{\eta_\nu}{\chi_\nu} = B_\nu(T). \tag{2.11}$$

Equation (2.11) is known as the Kirchhoff-Planck relation, and it states that in a radiative equilibrium, emission and absorption actually may take place as long as their ratio satisfies Planck's

law. If for some reasons radiative energy is lost somewhere or an additional source of radiative energy is present, the radiation field may deviate from Planck's law. For these cases, it is useful to introduce a more general quantity for the ratio of emission and absorption processes which is known as the *source function*:

$$S_\nu = \frac{\eta_\nu}{\chi_\nu}. \tag{2.12}$$

2.1.3 The Equation of Radiative Transfer

The RTE describes radiative energy conservation during its propagation through a medium. It is useful to note that the specific intensity has the dimension of "flux per steradian". If we consider a detector with a finite aperture size in a certain distance r from a radiative source, the opening angle which is covered by the aperture scales with r^{-2}. At the same time, the flux which reaches the aperture also scales with r^{-2} so that both effects cancel out each other when we compute the intensity. It is, therefore, very useful to describe radiative transfer in terms of the specific intensity and consider its change along a beam of constant direction $\mathbf{n}$. As we discussed above, the intensity of a beam of light is not supposed to change if no radiative interaction takes place, which means that

$$\begin{aligned} dI_\nu(\mathbf{x}, \mathbf{n}, t) &= \left[I_\nu(\mathbf{x} + c\, ds\, \mathbf{n}, \mathbf{n}, t + dt) - I_\nu(\mathbf{x}, \mathbf{n}, t)\right] dA\; d\Omega\; d\nu\; dt. \\ &= 0. \end{aligned} \tag{2.13}$$

The differential of the intensity is expressed in terms of the displacement ds along the beam:

$$dI_\nu(\mathbf{x}, \mathbf{n}, t) = \left(\frac{\partial I_\nu}{\partial t}\right) dt + \left(\frac{\partial I_\nu}{\partial s}\right) ds, \tag{2.14}$$

and with $dt = \frac{ds}{c}$,

$$dI_\nu(\mathbf{x}, \mathbf{n}, t) = \left[\frac{1}{c}\left(\frac{\partial I_\nu}{\partial t}\right) + \left(\frac{\partial I_\nu}{\partial s}\right)\right] ds. \tag{2.15}$$

The differentiation $\frac{\partial}{\partial s}$ depends on the coordinate system in which I_ν is described. In a Cartesian coordinate system, we can derive

$$\frac{\partial}{\partial s} = \mathbf{n} \cdot \nabla, \tag{2.16}$$

with which we arrive at

$$\frac{1}{c}\frac{\partial I_\nu}{\partial t} + \mathbf{n} \cdot \nabla I_\nu = 0 \qquad \text{in vacuum.} \tag{2.17}$$

Equation (2.17) is the RTE without emission and absorption terms. It is a partial differential equation of hyperbolic type, like the advection equations of hydrodynamics, and it resembles the Boltzmann transport equation for the photon phase space distribution function. The RTE is the conservation law for the radiative energy and, unlike in hydrodynamics, there is no further equation necessary for momentum or mass conservation since there is no force acting between photons and the rest mass of a photon vanishes.

We can now include interaction processes by using the definitions of the extinction and emission coefficients. Equation (2.7) and (2.9) describe sink and source terms for the intensity and are added to the right-hand side of the RTE:

$$\frac{1}{c}\frac{\partial I_\nu}{\partial t} + \mathbf{n} \cdot \nabla I_\nu = \eta_\nu - \chi_\nu I_\nu \qquad \text{in a medium.} \tag{2.18}$$

Conceptually, the RTE in this form could be solved with a Godunov scheme by constructing fluxes, advecting the radiation field through time and account for the source terms with operator-splitting. But this would have to be done on the timescale of the speed of light. However, for the vast majority of radiative transfer problems it is actually a reasonable approximation to assume the RTE to be time-independent. Especially if we want to solve the RTE on the timescale of hydrodynamics, we assume the radiation field to emerge throughout the domain of interest instantaneously. Furthermore, it is often useful to express the RTE in terms of the optical depth. Using the definition of the source function, the time-independent RTE then takes a compact form:

$$\frac{dI_\nu}{d\tau_\nu} = S_\nu - I_\nu. \tag{2.19}$$

where $d\tau_\nu = \chi_\nu ds$ denotes the optical depth along a line element in the direction $\mathbf{n}$. This is the actual form of the RTE we will deal with during the numerical solution in Chapter 3. Although this form of the RTE resembles a simple first-order ordinary differential equation, it requires a proper parameterization for the optical depth in 3D. This can become quite complex if one has to deal with special relativistic or even general relativistic spacetime coordinates. However, these effects are beyond the scope of this work, since we are mainly interested in the radiative energy transport on the scale of typical sound speeds in the ISM. In that case, the complexity of the

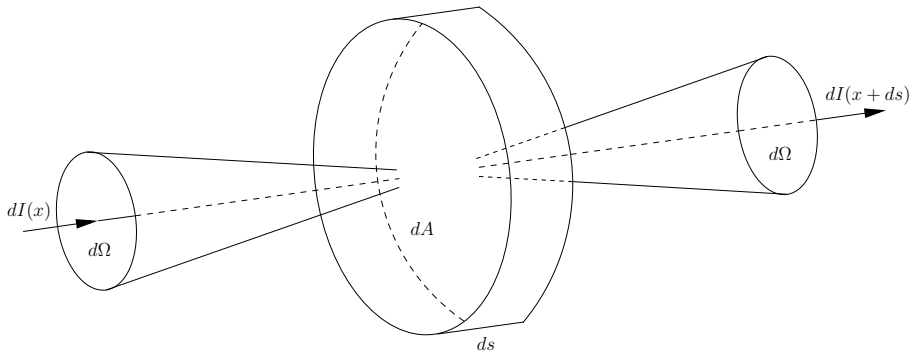

Figure 2.2: The incoming intensity is partly extinct inside the infinitesimal disc of matter. The outgoing intensity is the sum of the remaining incoming intensity and the emitted energy from inside the disc.

model, and hence the solution of the RTE, mainly lies in the formulation of the source function we choose to accurately describe the current radiative transfer problem of interest. (e.g., LTE, NLTE, grey or non-grey, anisotropy, dust continuum radiation, line transfer, etc.). Depending on the model setup, the source function may and, in fact, often does depend on the radiation field itself, which makes the RTE an integro-differential equation. In order to find a self-consistent solution, one has to invoke an iteration scheme of some form. Formally however, if we assume a known source function, the RTE in the form of Equation (2.19) is solved by the formal solution:

$$I(\tau_2) = I(\tau_1)\, e^{(\tau_2-\tau_1)} + \int_{\tau_1}^{\tau_2} S(\tau)\, e^{(\tau_2-\tau)} d\tau. \tag{2.20}$$

The formal solution describes the intensity propagation along a line element with the optical depth $\Delta\tau = \tau_2 - \tau_1$. It contains the incoming intensity $I(\tau_1)$, which may be partially absorbed, and additional energy injected by the source function. With regard to the numerical solution (Chapter 3), we emphasize that the RTE and the formal solution are formally linear in the specific intensity. This will play a crucial role later on in our approach of solving the RTE on a decomposed computational domain such as the adaptive mesh refinement grid embedded in the FLASH code.

2.1.4 The Moment Equations

The specific intensity I_ν contains the whole anisotropic information of the radiation field. It is often much easier to handle radiative transfer problems by reducing this information and integrate the intensity over the whole 4π unit sphere. This is, in fact, an expansion of the intensity

into spherical harmonics. The order of the expansion determines the angular information that is preserved during the integration. For radiative transfer, it is convenient and sufficient to only define the zeroth, first and second order (tensor) moments of the specific intensity:

$$J_\nu = \frac{1}{4\pi} \oint_{4\pi} I_\nu(\mathbf{n}) d\Omega, \tag{2.21}$$

$$\mathbf{H}_\nu = \frac{1}{4\pi} \oint_{4\pi} \mathbf{n} I_\nu(\mathbf{n}) d\Omega, \tag{2.22}$$

$$\mathsf{K}_\nu = \frac{1}{4\pi} \oint_{4\pi} \mathbf{n}\mathbf{n} I_\nu(\mathbf{n}) d\Omega. \tag{2.23}$$

The zeroth moment is the angle-averaged mean intensity J_ν and does not contain any angular information anymore but is closely connected to the radiative energy volume density E_ν. The first moment is a vector quantity which describes the averaged flux of radiative energy $\mathbf{F}_\nu$ while the second moment is a 3×3 matrix connected to the radiative pressure P_ν. The relations are

$$E_\nu = \frac{4\pi}{c} J_\nu, \tag{2.24}$$

$$\mathbf{F}_\nu = 4\pi \mathbf{H}_\nu, \tag{2.25}$$

$$\mathsf{P}_\nu = \frac{4\pi}{c} \mathsf{K}_\nu, \tag{2.26}$$

where c denotes the speed of light. During the computation of the radiation field, we will accumulate the mean intensity J_ν by successively computing the specific intensity for a large number of directions $\mathbf{n}$. This avoids the rather large memory requirement to store the complete field of intensities.

We do the same angular expansion for the RTE (2.18), which becomes necessary to couple it with the equations of hydrodynamics. The approach is the same: we first multiply the RTE successively with 1 and $\mathbf{n}$ and integrate it over solid angles. We use the expressions for the radiative energy, flux and pressure (Equations (2.24)-(2.26)) and arrive at

$$\frac{\partial E_\nu}{\partial t} + \nabla \cdot \mathbf{F}_\nu = 4\pi\eta_\nu - \chi_\nu c E_\nu, \tag{2.27}$$

$$\frac{1}{c}\frac{\partial \mathbf{F}_\nu}{\partial t} + c\,\nabla \cdot \mathsf{P}_\nu = -\chi_\nu \mathbf{F}_\nu. \tag{2.28}$$

We assumed that the emissivity η_ν has no angle dependence so that its angular integration vanishes if multiplied with $\mathbf{n}$ in the first moment equation. Unfortunately, each moment equation introduces the next higher moment of the intensity, e.g., in the first moment equation the second moment (the radiative pressure tensor) appears. Hence, the set of moment equations up to a certain order is always short of one equation in order to close the system. We will see that the same happens with Euler's equations of hydrodynamics although they are much easier to close if we assume an ideal gas equation of state (EOS) which relates the thermal pressure to the internal energy. The situation with the radiative pressure tensor and energy is much more complex because of the high-dimensionality of the radiation field. The equations must be closed by an ad hoc relation, e.g., the Eddington approximation with is often used in the diffusion limit or by explicitly computing the angular dependence of the K_ν-tensor according to Equation (2.23).

2.2 Hydrodynamics

The topic of hydrodynamics deals with the description of time-dependent or stationary flows of fluids and gases. The equations of hydrodynamics are used in almost all fields of astrophysics, meteorology, climate sciences, geophysics or engineering where the motion of fluids or gases is used for modelling. In basically all these research fields, the equations of hydrodynamics are already so complex that they can not be solved without numerical techniques. The reason for this is that the continuum description of a fluid must include mass, momentum and energy conservation which are coupled in a highly non-linear set of hyperbolic equations, the Euler equations. In astrophysics, the applications reach from modelling star and planet formation, the formation of galaxies and even the evolution of whole clusters of galaxies in the early universe (Springel et al., 2005; Vogelsberger et al., 2014). As diverse as the applications are the methods to solve them. In astrophysics, one typically has to deal with compressible gas motions in 3D which might be highly supersonic and involve strong shocks. The motion of gas in the ISM produces high density contrasts and turbulent fluid features on a wide range of length scales which requires sophisticated numerical schemes to solve the Euler equations for such complex environments.

Additional physics also play a crucial role in astrophysical hydrodynamics. A proper treatment of gravity is often indispensable and not entirely trivial as an interstellar gas is usually dominated by its self-gravity which requires the solution of the Laplace equation for the gravitational potential. Sophisticated chemistry can influence the thermodynamics and have a profound effect on the

hydrodynamical quantities. Furthermore, magnetic fields have been shown to play an important role in a wide range of astrophysical problems, including stellar atmospheres, the formation of stars, discs, planets, stellar winds and jets. Including magnetic fields in the equations of hydrodynamics takes much more care than, e.g., the gravitational potential. Since a magnetic field carries additional pressure, force and energy, the equations of magnetohydrodynamics require modified solution schemes to ensure conservation of mass, energy and momentum and guarantee a divergence-free magnetic field. Finally, including the effects of the radiation field requires the combined solution of the Euler equations and the equation of radiative transfer. Similar to the gravitational potential, radiative transfer on the timescale of hydrodynamics is in general a non-local problem in contrast to the Euler equations which are entirely determined by local fluxes of mass, momentum and energy. Like the magnetic field, the radiation field exerts an additional pressure on and exchanges energy with the gas while radiative forces may influence momentum conservation.

In the following sections, we describe the basic equations of hydrodynamics for an ideal fluid. The focus lies on the coupling of the equations of hydrodynamics with the moment equations of radiative transfer. Therefore, we neglect the effects of the magnetic field for now. However, a detailed description of the equations of magnetohydrodynamics with radiative transfer is given in the following Chapter 3 which focuses on numerical methods.

2.2.1 Ideal Fluids

In this work, we use the term *fluid* and *gas* interchangeably as in astrophysics one usually refers to gases as fluids and vice versa. We focus on the description of fluids in terms of continuum mechanics, in which one deals with continuous quantities rather than with discrete fluid particles. There is some freedom in the choice of a set of variables to describe fluids. Sometimes it is useful to describe a fluid by a set of primitive variables, which are the mass density ρ, pressure p and the velocity field $\mathbf{v}(u, v, w)$ with the x-component u, the y-component v and the z-component w. Those are the physical variables of the fluids one actually can measure and analyze. Numerically, it is rather common to use the set of conserved variables, which are the mass density ρ, the x-component ρu, y-component ρv and z-component ρw of the momentum and the energy density (energy per unit volume) E. The conserved variables appear in the fluxes of the Euler equations and are used to evolve the dynamics of the fluid. For this work, we assume the gas to be

ideal and characterized by its density, pressure and temperature or internal energy respectively. For typical densities and temperatures of the ISM, the ideal gas assumption is very accurate and widely used for astrophysical problems (except the interiors of stars or gaseous planets). For hydrodynamics, this has the advantage that we can use the rather simple ideal gas EOS for closing the Euler equations. Since the conserved variables are determined by the hydrodynamics, we use a caloric gamma EOS in which the pressure is related to the specific internal energy (energy per unit mass) e_{int} and density of the gas:

$$p = (\gamma - 1)\rho e_{\mathrm{int}} \tag{2.29}$$

where γ is the ratio of specific heats which is determined by the degrees of freedom of the particles in the gas. We will usually assume $\gamma = 5/3$ which corresponds to a mono-atomic (hydrogen) gas. The temperature is also related to the internal energy by:

$$e_{\mathrm{int}} = c_v T, \tag{2.30}$$

$$c_{\mathrm{V}} = \frac{k_b}{\mu m_{\mathrm{p}}}, \tag{2.31}$$

where k_b is the Boltzmann constant, m_{p} the proton mass and μ the mean molecular weight of the gas.

We should note that the ideal fluid assumption is, of course, not unconditionally valid since the uncertainty in the Boltzmann statistics is not included. Describing the fluid with the macroscopic quantities ρ, p, $\mathbf{v}$ and e requires that we can define a certain control volume in which these quantities are valid. The ideal gas assumption requires that such a control volume can be chosen to be negligible in size compared to the typical scale of the fluid flow. At the same time, the control volume has to be large enough so that the average of statistical uncertainties in the motion of single atoms or molecules vanishes. This requires that the mean free path of collisions between single particles in the gas is negligible compared to the macroscopic net flow of the fluid. Clearly, the mean free path depends inversely on the fluid density and compared to the densities of, e.g., air flows in the Earth's oceans or atmospheres, interstellar gas densities might seem fairly low (e.g. 1 particle per cm^3). But because of the large scales of the overall gas motions in the ISM, we can choose the size of a control volume to be much larger than the mean free path of an interstellar fluid particle, and yet it will still be negligible in size compared the typical length scale of features

in the fluid flow.

2.2.2 Euler's Equations

In continuum mechanics, the motion of an ideal fluid is entirely determined by conservation of mass, momentum and energy. The change over time of one of these conserved variables in a certain control volume has to compensated by a flux of the variable through the surface of this volume. Hence, the conservation equations are naturally derived from the integral form by computing net fluxes of mass, momentum and energy through the surface of the control volume. Using Gauss's theorem, the governing system of conservation laws is then usually expressed in a set of partial differential equations.

Conservation of Mass

The mass of all particles has to be conserved. This means that the rate of change of the mass in a fixed volume V has to be compensated by the mass flux through its surface S. Integrating the mass flux over the surface S yields the total flux so that the rate of change becomes

$$\frac{d}{dt}\int_V \rho \, dV = -\int_S \rho \mathbf{v} \, d\mathbf{S}. \tag{2.32}$$

This has to be true for any control volume we might choose. Using Gauss's theorem we can express the conservation of mass in partial differential form

$$\frac{\partial \rho}{\partial t} + \nabla \cdot (\rho \mathbf{v}) = 0, \tag{2.33}$$

where $\rho\mathbf{v}$ is the mass flux.

Conservation of Momentum

The conservation law for the momentum ($\rho\mathbf{v}$, which equals the mass flux) follows in a similar way as the conservation of mass. However, momentum can not only change because of the flux associated with the velocity field ($\rho\mathbf{v}\mathbf{v}$) but also due to pressure forces p that act on the surface of a gas parcel. In integral form, the total change of rate of momentum is again derived from

considering a control volume V with surface S:

$$\frac{d}{dt}\int_V \rho\mathbf{v}\,dV = -\int_S \rho\mathbf{v}\mathbf{v}\cdot d\mathbf{S} - \int_S p\,d\mathbf{S}. \tag{2.34}$$

In partial differential form this becomes

$$\frac{\partial\rho\mathbf{v}}{\partial t} + \nabla\cdot(\rho\mathbf{v}\mathbf{v} + p1) = 0. \tag{2.35}$$

The term $(\rho\mathbf{v}\mathbf{v} + p1)$ is the stress tensor of the fluid (1 denotes the unity matrix). The thermal bulk pressure p is isotropic since it only appears in the diagonal of the stress tensor which is a 3×3 matrix. The bulk pressure is responsible for uniform compression or expansion of a fluid element. In contrast, the velocity field can create shear forces which are determined by the non-diagonal elements of the tensor product $\mathbf{v}\mathbf{v}$ (which is sometimes explicitly denoted by $(\mathbf{v}\otimes\mathbf{v})$). Taking the divergence of the $\mathbf{v}\mathbf{v}$-tensor gives again a vector, and we actually get three advection equations for each component of the momentum. To make this clear, it is useful to write the momentum conservation law explicitly for each component of the velocity field $\mathbf{v}(u,v,w)$. In Cartesian coordinates we get

$$\partial_t(\rho u) + \partial_x(uu+p) + \partial_y(uv) + \partial_z(uw) = 0, \tag{2.36}$$

$$\partial_t(\rho v) + \partial_x(vu) + \partial_y(vv+p) + \partial_z(vw) = 0, \tag{2.37}$$

$$\partial_t(\rho w) + \partial_x(wu) + \partial_y(wv) + \partial_z(ww+p) = 0. \tag{2.38}$$

If an external force is present, it appears in the momentum equation as a source term (a momentum source rate per unit volume). For our purposes, this is the self-gravity of the fluid. If the gravitational potential Φ is known, it can be added to the fluid momentum in an operator-splitting step. The actual momentum conservation law then reads

$$\frac{\partial\rho\mathbf{v}}{\partial t} + \nabla\cdot(\rho\mathbf{v}\mathbf{v} + p1) = -\rho\,\nabla\Phi. \tag{2.39}$$

The gravitational potential is determined by the Poisson equation

$$\Delta\Phi = 4\pi G\rho, \tag{2.40}$$

where $\Delta = \nabla\cdot\nabla$ is the Laplace operator and G the gravitational constant.

Conservation of Energy

The fluid can carry energy in many forms. For the formulation of its conservation law, we have to consider internal energy and mechanical energy. The first law of thermodynamics supplies a conservation law for the internal energy which changes due to heating and work done by the pressure. A change of mechanical energies due to forces acting on a fluid parcel can be derived from the momentum conservation law in Equation (2.39). Combining both, we actually end up with an energy equation that includes the flux of internal energy and kinetic energy plus work done by the pressure. Following our approach of considering a control volume we get

$$\frac{\partial}{\partial t}\int_V \rho\left(e_{\text{int}} + \frac{1}{2}\,\mathbf{v}^2\right) dV = -\int_S \rho\left(e_{\text{int}} + \frac{1}{2}\,\mathbf{v}^2\right)\mathbf{v}\cdot d\mathbf{S} - \int_S p\,\mathbf{v}\cdot d\mathbf{S}. \tag{2.41}$$

We again rewrite this in partial differential form and include external heat sources and changes due to work done by gravitational forces

$$\frac{\partial E}{\partial t} + \nabla\cdot(E+p)\mathbf{v} = Q_{\text{ext}} - \mathbf{v}\cdot\nabla\Phi, \tag{2.42}$$

where $E = \rho\,(e_{\text{int}} + 0.5\,\mathbf{v}^2)$ denotes the total energy density (internal + kinetic energy per unit volume). We should note that Euler's equations are not the only way of describing the dynamics of the conserved variables. They are however the equations of choice to handle the fluid dynamics in a fixed rest frame like the spatial grid in a numerical discrete-volume computer code. Euler's equation then come in very handy since they naturally describe the change of variables by fluxes through the surface of control volumes. Another way of handling the equations of hydrodynamics is from a Lagrangian point-of-view. In the Lagrangian form, the motion of a fluid parcel is described in its comoving frame and the comoving derivative

$$D_t = \partial_t + \mathbf{v}\cdot\nabla \tag{2.43}$$

replaces advection terms due to the velocity field. The equations turn out to be slightly more compact than Euler's equations but are also more difficult to solve numerically using smoothed particle hydrodynamical computer codes.

2.3 Hydrodynamics with Radiation

We now consider the equations of hydrodynamics including the effects of radiative transfer. We already mentioned that the right-hand side of Equation (2.19) accounts for absorption and emission processes. To couple these source terms into Euler's equations, we integrate them over frequency to obtain the energy g^0 and momentum $\mathbf{g}$ exchange rates

$$g^0 = \int d\nu \int d\Omega \, (\eta_\nu - \chi_\nu I_\nu), \tag{2.44}$$

$$\mathbf{g} = \frac{1}{c} \int d\nu \int d\Omega \, \mathbf{n} \, (\eta_\nu - \chi_\nu I_\nu). \tag{2.45}$$

The notation g^α indicates that the exchange rates are related to the components of the radiation four-force density (Mihalas and Weibel Mihalas, 1984, Section 94) in the four-dimensional Minkowski spacetime. In the Euler equations, the exchange rates appear on the right-hand side of the momentum and energy equation

$$\frac{\partial \rho \mathbf{v}}{\partial t} + \nabla \cdot (\rho \mathbf{v}\mathbf{v} + p\mathsf{1}) = -\mathbf{g}, , \tag{2.46}$$

$$\frac{\partial E}{\partial t} + \nabla \cdot (E + p)\mathbf{v} = -g^0 - \mathbf{v} \cdot \nabla \Phi.. \tag{2.47}$$

Now we can connect the exchange rates to the frequency-integrated moment equations 2.27-2.28 and sum them them with the Euler equations to obtain

$$\frac{\partial}{\partial t} \left(\rho \mathbf{v} + \frac{\mathbf{F}}{c^2} \right) + \nabla \cdot (\rho \mathbf{v}\mathbf{v} + p\mathsf{1} + \mathsf{P}) = -\rho \nabla \Phi, , \tag{2.48}$$

$$\frac{\partial}{\partial t} (E + E_r) + \nabla \cdot (\rho E + p)\mathbf{v} + \nabla \cdot \mathbf{F} = -\mathbf{v} \cdot \nabla \Phi.. \tag{2.49}$$

These are the inertial frame equations of radiation hydrodynamics where E_r, $\mathbf{F}$ and P are the bolometric radiative energy density, flux and pressure respectively.

3

Numerical Methods

In this chapter, we present in detail our approach of solving the radiative transfer equation (RTE) in the framework of the FLASH code. We discuss the method of hybrid characteristics (Rijkhorst et al., 2006) that is the basis for our solution of the radiative transfer problem in an adaptive mesh refinement (AMR) code. We also show the substantial improvements made by others (Peters et al., 2010) and us to make this method feasible for massively parallel radiation hydrodynamical simulations. Although the focus of this chapter lies on the numerical methods to deal with radiative transfer, we also give a brief introduction into the basics of numerical hydrodynamics with a focus on the coupling of our radiative transfer solver with the FLASH code.

3.1 Introduction

Radiative transfer has a long tradition in the field of stellar physics where radiation plays a crucial role in the inner radiative zone of a star as well as in the stellar atmosphere where light emerges from the photosphere. Modelling radiative transfer is a very challenging field of computational physics although the mathematical formalisms behind the RTE might be quite basic. In the

inner regions of a star like our sun, radiative transfer can be described as a diffusive process since the inner regions are highly optically thick. In the transition region from the convective zone to the stellar atmosphere, this is no longer the case since the mean free path of a photon becomes much larger than than the range on which temperatures change substantially. The radiation field decouples from local thermodynamical properties of the gas which prohibits a diffusion approximation in such an NLTE situation. However, our focus lies on radiative transfer in the field of star formation theory, where radiative transfer plays a crucial role as an important cooling mechanism during the formation of the protostar and the following accretion processes. If one considers massive star formation in a cluster-like environment (e.g., Peters et al., 2010), ionizing radiation is a highly dynamic feedback process which determines the accretion rate of the massive star itself but also has an influence on ongoing star formation in the overall cluster. In this context, radiative transfer is a rather costly computation compared to solving the equations of hydrodynamics or magnetohydrodynamics (MHD). The reason for this is that the timescale of radiative transfer is usually much shorter than those of hydrodynamics and MHD because of the large speed of light compared to the sound speed of the gas in, e.g., a molecular cloud or the characteristic Alfvén wave speeds of the magnetic field. The short timescale on which radiation emerges throughout the complete computational domain makes radiative transfer a highly non-local problem compared to hydrodynamics which is determined completely by local thermodynamic properties of the gas. In this sense, hydrodynamics and radiative transfer are two very different numerical tasks and very challenging to solve consistently. Modern Eulerian MHD codes like FLASH mostly solve the Euler equations on a grid with AMR to resolve fluid features on a wide range of length scales. These codes are parallelized by subdividing the computational domain into several subdomains each containing a fixed number of cells. Since the Euler equations describe local fluxes of mass, momentum and energy, all subdomains can be handled in parallel during a hydrodynamical time step. Between the time steps, boundary values of the subdomains are exchanged using the Message Passing Interface (MPI) for communication. In contrast, characteristics based radiative transfer codes are usually designed very differently. Instead of domain decomposition, these codes are parallelized exploiting the formal independence of the RTE on the solid angle. Resolving the anisotropy of the radiation field accurately requires a large set of characteristics each covering a discrete opening angle of the 4π unit sphere. If all radiative quantities are assumed fixed during one solution step, characteristics of different directions can be computed independently of each other which makes it ideal for parallelization. However, the spatial information of the computational domain with all radiative quantities

has to be available to the each processor computing a certain number of characteristics on the solid angle grid. This can be a severe drawback in terms of memory requirement if high spatial resolution is required or a large number of frequencies or both (e.g, synthetic stellar spectra). Solving both the Euler equations and the RTE consistently requires careful approximations to the radiative transfer problem to make the coupling of a hydrodynamical code with a radiative transfer code feasible. van Noort et al. (2002) presented a radiation solver that is coupled to a hydrodynamical code using AMR and domain decomposition in 2D. The radiation solver invokes short characteristics for integrating the RTE while boundary values are communicated between Lambda iteration steps. The focus of this approach lies on modelling the dynamics of scattering-dominated stellar atmospheres. The short characteristics approach allows for a fast converging Gauss-Seidel iteration scheme (.e.g., Trujillo Bueno and Fabiani Bendicho, 1995), while non-local contributions have to be communicated by a successive exchange of boundary values between subdomains. This approach was even extended for 3D simulations (e.g., Hayek et al., 2010; Davis et al., 2012). However, while the Gauss-Seidel short characteristics approach is well suited for highly scattering dominated regimes, it introduces a lot of numerical diffusion because a large number of upwind interpolations is necessary. Successive communication of boundary values was also used with long characteristics in 3D (Heinemann et al., 2006) although their approach does not include AMR.

Another completely different approach for including radiative transfer in hydrodynamical simulations is based on the diffusion approximation of the angular moment equations. In regions of high opacities χ, the diffusion approximation is an expansion of the specific intensity in which all terms $\propto 1/\chi$ are neglected in the RTE. This leads to Eddington's approximation in which the isotropic radiation pressure is proportional to the radiation energy density. The moment equations of the radiative intensity themselves then form a set of hyperbolic equations, like the Euler equations of hydrodynamics. However, since those two hyperbolic systems would still have to be handled on their individual timescales, one can even make one further step and neglect the time dependence of the radiation flux by assuming it to be proportional to the gradient of the radiation energy (Fick's law). The moment equations can then be combined into a single diffusion equation for the energy of the radiation field. Because the flux in the diffusion approximation lost its finite propagation speed, one has to introduce a flux-limiter to avoid unphysical propagation speeds depending on the actual opacity. This *flux-limited diffusion approximation* (FLD) (Levermore and Pomraning, 1981) has been successfully used in radiation hydrodynamical star formation simulations coupled within Eulerian grid codes (e.g.

Krumholz et al., 2007a; Commerçon et al., 2011) as well as smoothed particle hydrodynamics (SPH) codes (e.g. Bate et al., 2013). However, the diffusion approximation is only valid in optically thick regions where the radiation field becomes isotropic. Kuiper et al. (2010) have shown the significant drawbacks of using FLD in the transition regions from optically thick to optically thin regimes where the radiation field becomes highly anisotropic. Recent efforts have been made to combine raytracing methods with FLD solvers (Kuiper et al., 2010; Flock et al., 2013) to handle primary stellar or protostellar radiation separately from the FLD approximation and to avoid the stellar flux from diffusing into shadow regions.

Finally, Monte Carlo (MC) methods have become increasingly popular during the last decade, especially in post-processing MHD simulations. The MC method is a statistical approach and treats individual photons or photon packages by following its propagation path and computing absorption, emission and scattering probabilities. Several advances have been introduced, e.g., photon peel-off (Lucy, 1999), immediate reemission (Bjorkman and Wood, 2001) and diffusion approximations (Min et al., 2009) which make the MC method a powerful tool to calculate synthetic spectra, spectral energy distributions or polarization maps from the outcome of MHD simulations. The angular and frequency resolution are, in principle, unlimited since the direction of propagation of a photon package and its frequency are chosen randomly from a continuous probability function. In that sense, the MC method always gives a quite reasonable result even in the limit of a small number of photon packages while a low resolution shows mainly up as statistical noise in the solution. But the statistical approach also has a severe drawback since we do not know in advance the exact path a photon package will travel, and how and when it is emitted or absorbed. Therefore, it is extremely difficult to implement on a decomposed domain. MC methods are extremely successful in post-processing the outcome of MHD simulations but are rarely used in combination with hydrodynamical simulations. Those approaches which does include MC methods (e.g. Acreman et al., 2010) are fairly restricted in their spatial resolution of the AMR grid, since each processor has to get a copy of the complete computational domain to be able to follow the path of an arbitrary photon package. For our approach, we therefore choose a discrete ordinate method using characteristics to integrate the RTE which requires a raytracer that works on an AMR grid with domain decomposition.

In the following sections, we describe our efforts of implementing a new characteristics based solver for the RTE. The solver is implemented in the FLASH code and is able to handle AMR as well as domain decomposition for parallelization.

3.2 Characteristics based Radiative Transfer

Characteristics based radiative transfer is a discrete ordinate method. In addition to the spatial discretization, all other ordinates (e.g., angular resolution, frequency) of the radiation field are discretized intro grid points or cells as well. The RTE is solved for each discretization point on these grids and the full 3D and polychromatic solution is obtained. The spatial integration of the RTE is achieved by casting a ray, or *long characteristic*, through the grid and integrate the RTE along this ray. This requires a discretization of the RTE.

3.2.1 Parameterization and Discretization of the Radiative Transfer Equation

In general, the method of characteristics is an approach of solving a partial differential equation (PDE), just like the RTE, by reducing it to a parameterized ordinary differential equation (ODE). We recall the 3D RTE here:

$$\frac{1}{\chi}\,\mathbf{n}\cdot\nabla I = S - I. \tag{3.1}$$

In a Cartesian coordinate system we can express the position along a ray in the direction $\mathbf{n}$ using an arbitrary point of origin $\mathbf{o}$ and a ray parameter s according to

$$\mathbf{x} = \mathbf{o} + s\mathbf{n}, \tag{3.2}$$

from which immediately follows that

$$\frac{\partial \mathbf{x}}{\partial s} = \mathbf{n}. \tag{3.3}$$

Now we can express the left-hand side of the 3D RTE in parameterized form

$$\begin{aligned}
\frac{1}{\chi}\mathbf{n}\cdot\nabla I &= \frac{1}{\chi}\frac{\partial \mathbf{x}}{\partial s}\cdot\nabla I && (3.4)\\
&= \frac{1}{\chi}\left(\frac{\partial x}{\partial s}\frac{\partial I}{\partial x} + \frac{\partial y}{\partial s}\frac{\partial I}{\partial y} + \frac{\partial z}{\partial s}\frac{\partial I}{\partial z}\right) && (3.5)\\
&= \frac{dI}{d\tau}. && (3.6)
\end{aligned}$$

The partial differential 3D RTE now reduces to an ordinary differential equation in the optical depth along the ray in direction $\mathbf{n}$:

$$\frac{dI(\mathbf{n})}{d\tau(\mathbf{n})} = S - I(\mathbf{n}). \tag{3.7}$$

In order to find an accurate 3D solution, Equation (3.7) has to be solved for a large number of rays defined by Equation (3.2) which determines the solution of the 3D RTE for a discrete point of origin and direction. Of course, the method of characteristics it not restricted to the parameterization in Equation (3.2) but can be used for any other PDE with a suitable parameterization. E.g., for the solution of the Euler equations, one usually refers to a characteristic as being the propagation of eigen-states along the "direction" of the eigenvector, and the eigenvalues define the propagation speed. The concept is similar in the way that the non-linear Euler equations are reduced to the propagation of independent 1D eigen-signals while in the case of the RTE, we reduce the 3D solution into a number of independent 1D solutions along a parameterized characteristic.

Olson et al. (1986) introduced the solution of the 1D RTE by using a discretized form of the formal solution 2.20. The RTE is integrated for each cell in the computational along a characteristic according to

$$I(\tau_i) = I_{i-1} \ \exp\left(-\Delta\tau_{i-1}\right) + \Delta I_i \tag{3.8}$$

where $\Delta\tau_i$ is the finite optical depth element given by a piecewise linear interpolation

$$\Delta\tau_i = \frac{1}{2}(\chi_{i-1} + \chi_i)\Delta s.$$

χ_i is the opacity at the discretization point s_i on the characteristic. ΔI_i is the discretized counterpart to the integral in the formal solution (Equation (2.20)) and is solved by either a linear or parabolic interpolation of the form

$$\Delta I_i = \alpha_i S_{i-1} + \beta_i S_i + \gamma_i S_{i+1}. \tag{3.9}$$

In the case of linear interpolation, the γ coefficient vanishes. The coefficients α_i, β_i and γ_i depend on the optical depths between s_{i-1}, s_i and s_{i+1}. They are given in Olson et al. (1986). Figure 3.1 shows the geometrical situation of a characteristic passing through a homogeneous grid at an

arbitrary direction $\mathbf{n}_j(\theta, \phi)$. Since the opacity and source function are stored in the cell centers of the finite volume hydrodynamical grid (dashed lines), the cell centers define the vertices of the radiative transfer grid (solid lines). The characteristic is traced on the radiative transfer grid using a modified version of the fast voxel traversal algorithm introduced by Amanatides and Woo (1987). The opacity χ_i and the source function S_i at the intersection points of the characteristic with the grid are then interpolated bilinearly from the adjacent vertices.

Characteristics based radiative transfer is basically the attempt to approximate the radiative interaction of each cell with each other cell in the computational domain. Although the method of long characteristics is very accurate in doing this, it is rather inefficient as it requires to shoot a large number of rays for each cell to sample the radiation field accurately in 3D. An alternative is to use a short characteristics approach, in which only neighbouring cells are used to interpolate incoming intensities from different directions. This requires to sweep the cells in an ordered fashion to make sure that all intensities, which are required for interpolation, are available. The short characteristics approach introduces a lot of numerical diffusion because of the large number of interpolations involved but reduces the cost of the radiative transfer calculations significantly. Either way, the method of characteristics requires a raytracer, which samples radiative interactions between arbitrary regions in the computational domain to account for non-local radiative coupling.

While the RTE is integrated along each direction $\mathbf{n}$, the mean intensity is computed by accumulating all intensities:

$$J = \frac{1}{4\pi} \sum_{\mathbf{n}} I(\mathbf{n}) \Delta\Omega \tag{3.10}$$

where $\Delta\Omega$ denotes the finite solid angle which the characteristics along $\mathbf{n}$ covers.

Point Sources

Depending on the anisotropy of the radiation field the resolution of the solid angle grid is crucial to the accuracy of the solution. If the radiation field is dominated by a few compact sources, one has to assure that each cell is connected to these sources radiatively. In those cases, it is preferable to compute the radiative flux the other way round: Instead of tracing parallel rays for each cell, we directly compute the intensity with respect to the source for each cell. An extreme example would be a singular point source, e.g., a star which injects radiation into its environment in a highly collimated manner. From the point of view of a distant observer (or cell), the intensity

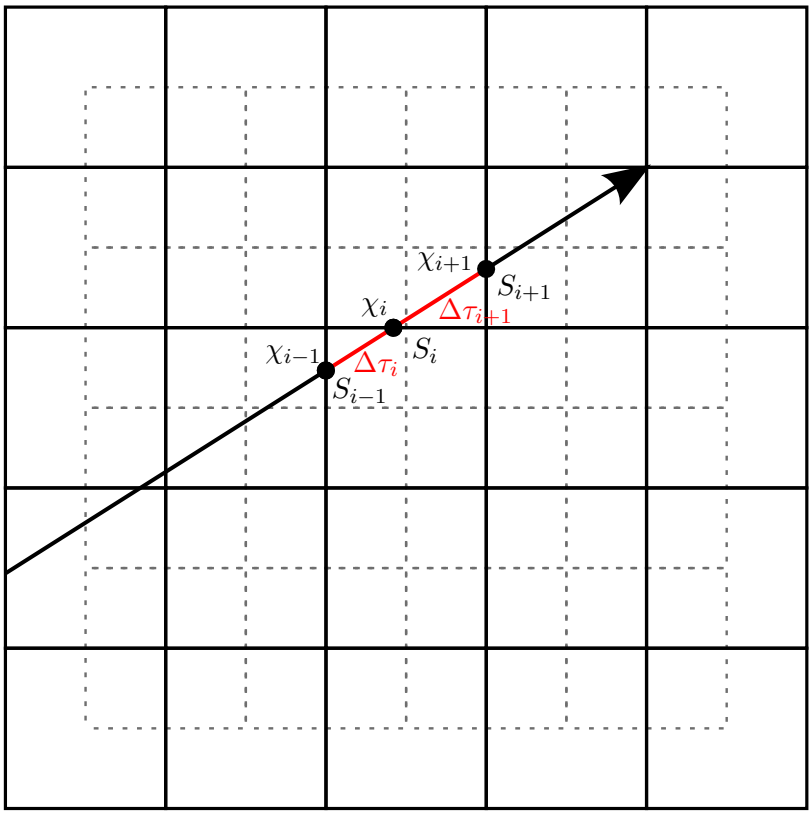

Figure 3.1: The staggered radiative transfer grid (solid lines) defined by the cell centers of the underlying finite volume hydrodynamical grid (dashed lines). A long characteristic at an arbitrary direction is shown which integrates the RTE for the hydro cell center at the upper right corner of the domain. Boundary values are obtained from guard cells that hold values from neighbouring subdomains.

that reaches the observer at position $\mathbf{x}$ from a point source at position $\mathbf{x}_*$ is

$$I_\nu^*(\mathbf{x}) = \frac{L_\nu^*(\mathbf{x})}{4\pi r^2} \exp(-\tau_*), \tag{3.11}$$

where r denotes the distance from the observer to the star, and L_ν^* is the stellar luminosity. If the location of a source is known it is much easier to treat it explicitly by computing the optical depth τ_* to each cell and adding its intensity contribution to the mean intensity.

3.2.2 Raytracing on the decomposed AMR Grid

The integration of the RTE requires a raytracer since we have to compute path lengths and optical depths in order to do the quadrature from Equation (3.9). Figure 3.1 shows how this is done in general on a homogeneous grid. However, the parallel design of the FLASH framework, in which our solver is currently implemented, forbids to raytrace over the entire domain which is necessary for the method of characteristics (Figure 3.2). FLASH invokes PARAMESH (Olson et al. (1999)), and lately also the CHOMBO library[1], for implementing an AMR grid. PARAMESH uses a block structured adaptive mesh, in which the fundamental data structure is a block containing cells which are logically indexed by a coordinate triple (i,j,k). The entire computational domain consists of a number of blocks of different physical sizes ordered hierarchically in an octree data structure. Blocks at the bottom of the octree, called *leaf blocks*, contain valid data, and they cover the entire physical size of the computational domain. FLASH allows for massively parallel computation by using the Message Passing Interface (MPI) for the communication of guard cell information between the blocks of the AMR grid. Optimal load balancing is guaranteed by splitting the AMR tree equally between all available MPI tasks to ensure that each task receives more or less the same number of leaf blocks. E.g., the AMR tree of a star formation simulation typically requires more than 10 levels of spatial resolution with up to several 10^5 blocks each containing 8^3 cells. This is only possible (in terms of CPU time and memory requirements) by the parallelization scheme described above.

The method of characteristics stays in direct contrast to the spatial parallelization of the AMR grid. As soon as we want to raytrace on an AMR grid with domain decomposition, there are two main problems we encounter. First, we need a raytracer that is working adaptively on the multiple resolutions of an AMR grid. Second, we need to exchange boundary contributions not only

[1] https://seesar.lbl.gov/anag/chombo/

between adjacent subdomains but from all subdomains that have a significant radiative contribution. For these purposes, we adapt a raytracing technique originally developed by Rijkhorst et al. (2006) and improved by Peters et al. (2010), which uses a combination of local long characteristics and a global "short-characteristics-like" interpolation of outgoing intensities from the decomposed domains of the AMR grid. The basic idea is to split the radiation field into two components:

- 1. A local component, that uses long characteristics to compute only radiative contributions from inside the subdomain (block) to both the cells inside the block as well as contributions that leave the subdomain (*face values*). The computation is done in parallel and in accordance with the design of the block structured AMR grid.

- 2. A global component, which is computed by communicating and accumulating the face values. This step requires raytracing the block structure of the AMR tree and the interpolation of face values, very similar to the short characteristics method (but on the level of subdomains/blocks). After the communication of the face values and the tree hierarchy, this step is also done in parallel.

This approach, called *hybrid characteristics*, only needs to communicate the face values of the subdomains and information about the AMR tree hierarchy but no 3D data. By this, the amount of communicated data is reduced significantly. Originally, this method was developed by Rijkhorst et al. (2006) to compute column densities with respect to point sources for UV ionization. The original method required to communicate the whole AMR tree structure at the highest level of spatial resolution during the raytracing step on the AMR block structure. This stands in contrast to the parallel design of the FLASH code and restricts the available range of refinement levels of the AMR tree substantially because of the large memory overhead. Peters et al. (2010) added some major improvements to the algorithm by introducing a walk through the AMR tree, which only requires the communication of basic AMR information and conserves the idea of shared memory parallelization. However, raytracing on the block structure was still done on the highest refinement level to conserve the proper block indexing. Obviously, this slows down the algorithm significantly if a high range of resolution is required, even though the domain may not even have reached the highest refinement level during the computation. For this work, we improved the AMR tree walk by using a dynamic ray parameter during the block raytracing step. Choosing the optimal ray parameter for each block depending on its refinement level in the tree guarantees a fast and adaptive way of finding the blocks and their corresponding face values which are cut by

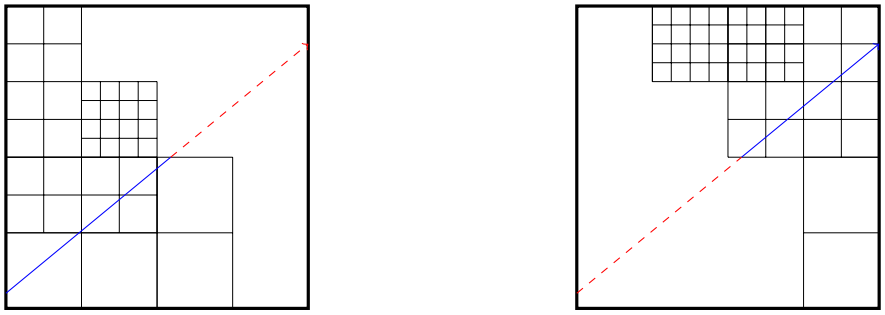

Figure 3.2: Example for a 2D AMR grid distributed over two processors without shared memory. Local raytracing through the domain is obviously restricted to the subdomain each processor is assigned to.

the current ray (see Figure 3.3). In addition, we implemented a new raytracer which, in addition to the contributions from point sources, can sample the radiation field for an arbitrary number of directions and angles. And finally, we added a full radiative transfer module which uses the raytracer to compute stepwise formal solutions according to Equation (3.8) along parallel rays. This enables us to account for the effects of the diffuse radiation field. Figure 3.4 shows a 2D example of a simple test setup with an irradiated central density clump using adaptive mesh refinement. The figure shows the ability of the method to create sharp shadows and to transport incoming radiation over the entire domain.

3.2.3 The Lambda Formalism

Computing the radiation field in the form of the mean intensity in Equation (3.10) requires a formal solution of the RTE in the way described above. Usually, this task is described in a rather compact form by using the *Lambda Operator*:

$$J = \Lambda[S]. \tag{3.12}$$

Formally, the Lambda operator for *one cell* in the computational domain contains the radiative contributions from each other cell. The construction of the operator would require to explicitly calculate the radiative coupling between a cell and each other cell. But this is far too costly concerning computation time and memory requirements. Instead, we do not construct the operator but we approximate the Lambda step from Equation (3.12) by using the formal solution from Equation (2.20) to compute the radiation field J from the source function S in the way de-

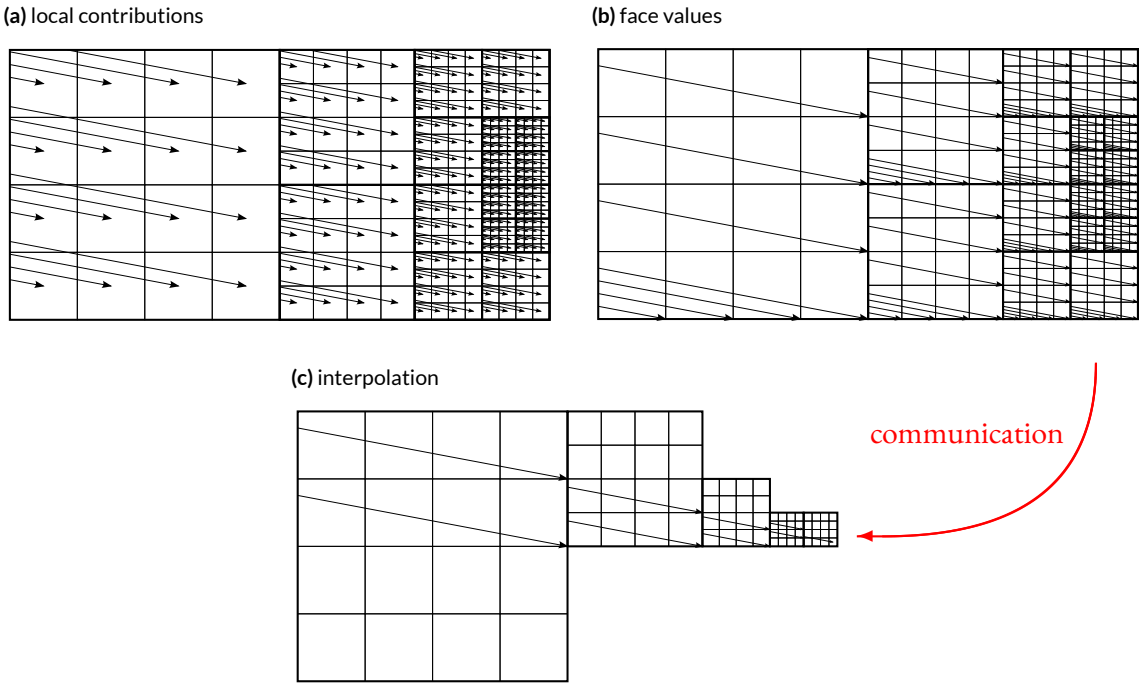

Figure 3.3: The basic steps of the hybrid characteristics method for parallel rays (compare to Rijkhorst et al. (2006)); a) local contributions as calculated with long characteristics. b) the outgoing face values which have to be communicated. c) example for the interpolation of face values for a particular target cell after the communication step.

scribed above. The accuracy of this approximation in a 2D or 3D computation depends crucially on the angular resolution, since it determines whether we actually "hit" each other cell during the angular integration of the mean intensity or not. It is also a question of whether or not this is necessary, since not each cell might have an important radiative contribution to the cell of interest. We might miss some important "hot spots" which have a crucial influence on the cell of interest while wasting computational time on cells which have a negligible contribution. E.g., we avoid this problem partly by calculating the radiation from point sources explicitly for each cell (Section 3.2.1).

However, the Lambda step from Equation 3.12 requires that we know the source function in advance. If we take the temperature from FLASH's hydro solver, we can compute the source function simply as being $S = B(T)$ then solve for the radiation field, couple it back to the hydro solver and we are done. This approach assumes the gas to be in a state of thermodynamical equilibrium but this is, of course, not always the case. If the radiation field is decoupled from the gas temperature, we do not know the source function in advance. The solution then requires some

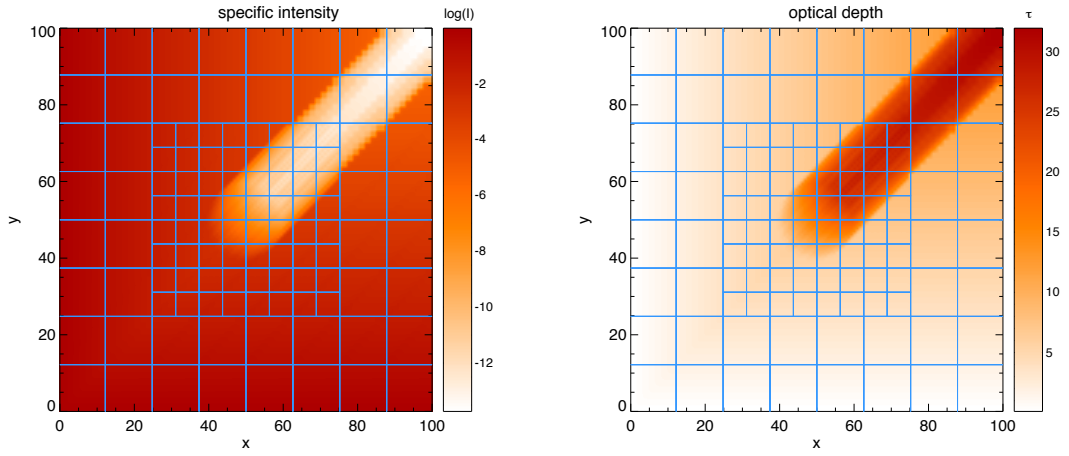

Figure 3.4: The specific intensity and the optical depth computed diagonally in the xy-plane with a central density clump. The source function is set to unity at the left and bottom outermost boundaries and zero everywhere else. The opacity of the central clump is one order of magnitude higher than the ambient opacity. The grid indicates the block structure of the AMR grid, units are arbitrary.

kind of iterative procedure to account for the non-local coupling of the radiation field with the gas. In the theory of radiative transfer, this iterative method is called *Lambda iteration*, which requires iterating over Equation (3.12) until a self-consistent solution for $J(S)$ is found. Strictly speaking, even in the LTE case with $S = B(T)$, we have to iterate to find a temperature that is consistent with the internal energy of the gas since this determines the thermal emission (see our discussion in Section 6.2). However, the Lambda iteration may need several hundreds of iteration steps, which is too costly and ineffective to be employed in a hydrodynamical simulation. One way of resolving this problem, is to partly solve Equation (3.12) analytically by splitting the Lambda operator. These approaches, called *Accelerated Lambda iteration* (ALI), have been investigated and used extensively in the stellar atmosphere community (e.g. Trujillo Bueno and Fabiani Bendicho, 1995). We have implemented the most simple form of ALI, the local lambda operator, to solve radiative transfer problems even in regions of high optical depths and strong decoupling where the classical Lambda iteration usually fails (Appendix A.1).

3.2.4 The Angular Discretization using HEALPix

The choice of the solid angle grid is equivalent to the problem of discretizing the surface of a unit sphere. The method of characteristics requires the solution of the parameterized RTE along a large number of directions $\mathbf{n}$ depending on the anisotropy of the specific intensity $I(\mathbf{x}, \mathbf{n})$. In

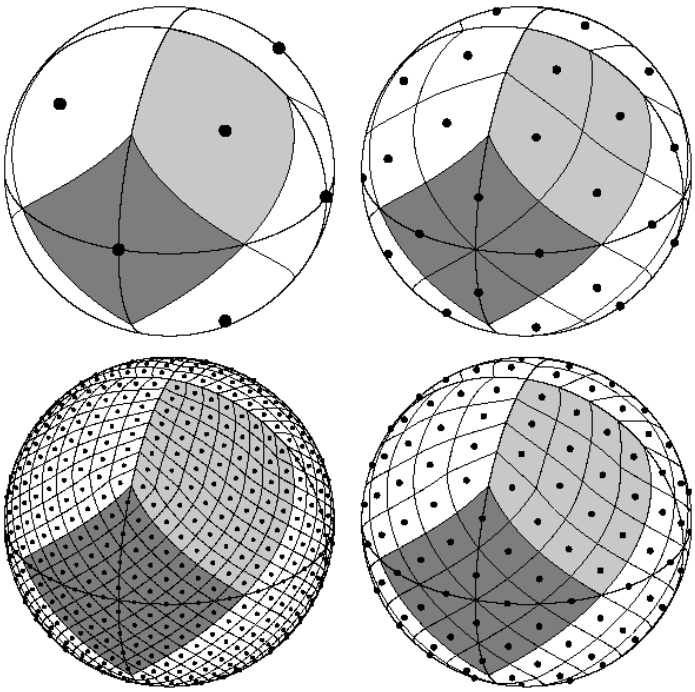

Figure 3.5: The HEALPix tessellation scheme, from Górski et al. (2005). The Area in light grey shows one of the eight (four north, and four south) polar base pixels and the dark grey area shows one of the four equatorial base pixels. Moving clockwise from the upper left panel the base pixels are hierarchically subdivided with the grid resolution parameter equal to $N_{\rm side} = 1, 2, 4, 8$ and the total number of pixels $N_{\rm pix} = 12, 48, 192, 768$.

general, this requires a homogeneous discretization of the solid angle Ω on the 4π unit sphere. For this purpose, we use the HEALPix[1] scheme introduced by Górski et al. (2005). HEALPix ensures an optimal discretization of the unit sphere (also called *pixelation* or *tessellation*) into a number of finite solid angles $\Delta\Omega$. HEALPix in general addresses problems in which a function on domains of spherical topology has to be analyzed. The pixelation scheme was originally developed to handle large datasets generated by cosmic microwave background experiments (e.g., WMAP, Planck) and provides a software library[2] with numerous subroutines for spherical discretization and numerical analysis of functions or datasets on the sphere.

The HEALPix pixelation has a base resolution of 12 pixels in three rings around the poles and the equator of the unit sphere each covering the same area. Based on these base pixels, the resolution is refined by dividing each base pixel into $N_{\rm side}^2$ subpixels, where $N_{\rm side}$ has to be a power of 2 ($N_{\rm side} = 1, 2, 4, 8, ...$). The total number of pixels (assuming an isotropic refinement) is then $N_{\rm pix} = 12N_{\rm side}^2$).

[1] Hierarchical Equal Area isoLatitude Pixelization
[2] http://healpix.jpl.nasa.gov/

3.3 Numerical Hydrodynamics

In this section, we describe the basics of the numerical methods that are used in the FLASH code to solve Euler's equations. These algorithms evolve the conserved variables of hydrodynamics in a fixed frame in contrast to SPH methods which work in the comoving frame of the fluid. The fixed frame approach has the advantage that the evolution of density, momentum and energy can be computed by considering the flux of these quantities through the faces of control volumes. This approach requires a finite volume discretization in space which is very well suited to describe a hyperbolic system of conservation laws, like Euler's equations. The disadvantage lies in the rather static discretization. In a finite volume code, the space is discretized and fluxes are calculated independently of whether the fluid shows dynamic features or not. In an SPH approach, the fluid is evolved by following particles which carry mass, momentum and energy which makes the method naturally adaptive since particles accumulate in very dynamic regions. However, in a finite volume code like FLASH, the spatial discretization has to be treated explicitly by using AMR techniques.

3.3.1 Hyperbolic Equations

The equations of hydrodynamics, we introduced in Section 2.2, are a set of conservation laws that describe the "wave-like" propagation of signals. We recall the governing equations for conservation of mass, momentum and energy here and write down the advection part explicitly for all three dimensions neglecting any source terms:

$$\partial_t \rho + \partial_x(\rho u) + \partial_y(\rho v) + \partial_z(\rho w) = 0, \tag{3.13}$$

$$\partial_t(\rho u) + \partial_x(uu + p) + \partial_y(uv) + \partial_z(uw) = 0, \tag{3.14}$$

$$\partial_t(\rho v) + \partial_x(vu) + \partial_y(vv + p) + \partial_z(vw) = 0, \tag{3.15}$$

$$\partial_t(\rho w) + \partial_x(wu) + \partial_y(wv) + \partial_z(ww + p) = 0, \tag{3.16}$$

$$\partial_t E + \partial_x(u(E + p)) + \partial_y(v(E + p)) + \partial_z(w(E + p)) = 0. \tag{3.17}$$

where E is the total energy volume density ($E = \rho(0.5(u^2 + v^2 + w^2) + e_{\mathrm{int}}$). This system of partial differential equations is closed by the ideal gas equation of state (EOS, Section 2.2.1) which relates the specific internal e_{int} to the pressure

$$p = (\gamma - 1)\rho e_{\mathrm{int}} \tag{3.18}$$

We can rewrite Euler's equation in a very compact form if we define a state vector

$$\mathbf{Q} = \begin{pmatrix} \rho \\ \rho u \\ \rho v \\ \rho w \\ E \end{pmatrix}, \tag{3.19}$$

and flux vectors $\mathbf{F}(\mathbf{Q})$, $\mathbf{G}(\mathbf{Q})$ and $\mathbf{H}(\mathbf{Q})$ for the x-,y- and z-direction respectively

$$\mathbf{F} = \begin{pmatrix} \rho u \\ \rho u^2 + p \\ \rho uv \\ \rho uw \\ u(E+p) \end{pmatrix}, \quad \mathbf{G} = \begin{pmatrix} \rho v \\ \rho uv \\ \rho v^2 + p \\ \rho vw \\ v(E+p) \end{pmatrix}, \quad \mathbf{H} = \begin{pmatrix} \rho w \\ \rho uw \\ \rho vw \\ \rho w^2 + p \\ w(E+p) \end{pmatrix}. \tag{3.20}$$

Equation (3.13)-(3.17) can now be expressed as follows:

$$\partial_t \mathbf{Q} + \partial_x \mathbf{F}(\mathbf{Q}) + \partial_y \mathbf{G}(\mathbf{Q}) + \partial_z \mathbf{H}(\mathbf{Q}) = 0. \tag{3.21}$$

This form is very useful in discussing some basic properties of Euler's equations. First of all, Euler's equation resemble a system of advection equations. The variables in the state vector can only change by a flux across cell interfaces. These kind of conservation laws are called a system of *hyperbolic equations*[1]. Second, the flux vectors are non-linear functions of the state vector. It is therefore, in general, not possible to formulate, e.g., the flux in the x-direction as a product of a state-independent matrix A times the state vector (e.g., $\mathbf{F} = \mathsf{A}\mathbf{Q}$). Instead, all the complexity in the numerical solution arises from the properties of the Jacobian of the flux vectors. In the advection equation for the x-direction

$$\partial_t \mathbf{Q} + \frac{\partial \mathbf{F}}{\partial \mathbf{Q}} \partial_x \mathbf{Q} = 0, \tag{3.22}$$

[1]The formal definition of hyperbolicity is more rigorous and requires the Jacobian to be diagonalizable with real eigenvalues.

the Jacobian ($\frac{\partial \mathbf{F}}{\partial \mathbf{Q}}$) determines the propagation speeds of the conserved variables in the state vector which are tightly coupled. Hence, Euler's equations are just a special case of a system of hyperbolic equations with a non-linear Jacobian.

3.3.2 Riemann Solvers

A central problem concerning the solution of Euler's equations is the solution of the *Riemann problem* which is defined by the 1D initial state

$$\rho, v, p = \begin{cases} \rho_L, v_L, p_L & \text{for } x \leq x_0, t = 0 \\ \rho_R, v_R, p_R & \text{for } x > x_0, t = 0 \end{cases}. \tag{3.23}$$

The initial state represents two identical fluids of different constant states that are separated by a barrier at $x = x_0$. The question at hand is: what happens when the barrier is removed instantly at $t = 0$? This setup resembles the most basic test for any hydrodynamical code and is referred to as a *Sod shock tube test* (Sod, 1978). Figure 3.6 shows the results of such a Riemann problem for a modified version of Sod's problem. What happens is that a *shock* emerges travelling to the right and a *rarefaction wave* travelling to the left. The region where there is a jump in density but neither in velocity nor in pressure is called a *contact discontinuity*. Figure 3.6 compares the solution of the Riemann solver of Roe (Roe, 1981), which we implemented for testing purposes, with the analytic solution computed with the NUMERICA software library [1] described in Toro (2009). Roe's solver is an approximate linearized characteristics Riemann solver that is based on the decomposition of the state-vector Q into its eigen-states which are evolved with their appropriate eigen-velocities to compute the fluxes in Euler's equation (3.22).

3.3.3 Godunov's Scheme

The method of Godunov solves Euler's equations with a conservative scheme. The idea is *not* to compute cell-centered quantities at position x_i at a certain discrete time t_n, but to evolve cell and time averaged quantities. This leads to a discrete volume method in which jumps in the state-vector on cell interfaces at $x_{i+1/2}$ can be regarded as Riemann problems. The solution of the Riemann problem on the cell interfaces leads to a new state-vector for each cell. However, the Riemann solution can lead to quite complex states in the cell since two Riemann solutions from

[1] http://www.ing.unitn.it/ toroe/software.html

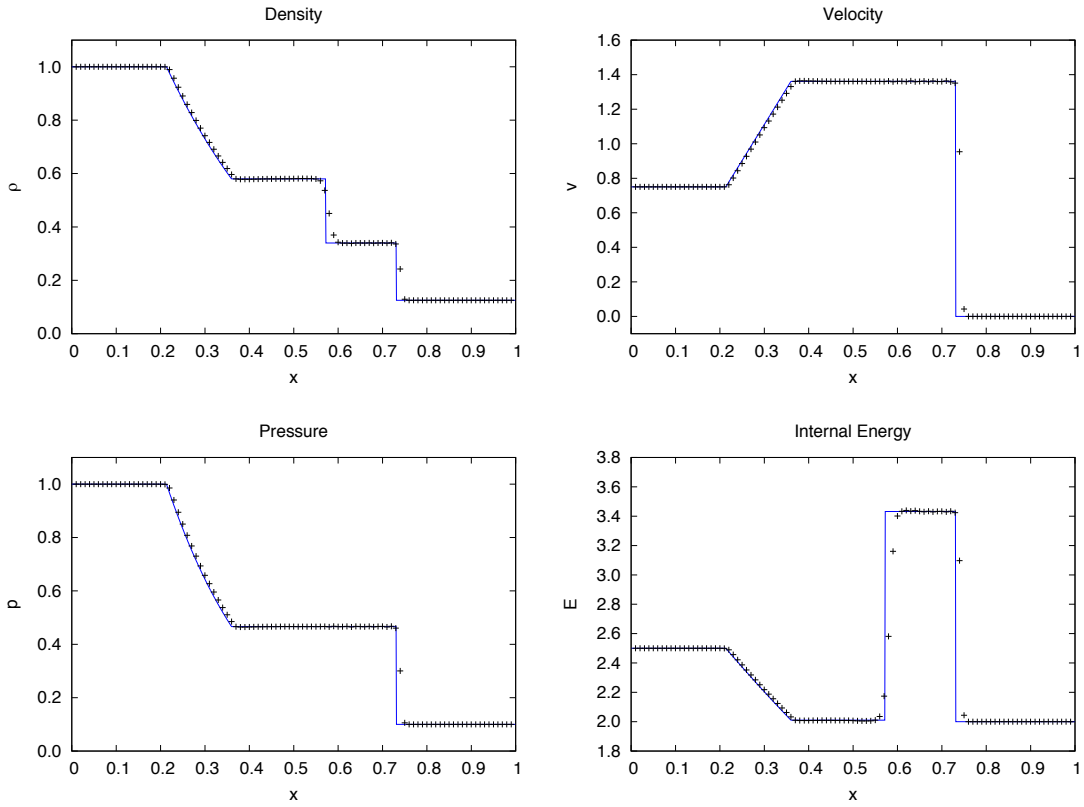

Figure 3.6: The solution of the Sod shocktube test using the Riemann solver of Roe with a superbee flux-limiter and with $\rho_L = 1.0, v_L = 0.75, p_L = 1.0, \rho_R = 0.125, v_R = 0.0, p_R = 0.1$; solid lines: analytic solution; symbols: Roe's solver. Solutions are compared at $t = 0.2$ and $x_0 = 0.3$; units are CGS.

adjacent interfaces appear inside the cell. Instead, it is easier to interpret Godunov's method as a scheme in which a Riemann solver is used to calculate fluxes at cell interfaces that are used in the conservative scheme

$$q_i^{n+1} = q_i^n - \Delta t \frac{f_{i+1/2}^n - f_{i-1/2}^n}{x_{i+1/2} - x_{i-1/2}}, \tag{3.24}$$

to evolve an arbitrary conserved quantity q of the state-vector $\mathbf{Q}$. The main challenge in solving Equation (3.22) then lies in determining the interface fluxes which are coupled non-linearly to the state-vector (Equation (3.20)). Roe's solver (Figure 3.6) is just one possibility which is easy to implement and can be extended to 2nd order accuracy in space with an appropriate flux-limiter. Another method is the family of HLL-solvers proposed by Harten Lax and van Leer in 1983. The decomposition of the state-vector in HLL-solvers is not as rigorously as in Roe's method but uses only two waves (HLL) or three waves (HLLC) to estimate interface fluxes. HLL-solvers more

or less "guess" wave propagation speeds and the decomposition of the state-vector and do not derive them from a linearized approximation of the Jacobian. They are, therefore, more flexible which results in a large number of variations including HLL-solvers for the MHD equations by including magnetic waves.

An important step in Godunov's scheme is the reconstruction of the interface states from cell averaged quantities since Godunov's original method is only accurate to 1st order in space. Linear interpolation usually leads to 2nd order accuracy and requires slope or flux-limiters to prevent over and undershoot problems (Figure 3.6). However, the hydrodynamical solver in the FLASH code uses a quadratic reconstruction based on the method by Colella and Woodward (1984), called PPM-method ("Piecewise Parabolic Method"). In fact, the reconstruction takes place *before* the solution of the Riemann problem, so the PPM-method does explicitly not linearize the Jacobian. This makes the PPM-method very accurate and more efficient than other 2nd order algorithms but takes considerably more effort to implement. Nevertheless, the PPM-method has proven to be well suited to compute smooths flows as well as shocks and contact discontinuities, which is why it is the method of choice in the FLASH code.

Choosing the Time Step

Since the update of the state vector components q_i in Equation (3.24) is done explicitly, one has to take care of the time step size. The problem is that for the non-linear Euler equations, the solution of the Riemann problem on the cell interface is only valid within the size of the finite volume cell. This restricts the time step so that the eigen-states can not propagate into an adjacent cell. Since the propagation speed is determined by the eigenvalues of the Jacobian, the maximum eigenvalue restricts the size of the time step so that

$$\Delta t_{\mathrm{CFL}} = C_{\mathrm{CFL}} \frac{\Delta x}{\lambda_{\max}}, \tag{3.25}$$

where C_{CFL} is the *Courant number* which should obey $0 < C_{\mathrm{CFL}} < 1$. This is known as the *Courant-Friedrichs-Lewy condition* (Courant et al., 1928) (CFL-condition), which states that the domain of dependence, e.g., of q_i^{n+1} at time $t = t_n$, should include the true domain of dependence at $t = t_n$, or in other words: in the limit of $\Delta t_n \to 0$, the discrete solution q_i^n should resemble the exact solution. From this criterion follows the CFL-condition that restricts the time step according to Equation (3.25). Restricting the Courant number to a value less than

unity guarantees that no eigen-signal (or wave) travels further than its domain of dependence, which is the cell size given by Δx. The CFL-condition is a general stability criterion which can easily be extended to include the eigen-signals of, e.g., the MHD equations which are determined by the Alfvén wave speeds.

3.4 FLASH/RT - Coupling the Radiation Solver

The FLASH code (Fryxell et al., 2000) is a versatile MHD computer code and is extensively used for computational science research projects, especially in the field of theoretical astrophysics [1]. In addition to the hydrodynamical and MHD solvers, FLASH contains a variety of physics modules to deal with heating and cooling processes, self-gravity, diffusion and conduction, chemistry, the EOS and many more. The FLASH code works on an Eulerian grid with AMR and domain decomposition (Olson et al., 1999) for high performance, massively parallel computations (see Section 3.2.2). It is parallelized using the Message Passing Interface (MPI) to exchange boundary information between subdomains and shows excellent scaling behaviour on any computational infrastructure (e.g., Fryxell et al., 2000). AMR is especially important in simulations of the star formation process since this requires to resolve a large range of length scales (Section 1.3) which would not be feasible with a homogeneous grid. Since resolving the Jeans length from Equation (1.7) during the collapse simulation is critical to avoid artificial fragmentation (Truelove et al., 1997), this is often an important refinement criterion in these simulations.

For this work, we use a modified version of the FLASH 2.5 release. This version contains a number of additional modules including radiative cooling by atomic and molecular excitations as well as radiative cooling by gas-dust coupling (Banerjee et al., 2004; Banerjee and Pudritz, 2006), heating by ionizing radiation from massive stars (Rijkhorst et al., 2006; Peters et al., 2010) ambipolar diffusion (Duffin and Pudritz, 2008), and sink particles (Federrath et al., 2010). The sink particle technique, first introduced by Bate et al. (1995) for SPH simulations, provides a subgrid model for the Truelove criterion (Truelove et al., 1997). This allows to simulate the collapse of turbulent cloud cores and to study the disc evolution for a self-gravitating system (e.g., Seifried et al., 2011, 2012) without resolving individual protostars. This modified FLASH version was also used to study the effect of ionization feedback from young massive stars in Peters et al. (2010) and Peters et al. (2011), where sink particle were used as point sources in the hybrid characteristics radiation module. Our new radiation solver is included in the modular architecture of the FLASH Code

[1] http://flash.uchicago.edu/site/publications/flash_pubs.shtml

and contains a number of implementations for the source function, opacities, radiative heating and cooling processes, and Lambda iterations. We refer to this version as FLASH/RT.

3.4.1 The Radiation Solver in the FLASH Framework

Since our method is implemented in the FLASH framework, it is straightforward to couple the radiative transfer module to the hydrodynamical and MHD modules of the FLASH code. The coupling is done by accounting for radiative emission and absorption processes, which are determined by the thermal emission opacity $\chi_e = \kappa_e \rho$ and the thermal absorption opacity $\chi_a = \kappa_a \rho$. The opacities are calculated from mass specific cross sections κ_e and κ_a which we have implemented in a separate module of the FLASH framework. Note that the total extinction coefficient χ, which is used for the solution of the RTE, may include an additional scattering opacity χ_s and therefore $\chi = \chi_a + \chi_s$. The coupling of both the radiation and the MHD solver is achieved by computing a source term according to Mihalas and Weibel Mihalas (1984) which describes the total net gain or loss of energy due to radiative heating and cooling. It reads

$$Q_{\mathrm{rad}} = 4\pi \int_0^\infty \chi_\nu (J_\nu - S_\nu) d\nu. \tag{3.26}$$

This source term is computed from the time-independent solution of the radiation field as described in the previous sections and it is coupled to the MHD integrator in an operator splitting step. Hence, the set of compressible MHD equations in dimensionless form including gravita-

tion and radiative energy exchange are those of

continuity

$$\frac{\partial \rho}{\partial t} + \nabla \cdot (\rho \mathbf{v}) = 0, \tag{3.27}$$

momentum conservation

$$\frac{\partial (\rho \mathbf{v})}{\partial t} + \nabla \cdot (\rho \mathbf{v} \otimes \mathbf{v} + p_* 1 - \mathbf{B} \otimes \mathbf{B}) = \rho \mathbf{g} \tag{3.28}$$

energy conservation

$$\frac{\partial E}{\partial t} + \nabla \cdot (\mathbf{v}(E + p_*) - \mathbf{B}(\mathbf{v} \cdot \mathbf{B})) = \rho \mathbf{v} \cdot \mathbf{g} + Q_{\mathrm{rad}}, \tag{3.29}$$

and the induction equation

$$\frac{\partial \mathbf{B}}{\partial t} - \nabla \times (\mathbf{v} \times \mathbf{B}) = 0, \tag{3.30}$$

with the gas velocity field $\mathbf{v}$, the magnetic field vector $\mathbf{B}$ and the gravitational acceleration $\mathbf{g}$. p_* is the total pressure and E the total energy density of a fluid element containing magnetic contributions according to

$$p_* = p + \frac{B^2}{2}, \tag{3.31}$$

$$E = \frac{1}{2} \rho u^2 + e_{\mathrm{int}} \rho + \frac{B^2}{2}. \tag{3.32}$$

with the gas density ρ, the thermal pressure p and the internal specific energy e_{int}. Note that we solve the equations of MHD and radiative transfer successively by an operator splitting step and not simultaneously. Furthermore, for the test cases in Chapter 4, the thermal pressure dominates the hydrodynamics, and it is several orders of magnitude larger than the radiation pressure, which we therefore neglect in the momentum equation (3.28). Figure 3.7 shows our solver in the FLASH framework.

Coupling the Radiation Source Term

The current coupling is done by an update of the internal gas energy e_{int} and temperature T respectively. Since we solve the time-independent RTE, there is no explicit update of the radiative energy or the source function. Instead this is done in the following time step when the gas

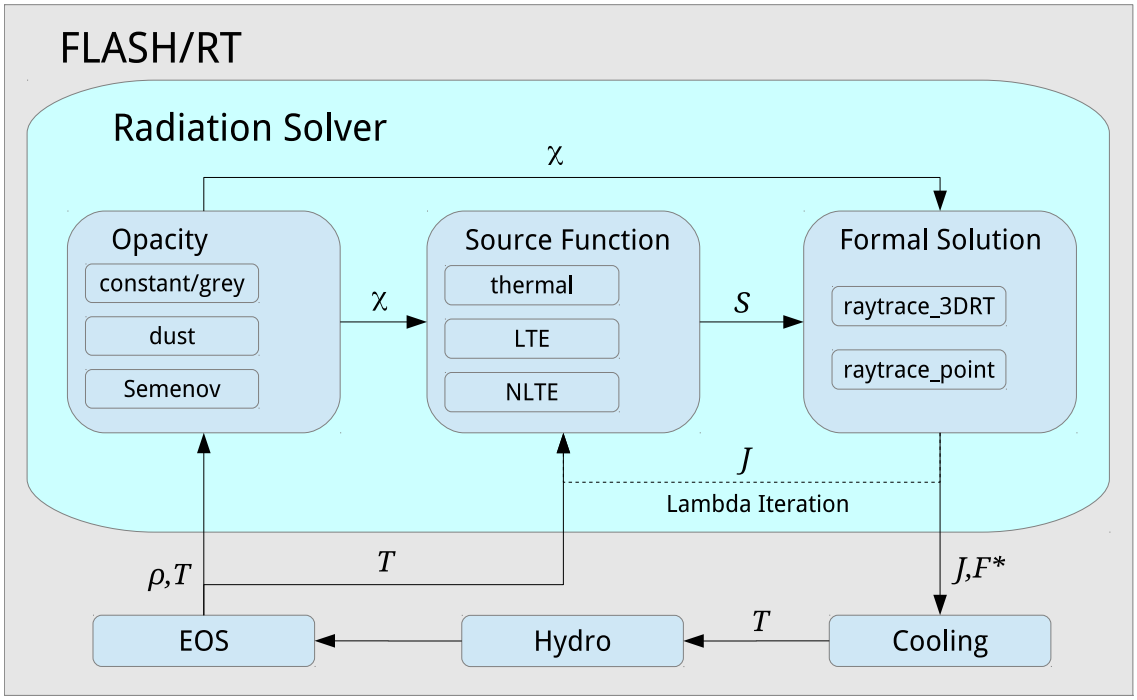

Figure 3.7: The radiation solver in the modular FLASH framework.

quantities have been updated. The update of the internal energy is done explicitly by

$$\Delta e_{\text{int}} = \Delta t \; Q_{\text{rad}}. \tag{3.33}$$

Due to the explicit update, we have to make some restrictions on the time step. The radiation field does not have an explicit influence on the CFL time step in Equation (3.25) since the energy update is done after the solution of the MHD equations. Instead, we compute a cooling time step which is chosen if it is shorter than any other time step from a FLASH module. The cooling time step should be chosen so that the energy contribution Δe_{int} does not exceed a fixed percentage of the internal energy. Otherwise, if the time step Δt is chosen too large, the total radiative energy could become negative (e.g., $\Delta e_r > e$). This leads to the following time step restriction:

$$\Delta t_{\text{c}} = \frac{e_{\text{int}}}{\Delta e_{\text{int}}} \, k_{\text{c}} \, \Delta t_{\text{CFL}}, \tag{3.34}$$

where k_c determines how much change in the internal energy is allowed during a time step. The time step highly depends on the absorption coefficient χ since it determines the optical depth of the medium and how much radiation is absorbed and emitted during a single time step. Typically

the choice of $0.2 > k_c > 0.01$ is convenient as it produces accurate results (Chapter 4) and time steps about one oder of magnitude lower than the CFL time step.

4

Tests

In this chapter, we show test results from the implementation of our radiation solver. The tests include time-independent as well as dynamical tests in 1D and 3D in Section 4.1. We also show results from the combined FLASH/RT code in a series of 1D radiative shock calculations in Section 4.2. Finally, we investigate the performance of our implementation in Section 4.3.

4.1 Testing the Radiation Solver

In this section, we describe tests performed to exclusively examine the accuracy and performance of the radiation solver without coupling it to other modules in FLASH. These tests include time-independent solutions of a static scattering dominated 1D plane-parallel atmosphere, 3D thermal dust continuum radiative transfer in a protostellar disc as well as time-dependent tests.

4.1.1 Non-LTE 1D Atmosphere

In the first test, we compute the radiation field in a grey, isothermal, scattering dominated 1D atmosphere. This test is typically used to verify a radiation solver's iterative performance and

accuracy to describe non-LTE systems on a wide range of optical depths. It is also particularly useful to ensure that the solver accurately reproduces the diffusion limit in an optically thick regime, e.g., in the lower parts of the atmosphere. This test also requires the accelerated lambda iteration (ALI, Appendix A.1) since the classical lambda iteration fails to reproduce the solution in the case of strong scattering contributions.
The amount of scattered radiation is quantified by the ratio of the thermal absorption coefficient to the total extinction coefficient from Equation (2.4):

$$\epsilon = \frac{\chi_a}{\chi_a + \chi_s} \tag{4.1}$$

where we neglected the frequency dependence and ϵ is the *photon destruction probability*. The grey source function in the atmosphere contains a thermal part and a scattering contribution, and it reads

$$S = \frac{\eta}{\chi} = \frac{\eta_s}{\chi_a + \chi_s} + \frac{\eta_e}{\chi_a + \chi_s} \tag{4.2}$$

$$= (1 - \epsilon)J + \epsilon B, \tag{4.3}$$

where we defined $J = \eta_s/\chi_s$ and the thermal emission is $B = \eta_e/\chi_a$. Since the atmosphere is isothermal, we assume that we know the temperature and normalize it so that $B = 1$. The crucial part in this test is to find the source function which has to be consistent with the mean intensity J which is

$$J = \frac{1}{2}(I_- + I_+), \tag{4.4}$$

where I_- and I_+ are the down and upward (2 stream solution) integrated specific intensity respectively (according to Equation (3.8)). Since we assume a uniform mass specific opacity κ and constant temperature T, the intensity is only a function of optical depth $d\tau = \chi dz$, thermal emission B and the photon destruction probability ϵ. The mean intensity is then given by the analytic solution

$$J = B\left(1 - \frac{\exp(-\sqrt{\epsilon}\tau)}{1 + \sqrt{\epsilon}}\right). \tag{4.5}$$

The density ρ of the model increases exponentially with distance from the upper boundary and we assume that $\chi \propto \rho$ but with ϵ being constant. There is no incoming radiation at the upper boundary of the atmosphere at $\tau = 0$ while at the lower boundary the incoming radiation

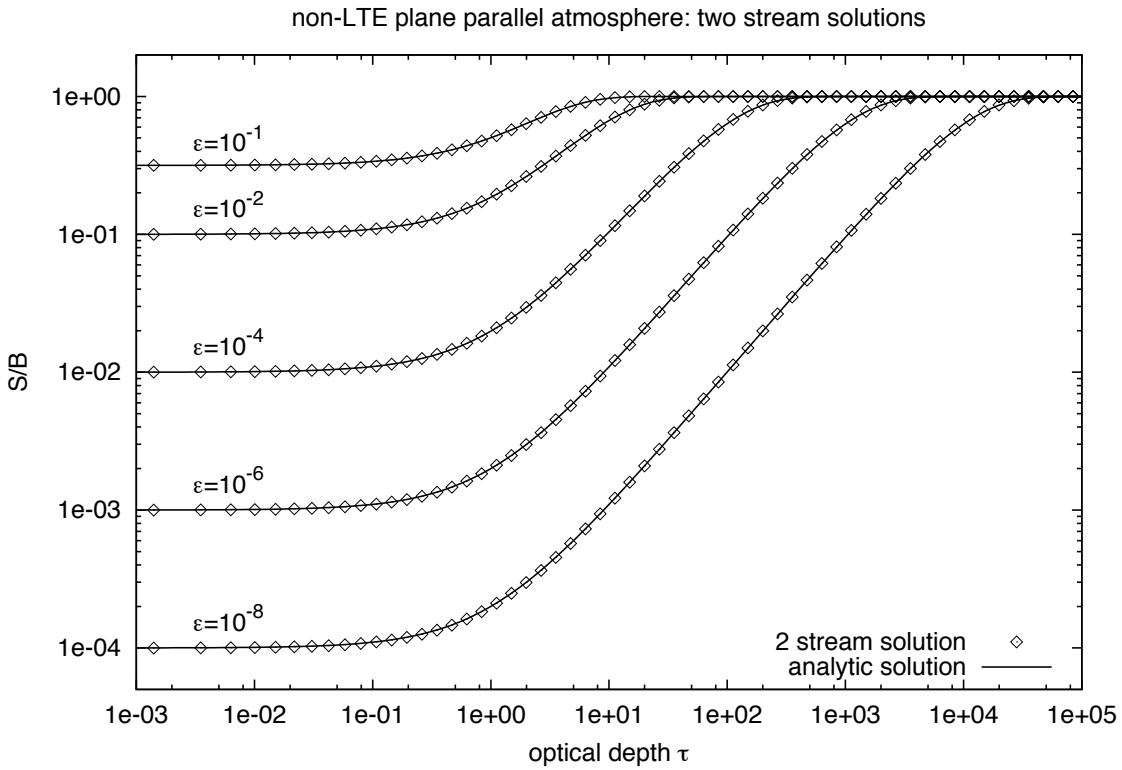

Figure 4.1: Scattering dominated 1D atmosphere problem. The solutions from the radiation solver (symbols) are compared to the analytic solutions (lines) for five different photon destruction probabilities.

is $I = B$. The resulting model atmosphere provides an exponentially varying optical depth τ which resolves the transition region from the optically thick inner LTE-regions to the optically thin NLTE-regions at the outer boundary. We test the solver for a wide range of photon destruction probabilities from $\epsilon = 10^{-1}$ to 10^{-8}. The domain consists of 8 subdomains each containing 8 cells which results in a total spatial resolution of 64 cells. Figure 4.1 shows the results. In the outer optically thin parts of the atmosphere, the scattering contribution in the source function becomes dominant since radiation leaves the atmosphere. The numerical solution is in excellent agreement with the analytic solution.

4.1.2 Hydrostatic Protostellar Disc

Cosmic dust is one of the most important constituents of the ISM. By mass, it makes up only a small fraction of typically about 1%, but dust has important radiative and chemical properties.

Dust particles have strong continuum opacities which are highly frequency-dependent. Especially in the optical regime, dust absorbs light much more efficiently than in the infrared regime. That is why young protostars, which are surrounded by gaseous and dusty envelopes, are difficult to observe in the visible wavelengths but require infrared observations (see also Section 1.3.3). Thermal absorption and reemission of radiation by dust (a process called *reprocession*) strongly determines the thermodynamical properties of a protostellar disc, especially in those regions where the disc is opaque to direct stellar radiation and dominated by thermal reemission of dust molecules. This is mainly the case near the equator of the disc because radial optical depths with respect to the central star are typically much larger than unity ($\tau_* \gg 1$). Therefore, modelling the temperature structure requires diffuse radiative transfer to be taken into account.
In this test setup, we combine emission from a point source with the solution of the radiative transfer equation (RTE). The goal is to determine the self-consistent temperature structure of the gas in a protostellar disc. The setup is based on the benchmark by Pascucci et al. (2004), which is based on the theoretical work by Chiang and Goldreich (1997). We compare our solutions from a 3D calculation with the results from the Monte Carlo radiative transfer code RADMC3D (Dullemond, 2012).

Thermal Radiative Transfer

A protostellar disc combines optically thick and thin regimes, which requires the computation of primary stellar radiation and the thermal reemission from dust molecules in the disc. Our approach follows the idea of splitting the radiation field in two components and handling each component separately. Following the work of Dullemond (2002), the first component we compute is the extinct stellar flux. This can be handled by using the original hybrid characteristics method, which computes the optical depth with respect to a central stellar source (τ_*). The extinct stellar flux F_* at a distance r from a star of luminosity L_* is given by

$$F_*(\mathbf{x}) = \frac{L_*}{4\pi r^2} \exp(-\tau_*(\mathbf{x})), \tag{4.6}$$

assuming that the star can be approximated as a point source. The amount of energy per unit time that is absorbed this way is determined by the absorption coefficient χ and given by

$$Q(\mathbf{x}) = \chi F_*(\mathbf{x}). \tag{4.7}$$

The reemitted radiation of the dust grains in the disc is treated as a secondary component of the radiation field, which we call the *reprocessed* radiation field. This component is computed with the general transfer algorithm using parallel rays. Assuming LTE, the dust grains will acquire an equilibrium temperature such that they emit exactly the same amount of energy which they absorb

$$\frac{\sigma}{\pi}\chi T^4 = \frac{Q}{4\pi} + \chi\frac{1}{4\pi}\oint_{4\pi} I \; d\Omega. \tag{4.8}$$

where I is the specific intensity of the reprocessed radiation field. The first term in Equation (4.8) accounts for the direct stellar radiation while the second term describes the energy of the reprocessed radiation field. The transfer equation for reemitted radiation by dust grains is

$$\frac{\partial I}{\partial \tau} = \frac{\sigma}{\pi}T^4 - I. \tag{4.9}$$

Hence, the source function in this setup is the frequency-integrated thermal emission from dust grains $S = \frac{\sigma_{\mathrm{SB}}}{\pi}T^4$. The task at hand is to find a temperature that is consistent with the coupled set of Equations (4.8) and (4.9). This is done by iterating the equations until convergence is reached (Lambda-iteration).

The Disc Model

For the simulation setup we are following the benchmark test of Pascucci et al. (2004) which resembles a *flared disc* (Chiang and Goldreich, 1997). The idea is to define a radial gas surface density distribution and to assume that the vertical density structure is only determined by the hydrostatic equilibrium in the vertical direction. The gas density distribution is given by

$$\begin{aligned}
\rho(r,z) &= \rho_0 \; f_1(r) \; f_2(r), \\
f_1(r) &= \left(\frac{r}{r_d}\right)^{-1.0}, \\
f_2(r) &= \exp\left(-\frac{\pi}{4}\left(\frac{z}{h(r)}\right)^2\right), \\
h(r) &= z_d\left(\frac{r}{r_d}\right)^{1.125},
\end{aligned} \tag{4.10}$$

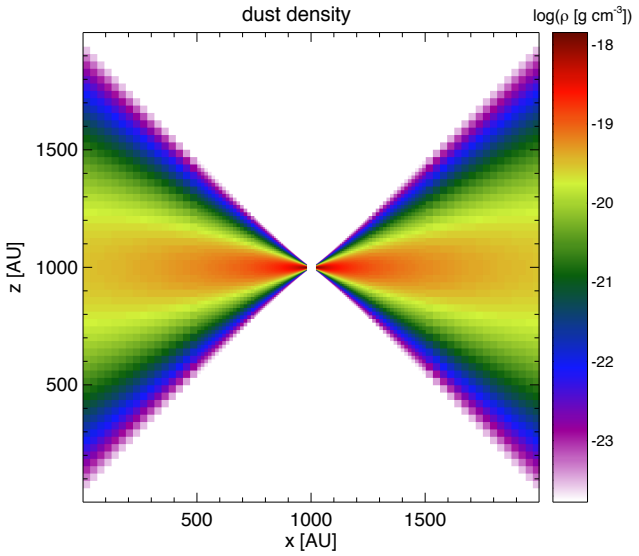

Figure 4.2: The dust density in the xz-midplane for the Pascucci benchmark for a total optical depth of $\tau_{\rm disc} = 1$.

where r is the radial distance in the disc midplane, z is the height above the disc, and ρ_0 is the gas density in the midplane at $r = r_d = 500\text{AU}$ and $z = 0$. The outer disc radius is defined by $r_{\rm out} = 1000\,\text{AU} = 2\,\text{r}_\text{d}$ and we crop the disc at an inner radius $r = r_{\rm in}$. z_d determines the height of the disc which we choose to be $0.25\ r_d$ consistent with Pascucci et al. (2004). We choose the central source to have solar properties with $M_* = 1\,\text{M}_\odot$, $\text{R}_* = 1\,\text{R}_\odot$ and $T_* = 5800\,\text{K}$. We use a grey opacity at the visible wavelength of $\lambda = 550$ nm from the opacity tables used in Pascucci et al. (2004) ($\kappa = 8736\,\text{cm}^2\,\text{g}^{-1}$).

In contrast to the Pascucci benchmark, we perform our calculations in 3D instead of 2D. Therefore, we can not directly compare our results to the Pascucci results but instead use the results from RADMC3D as a reference. We perform calculations for three cases of ρ_0 so that the total radial optical depth of the disc in the midplane varies from $\tau_{\rm disc} = 1$, $\tau_{\rm disc} = 10$ and $\tau_{\rm disc} = 100$. We do not explicitly distinguish between a gas and a dust temperature and assume both to be tightly coupled and the dust density is defined as a fixed fraction of the gas density (1%). The dust density distribution through the xz-midplane of the disc setup for the optically thin case ($\tau_{\rm disc} = 1$) is shown in Figure 4.2.

The spatial resolution varies over 4 refinement levels from $\Delta x = 31.25\,\text{AU}$ in the outer regions to $\Delta x = 1.953\,\text{AU}$ in the center of the disc. The solid angle integration is performed using 768 directions (nSide=8).

Results

The resulting temperature structures and averaged midplane profiles are shown in Figure 4.3. As it turns out, the accuracy of the solution is very sensible to the spatial resolution of the inner edge of the disc at $r = r_{\rm in}$ which is a result of discretizing the inner circular rim on a Cartesian grid. Therefore, we increase the inner radius from $r_{\rm in} = 10\,\mathrm{AU}, 20\,\mathrm{AU}$ to $40\,\mathrm{AU}$ for the three different setups to guarantee sufficient resolution at the point where the disc becomes optically thick. In the optically thin case ($\tau_{\rm disc} = 1$), the midplane temperature is almost entirely dominated by the direct illumination of the central source. In the optically thick cases, the midplane temperature is dominated by the reprocessed radiation from dust in the photosphere of the disc, which is directly illuminated by the central source. At the point where the disc becomes optically thick, a bump emerges in the temperature profile since the dust distribution becomes dense enough to absorb a considerable amount of radiation from the central source. Our results are in excellent agreement with the reference computed by RADMC3D and within the 10% range of the results from the different codes used for the Pascucci et al. (2004) benchmark.

4.1.3 Time-Dependent Radiative Transfer

In this section, we show results from time-dependent radiative transfer calculations. In order to couple the radiative transfer solver to the FLASH code, we have to calculate the energy contribution by the radiation field. Solving the time-dependent RTE on the timescale of the speed of light would lead to time steps far too small for the use in a hydrodynamical simulation on astrophysical scales. However, since we are not interested in the dynamics of the propagation of the radiation itself but, instead, in its contribution to the energy budget of the gas, we assume the hydrodynamical timescale to be much larger than the timescale on which radiation is transported. This means that the radiation field emerges instantaneously everywhere, and we assume the solution of the time-independent RTE as being convenient (see also Section 3.4.1).

Diffusion Setup

In this test, we investigate the ability of our solver to follow the flux of radiative energy into a highly opaque medium. In this case, the propagation of the radiation field can be described by

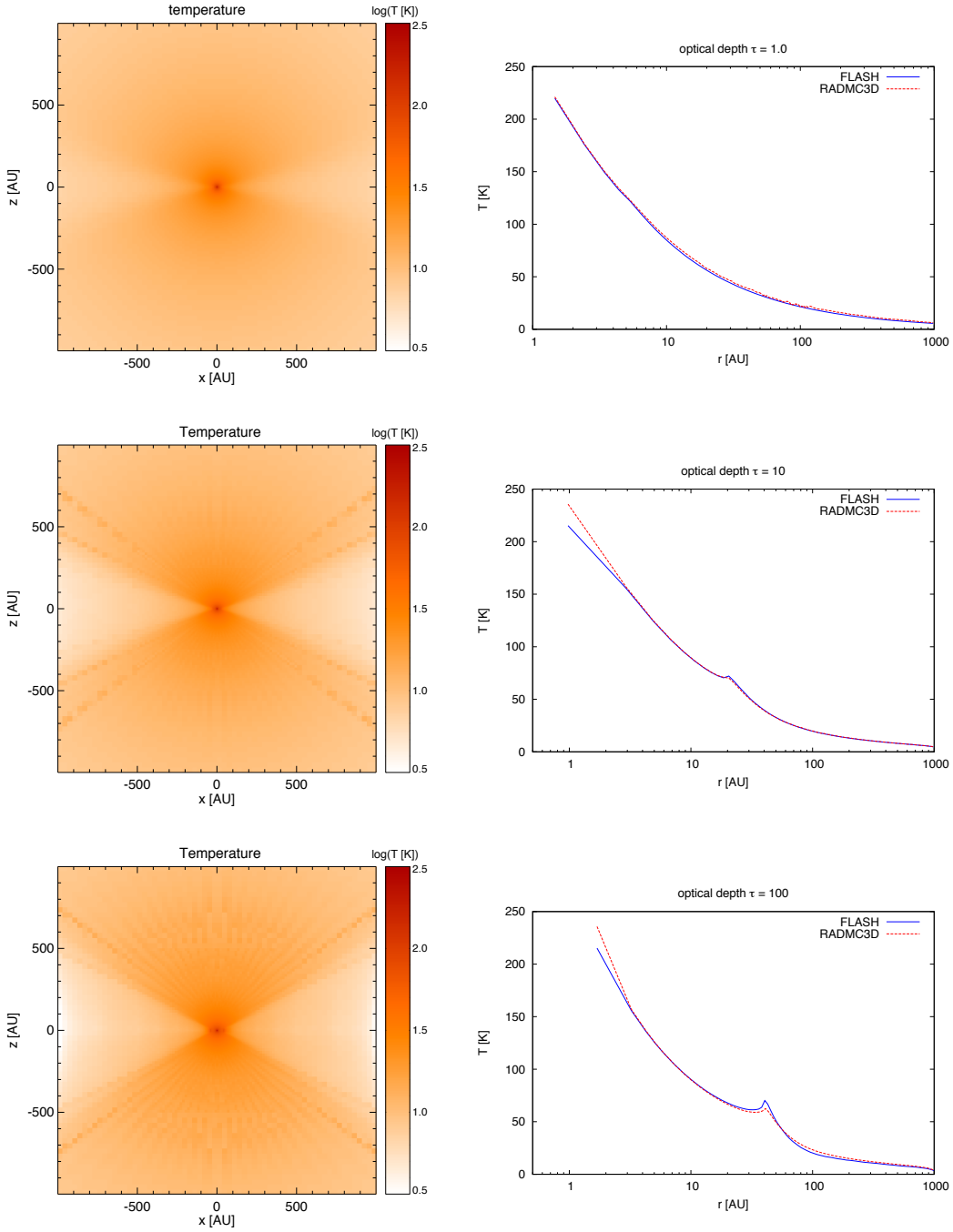

Figure 4.3: The solutions of the Pascucci et al. (2004) benchmark problem. Left column: the temperature structure through the xz-midplane of the disc for total radial optical depths of $\tau = 1$ (top), $\tau = 10$ (mid), and $\tau = 100$ (bottom). Right column: averaged temperature profiles in the xy-midplane in comparison with the solutions of RADMC3D. Solutions obtained with FLASH/RT use 768 directions for the angular discretization. Monte Carlo computations with RADMC3D were performed using 10^8 photon packages.

the diffusion approximation, and we show that our approach reproduces the diffusion limit accurately. The diffusion approximation is derived from the moment equations of the RTE by invoking a closure relation between the radiative energy and the radiative pressure (e.g., the Eddington approximation). The radiation equations themselves then form a hyperbolic system. By neglecting the explicit time dependence of the radiative flux $\mathbf{F}$ and assuming that $\mathbf{F} \propto \nabla E_r$, the flux can be eliminated from the equations. The dynamics of the radiation field $J = cE_r/(4\pi)$ can then be described in a single equation, the diffusion equation (Mihalas and Weibel Mihalas, 1984):

$$\frac{\partial J}{\partial t} - \nabla \left(\frac{c}{n\,\chi} \nabla J \right) = c\,\chi\,(S - J). \tag{4.11}$$

where n denotes the number of dimension. We do not allow any interaction of the radiation field with the hydrodynamics and only follow the propagation of the radiation field. Hence, the diffusion equation becomes homogeneous since $S = J$. In this case, the solution to the diffusion equation is described by the Gaussian function

$$J_D(\mathbf{x}, t) = \frac{J_0}{(4\pi D t)^{n/2}} \exp\left(-\frac{\mathbf{x} - \mathbf{x}_0}{4Dt} \right), \tag{4.12}$$

where J_0 denotes the initial mean intensity at $t = t_0$ and $\mathbf{x}_0$ its initial position. We use Equation (4.12) to compute the initial conditions $J(\mathbf{x}, t_0)$ for our test setup. We perform 1D and 3D computations with the initial conditions $J_0 = J(\mathbf{x}_0, t_0) = 10^5\,\mathrm{erg\,s^{-1}\,cm^{-2}\,sr^{-1}}$ with $t_0 = 10^{-11}\,\mathrm{s}$ in 3D and $t_0 = 10^{-10}\,\mathrm{s}$ in 1D respectively, The center of the Gaussian is at $\mathbf{x}_0 = 0$, and we evolve the radiation field until $t = 20 \times t_0$ is reached. The length of the computational domain is $1\,\mathrm{cm}$ with a homogeneous density distribution of $\rho = 1\,\mathrm{g\,cm^{-1}}$ and a constant absorption coefficient $\kappa = 1000\,\mathrm{cm^2\,g^{-1}}$, which results in a highly optically thick medium. The temperature is constant and arbitrarily set to $T = 1K$. Since no heating or cooling is allowed, there is no hydrodynamical response from the medium and all hydrodynamical quantities are constant in space and time.

Since we solve the time-independent RTE, there is a problem in reproducing the time-dependent term in Equation (4.11). Strictly speaking, the static source function vanishes since we do not couple the radiation field to the medium through which it propagates. Consequently, the mean intensity would also vanish in the time-independent solution. However, the time dependence causes an implicit effective contribution in the source function (e.g. Jack et al., 2012, and also our discussion in Section 6.1) which depends on the specific intensities of the previous time step. It

is this implicit contribution that is evolved through time and describes the evolution of the radiation field. Since we do not account for this implicit contribution, we solve the problem by operator splitting using the right-hand side of Equation (4.11) to calculate the new source function at the following time step. The evolution is done using a simple forward Euler time integration scheme of the form

$$S_n = S_{n-1} + \Delta t_n \, \chi \, c \, (J(t_{n-1}) - S_{n-1}), \tag{4.13}$$

where Δt_n is the length of the current time step n. Therefore the time step is restricted to be (Section 3.4.1)

$$\Delta t_n = k_{\mathrm{rad}} \Delta t_{n-1} \frac{S^i_{n-1}}{\max(|S^i_{n-1} - S^i_{n-2}|)}, \tag{4.14}$$

where $\max(|S^i_{n-1} - S^i_{n-2}|)$ denotes the maximum change in the source function of all discrete grid points i. k_{rad} limits the maximum change in the source function, and we found a value of $k_{\mathrm{rad}} \approx 0.1$ to give stable and accurate results in 3D.

Results

The results of the 1D solutions are shown in Figure 4.4. We compare the numerical results with the analytic solution given by Equation (4.12) and found our results to be within 1% accuracy at a resolution larger than 32 cells. At the edge of the domain, the numerical solution deviates from the diffusion solution as radiative energy can leave the domain and we allow no irradiation from the outside. The results from the 3D computation are shown in Figure 4.5 and compared to the diffusion solution along the three main axes of the domain. In the 3D case, the domain is subdivided by the AMR grid into 4 blocks in each dimension. Each block contains 8^3 cells giving a total linear resolution of 32 cells. In the 3D case, the setup consists of a Gaussian kernel around the origin which diffuses outwards. The solutions along each coordinate axis are obviously indistinguishable, emphasizing the accuracy and importance of the homogeneous angular HEALPix tessellation. The 3D computations were performed using 192 directions.

4.2 FLASH/RT - Testing the Radiation Hydrodynamics Solver

For the following tests, we use the full FLASH/RT Code including coupling through radiative energy exchange. The tests include a series of 1D radiative shock calculations. Further full 3D

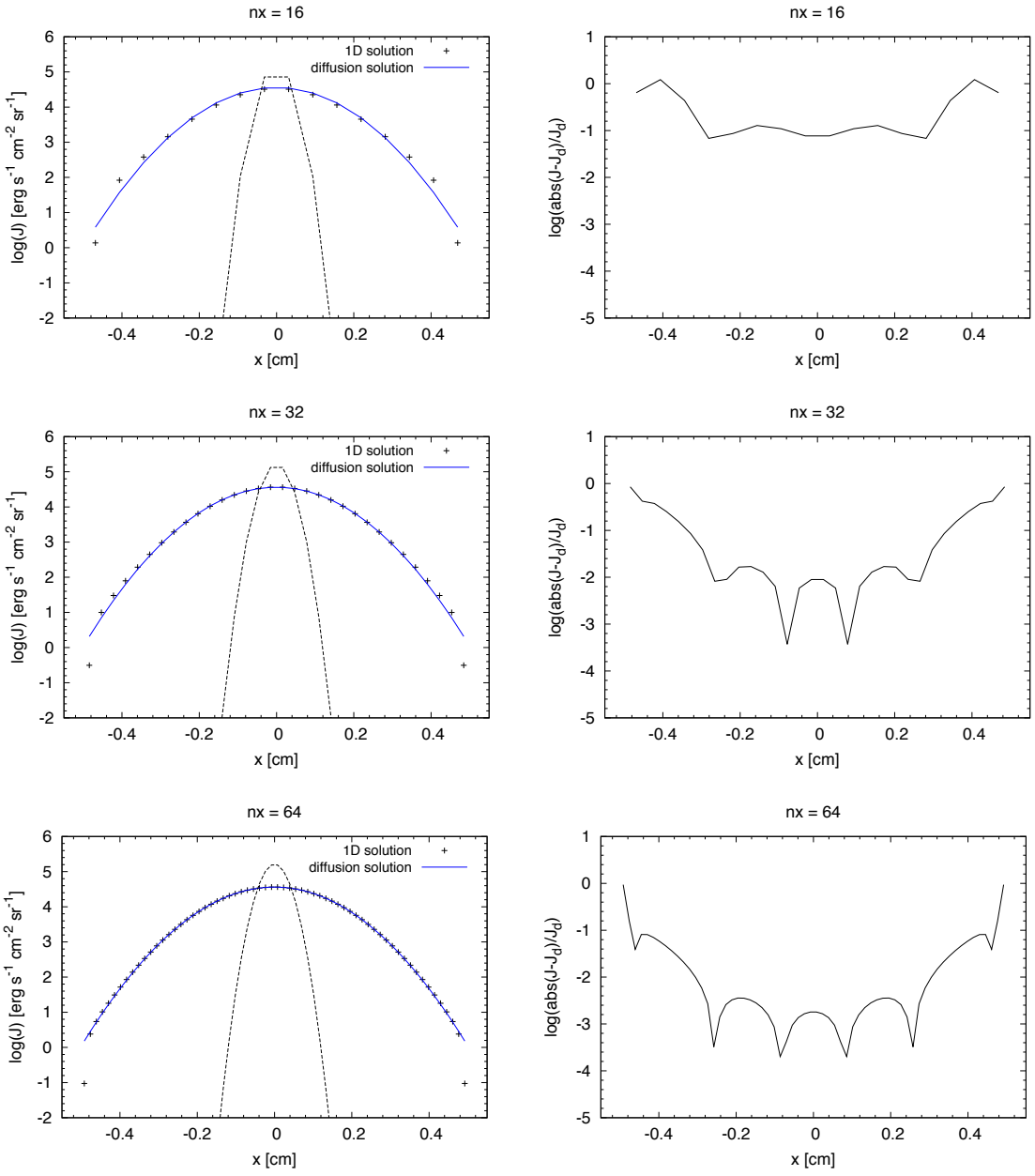

Figure 4.4: Results of the 1D diffusion test for different homogeneous spatial resolutions, *top:* nx=16, *Mid:* nx=32, *bottom:* nx=64. The dashed lines show the initial conditions at $t = t_0$ determined by the Gaussian solution of the diffusion equation. The initial radiative energy (symbols) is evolved and diffuses outwards until $t = 20 \times t_0$ is reached and compared to the analytical solution (solid lines) of the homogeneous diffusion equation. For a sufficient spatial resolution, the numerical solution stays within 1% accuracy. At the edge of the domain, the radiation solver deviates from the diffusion solution as radiation leaves the domain while the diffusion solution is valid for an infinite domain.

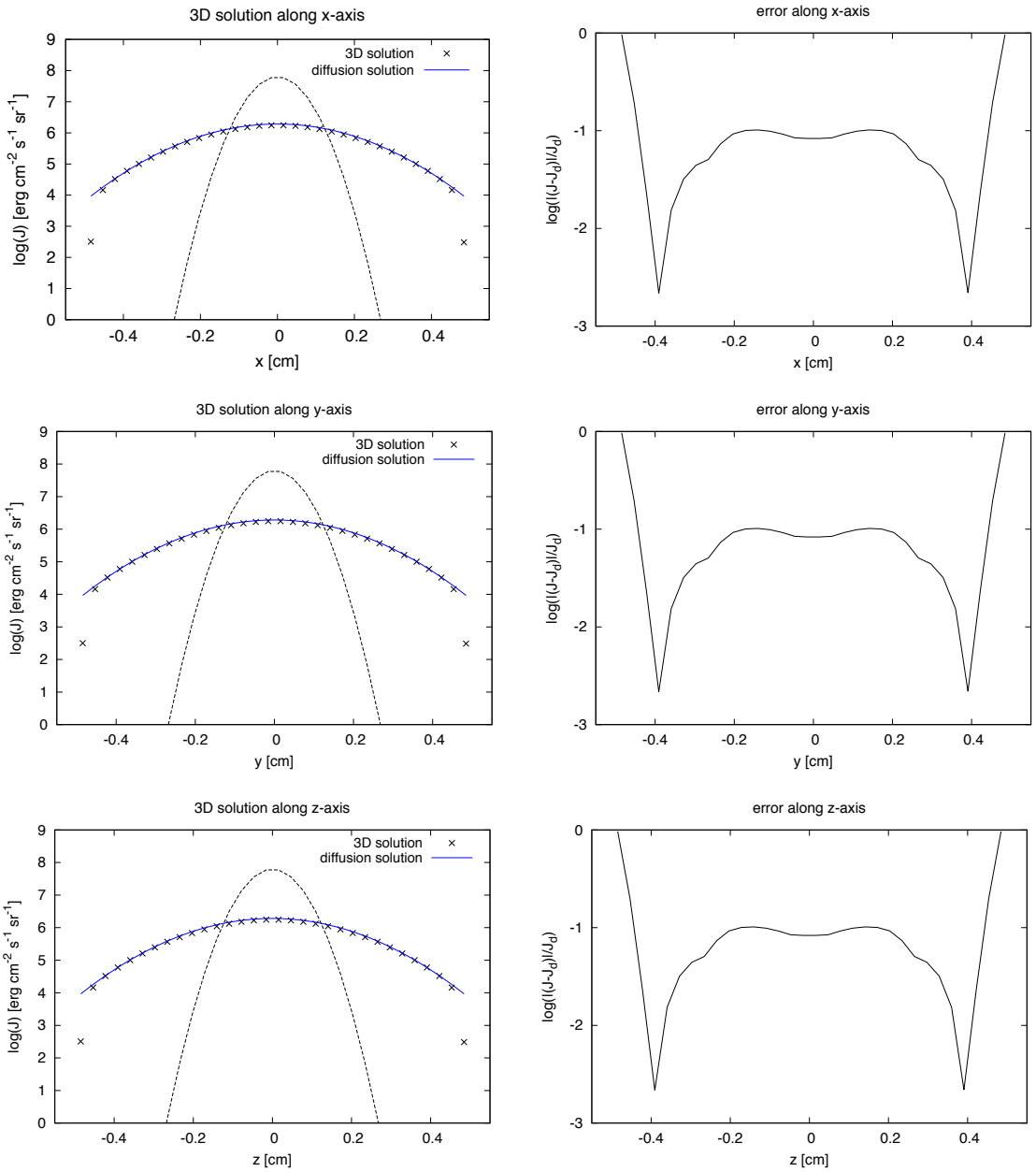

Figure 4.5: Results of the 3D diffusion test along the x-, y- and z-axis of the simulation box with a homogeneous spatial resolution of nx=ny=nz=32 (symbols). The dashed lines show the initial conditions at $t = t_0$ determined by the Gaussian solution of the diffusion equation. The 3D solution is not as accurate as the 1D results but still within 10% of the analytical solution. The obvious independence of the solution on the direction axis a result from the homogeneous angular HEALPix tessellation. The calculations were performed using 192 directions.

radiation hydrodynamical simulation results can be found in the following Chapter 5, which deals with collapse simulations of a molecular cloud core.

4.2.1 1D Non-equilibrium Radiative Shock

Testing the radiative transfer solver for radiative shock computations is the first crucial step in testing FLASH/RT. This test requires us to couple the radiation code to the hydrodynamical solver in FLASH. This is done by a source term, which is determined by the energy budget of absorption and emission processes. We recall the frequency-integrated source term from Equation (3.26) here:

$$Q_{\mathrm{rad}} = 4\pi\chi_a(J - B), \tag{4.15}$$

which is coupled to the hydrodynamical solver by adding it to the right-hand side of the Euler equation for the internal gas energy. For this test case, the emission and absorption opacities are equal. Since the shock setup is used for test purposes, we neglect the magnetic field.

Initial Conditions

The initial conditions are consistent with the theoretical work of Lowrie and Edwards (2008). In their work, the jump conditions and the equations of radiation hydrodynamics are given in a dimensionless form. The equations are normalized using reference material quantities and a constant P_0 which arises from the normalization process and is given by

$$\mathrm{P}_0 = \frac{\tilde{\alpha}_{\mathrm{r}}\tilde{\mathrm{T}}_0^4}{\tilde{\rho}_0\tilde{\mathrm{a}}_0^2}. \tag{4.16}$$

The quantities denoted with a tilde are the dimensional reference material attributes (temperature $\tilde{T}_0$, density $\tilde{\rho}_0$, sound speed $\tilde{a}_0$) and $\tilde{\alpha}_r$ is the radiation constant. The "0"-subscript indicates pre-shock state initial values. P_0 gives a measure for the relative importance of gas and radiation pressure or alternatively, the radiative energy to the material energy (Mihalas and Weibel Mihalas, 1984). For our test setups, we choose a grey non-equilibrium shock setup with Mach numbers of $M_0 = 1.2$, $M_0 = 2$ (subcritical), $M_0 = 3$ (critical), and $M_0 = 5$ (supercritical), which we compute in the reference frame of the shock with $\mathrm{P}_0 = 10^{-4}$ and $\gamma = 5/3$. Lowrie and Edwards (2008) give a dimensionless absorption and transmission cross section, which determine the radiative energy exchange and diffusivity of the radiating materials. Evaluating the dimen-

sionless values of their example setup gives an absorption coefficient of $\kappa_a \approx 423.0\ \mathrm{cm}^2/\mathrm{g}$ and a total extinction coefficient of $\chi \approx 788.0\ \mathrm{cm}^2/\mathrm{g}$, which results in an effective photon destruction probability of $\epsilon = \kappa_a/\chi \approx 0.5377$. The initial dimensionless pre-shock gas temperature T_0 and density ρ_0 are set to unity, the post-shock initial values (T_1, ρ_1) are computed using the Rankine-Hugoniot jump conditions. The actual dimensional initial conditions can then be calculated using their dimensional reference material values (for more details we refer to Lowrie and Edwards (2008)). Finally, the radiation temperature

$$T_\mathrm{r} = \left(\frac{\pi}{\sigma_\mathrm{SB}}\, J\right)^{1/4} \tag{4.17}$$

is initially in equilibrium with the gas temperature. For the radiation shock test problem, the source function is determined by a thermal emission and a diffusive part. In fact, this is equivalent to using the isotropic scattering source function

$$S = (1-\epsilon)J + \epsilon B \tag{4.18}$$

with the appropriate photon destruction probability and a thermal energy contribution given by the frequency integrated Planck emission $B = \frac{\sigma_\mathrm{SB}}{\pi}\tilde{T}^4$. Since the radiation field will not be not be in thermal equilibrium with the material throughout the simulation, we need to iterative until a consistent solution of the mean intensity J is found. However, since $\epsilon \approx 0.5377$ gives only a moderate scattering contribution and using the solution from the previous time step, the accelerated lambda iteration usually converges after 2 or 3 iteration steps.

Results

The shocks need a few nanoseconds to relax into a static equilibrium state. Figure 4.6, 4.7, 4.8 4.9 show the resulting temperature and density profiles after 10 nanoseconds. Sufficiently far upstream (left) and downstream (right) of the hydrodynamical shock (at $x = 0$), gas and radiation are in thermodynamic equilibrium and the radiation temperatures coincides with the gas temperature computed from the initial conditions. Since the total extinction coefficient χ is about twice the thermal absorption and emission coefficient, the temperature of the radiation field and the gas are out of equilibrium near the shock front.
The subcritical shock with $M_0 = 1.2$ (Figure 4.6) shows a hydro shock but no spike in the radiation temperature. For $M_0 = 2$ the so called *Zel'Dovich spike* in the gas temperature appears for

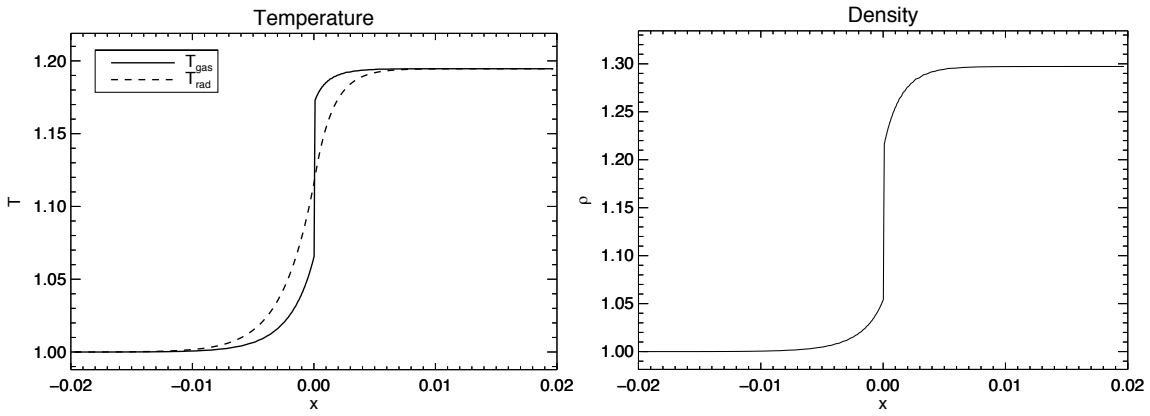

Figure 4.6: Temperature and density profiles for the subcritical shock with $M_0 = 1.2$ in the equilibrium state after 10 nanoseconds. The gas is preheated on the upstream side and cooled on the downstream side of the hydro shock front. Quantities are nondimensionalized.

the first time as seen in Figure 4.7. The spike appears since radiation is transported through the hydrodynamical shock from the downstream to the upstream region and heats up the inflowing gas, which is initially in a thermal equilibrium with the radiation field in the upstream region. After the gas has passed the hydrodynamical shock, it cools down until the radiation field and the gas are again in thermal equilibrium on the downstream side of the shock. Since the upstream temperature at the shock front is still less than the downstream temperature the shock is still subcritical. Figure 4.8 shows the solution for $M_0 = 3$. In this case the shock becomes critical since the inflowing gas is heated up until it almost reaches the value of the downstream temperature and the spike becomes more narrow. Finally, for $M_0 = 5$, the shock becomes supercritical, and the discontinuity in the gas temperature is restricted to the narrow range of the Zel'dovich spike (Figure 4.9). Our solutions resemble the semi-analytical results from Lowrie and Edwards (2008) and show the correct spike evolution. However, a closer look at the results show a slight deviation of the shock front from its initial position (at $x = 0$). Especially in the supercritical case, the shock front drifts very slowly into the downstream direction. This drift is due to the absence of the radiation pressure in our approach, which becomes important for higher Mach numbers (with a higher downstream gas temperature). While the shock front drifts very slowly, the temperature and density profiles do not change since the radiation source term is still very well approximated in our approach.

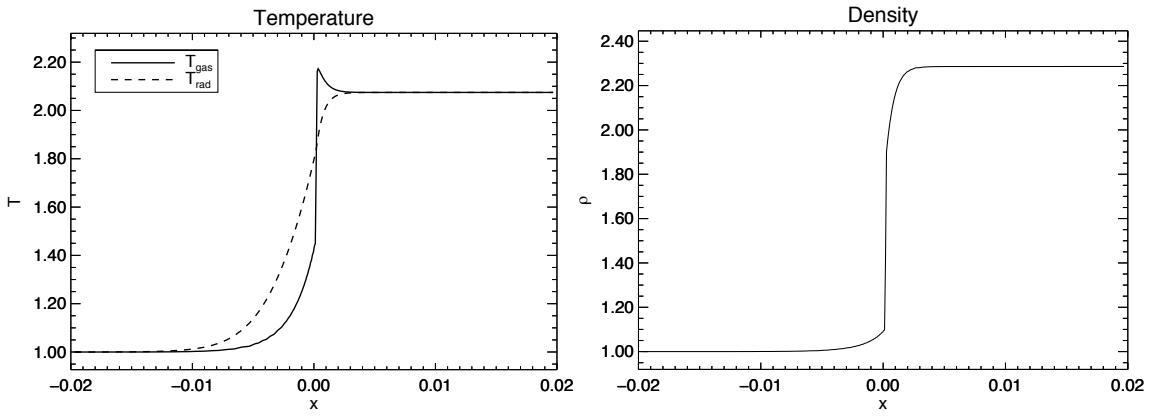

Figure 4.7: Same conditions as in Figure 4.6 but with $M_0 = 2$. The maximum temperature at the shock begins to exceed the downstream equilibrium temperature which results in the Zel'dovich spike. Since the temperature at the upstream side of the shock is still well below the downstream temperature, the shock is subcritical.

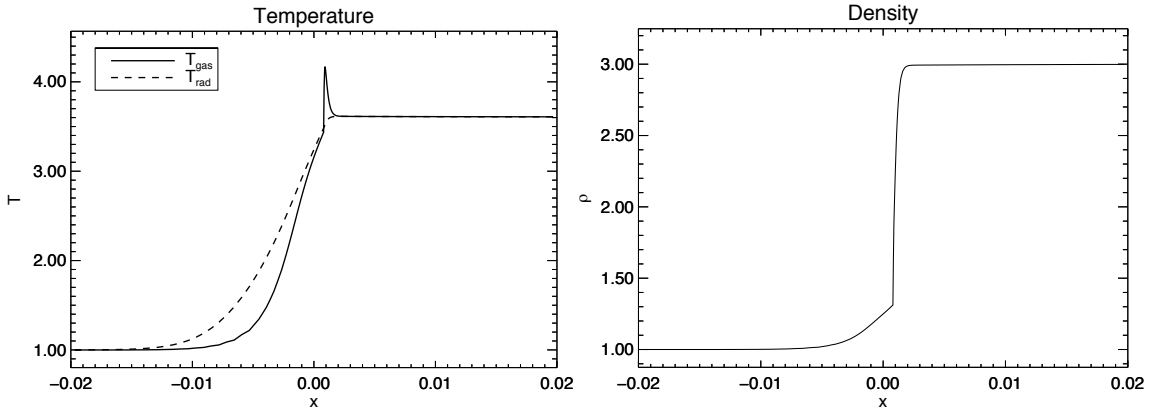

Figure 4.8: Same conditions as in Figure 4.6 but with $M_0 = 3$. The temperature on the upstream side of the hydro shock front almost reaches the downstream equilibrium value. The Zel'dovich spike gets more narrow and the shock becomes critical.

4.3 Performance

The FLASH code shows excellent scaling behaviour on any computational infrastructure (e.g. Fryxell et al., 2000). For this work, the computations are clearly dominated by the solution of the RTE. Hence, the scaling behaviour of the radiative transfer solver is crucial for the total performance of the FLASH/RT calculations. We investigate the scaling performance of our radiation code using the disc benchmark setup (see Section 4.1.2). We performed 50 formal solutions of the RTE using 192 directions on a spatial range covering 5 refinement levels. After the initial refinement, depending on the density structure and the radius, the computational domain consists of 3648 valid subdomains (leaf blocks) each containing 8^3 cells. The FLASH code distributes the

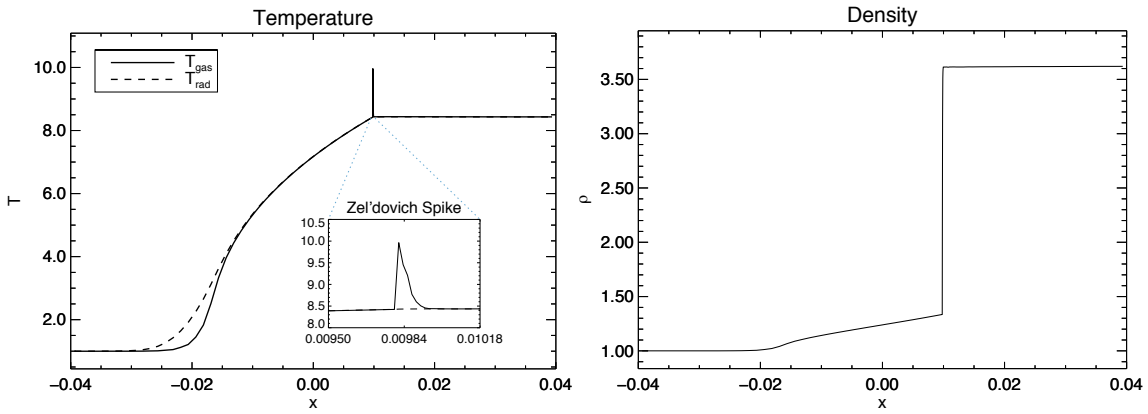

Figure 4.9: Same conditions as in Figure 4.6 but with $M_0 = 5$. The temperature on the upstream side of the hydro shock front reaches the downstream equilibrium value. The Zel'dovich spike gets very narrow and the shock becomes supercritical.

blocks among all available MPI ranks using a Morton space-filling curve[1]. The scaling tests were run at The North-German Supercomputing Alliance in Berlin on the Cray XC30 "Gottfried" using 12-core Xeon IvyBridge processors. Figure 4.10 and Table 4.1 show the scaling results for the computation of the formal solution of the RTE averaged over 50 cycles. The scaling is normalized to the wallclock time using 96 cores (e.g, 8 Xeon IvyBridge processors). "Gottfried" provides 2 Xeon processors with 24 cores in total per computing node, hence, adding 24 cores to the computation will increase the communication overhead. Figure 4.10b shows the speedup compared to a perfect scaling behaviour. The radiation solver scales reasonably well considering the massive communication of non-local information, which is necessary for the solution of the RTE. Figure 4.10c shows that doubling the number of cores decreases the performance per block by approximately 10%, which we consider also as reasonable.

The cost of the radiative transfer solver from a 3D collapse simulation (see the following Chapter 5 and Figure 4.10d) is comparable to the cost for the computation of the self-gravitational potential which is done by a Poisson tree-solver. However, the radiative transfer solver in this particular simulation uses a rather moderate angular resolution of 192 directions (using the HEALPix tessellation from Górski et al. (2005)). For runs including rotation and turbulence, the angular resolution probably needs a much higher resolution of at least 768 directions or higher. Since the cost of the radiative transfer solver scales linearly with the number of directions, it dominates the entire simulation run compared to the calculation of self-gravity. So far, we have tested the FLASH/RT code on our own computing cluster in Hamburg (32 nodes with 2x Intel Xeon Hexa-Core CPUs,

[1] http://flash.uchicago.edu/site/flashcode/user_support/flash4_ug/

nr. of cores	Time [s]	Speedup	Blocks per cpu	Performace per Block [%]
96	86.06	1.0	37-39	100.0
144	60.60	1.42	25-26	95.2
192	48.01	1.79	18-20	89.6
240	41.11	2.09	14-16	82.6
288	34.93	2.46	12-13	81.0
336	32.98	2.60	10-12	75.5

Table 4.1: Results from the scaling test normalized to a run with 96 cpus; because of the increased communication overhead, each cpu should handle as many block as possible in terms of memory requirements.

2.40 GHz) and at the North-German Supercomputing Alliance in Berlin on the Cray XC30.

(a) Wallclock Time

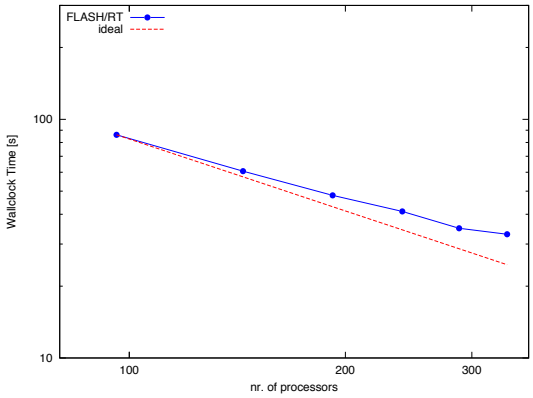

(b) Speedup

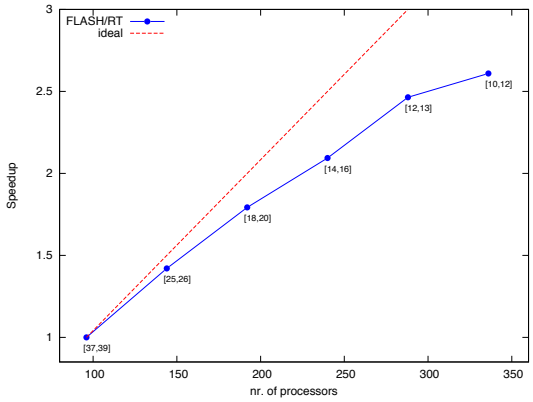

(c) Performance per Block

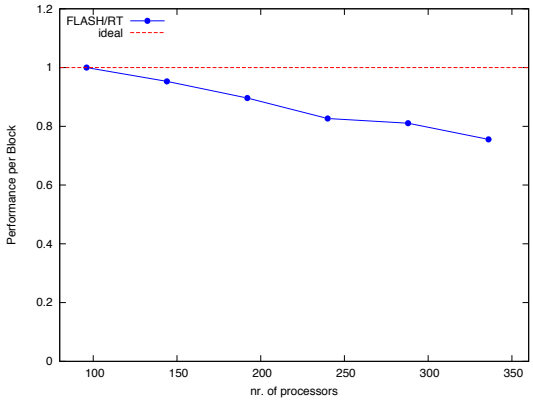

(d) fractional runtimes

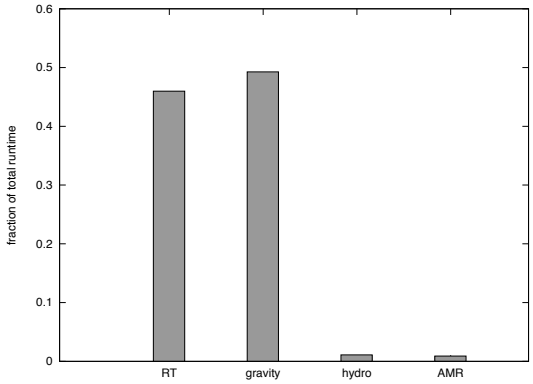

Figure 4.10: Results from the parallel scaling test; In a) the total wallclock time for the formal solution averaged over 50 iteration cycles is shown. In b) the speedup normalized to the wallclock time using 96 cores is shown. The number in brackets denote the minimum and maximum blocks per core, which is the result from the Morton space-filling curve. In c) the performance per block is shown, which decreases by roughly 10% if the number of cores is doubled. In d) the fractional runtimes for the most costly steps of the the collapse simulation (Section 5.1) is shown. All computations were performed using 192 directions.

5

3D Collapse Simulations

In this section, we show results from full 3D radiation hydrodynamical simulations performed with FLASH/RT. Since we aim to use our framework for the modelling of radiative feedback in star formation simulations, we show the capabilities of our method in a series of self-gravitating collapsing cloud simulations. We follow the collapse until the first hydrostatic core is formed and before the dissociation of hydrogen molecules start (the first collapse). In Section 5.1, we show results from a basic collapse simulation without rotation and compare the resulting profiles to other similar works. Afterwards, we show results from more complex simulations including rotation and turbulence (Section 5.2) and compare the results to a simulation without modelling radiative transfer. In Section 5.3, we show results from simulations of the formation of a binary system based on the work by Boss and Bodenheimer (1979). The angular resolution of the radiative transfer calculations are the same for all three collapse simulations, and we use 768 directions to compute the radiation field (nSide=8 for the HEALPix tessellation).

Opacities

Since our solver does not yet support any frequency dependence, the source function S is only determined by the frequency-integrated thermal emission of the gas ($S = B = \frac{\sigma_{\mathrm{SB}} T^4}{\pi}$), and we neglect any scattering processes. Consequently, we have to use frequency-integrated mean dust opacities. For this purpose, we choose the Planck mean opacities by Semenov et al. (2003). In their work, the dust composition model takes into account the evaporation temperatures of ice, silicates, iron as well as their density dependencies. We coupled their subroutines[3] for computing temperature and density dependent dust opacities into FLASH, and we choose the input parameters for spherical homogeneous dust grains with a normal relative iron content in the silicates of Fe/(Fe+Mg) = 0.3.

5.1 Collapse without Rotation

In this section, we study the collapse of a spherical, homogeneous, and gravitationally unstable density distribution. The initial conditions do not contain any turbulence or density perturbations and hence, the results are spherically symmetric. This setup represents a common benchmark for the capabilities of a radiation hydrodynamical astrophysical computer code, and we compare our results to similar work done by Commerçon et al. (2011), Masunaga et al. (1998), and the pioneering simulations of Larson (1969).

Initial Conditions

For the collapse simulation, we start with highly gravitationally unstable initial conditions. The cloud of one solar mass consists of a homogeneous sphere with radius $R_0 = 7.07 \times 10^{16}$ cm($\approx$ 4725AU) and and density $\rho_0 = 1.38 \times 10^{-18}\ \mathrm{g\,cm^{-3}}$, which results in an initial free-fall time (Equation 1.9) of $t_{\mathrm{ff}} \approx 56.67\,\mathrm{kyrs}$. The size of the 3D computational domain is four times the initial cloud radius R_0 in each dimension. The surrounding gas density is a hundred times less than the initial cloud density ρ_0, and the cloud is initially in thermal equilibrium with the ambient gas at a temperature of $T = 10\,\mathrm{K}$ resulting in an initial isothermal sound speed of $c_{\mathrm{s}} \approx 0.195\,\mathrm{km\,s^{-1}}$. We use an ideal gamma equation of state (EOS) relating the internal energy and gas density to the pressure and temperature (Section 2.2.1) with the adiabatic exponent

[3] http://www.mpia-hd.mpg.de/homes/henning/Dust_opacities/Opacities/opacities.html

$\gamma = 5/3$. Since the cloud is initially not in pressure equilibrium with its surroundings, FLASH's hydrodynamical solver drives a weak shock wave into the ambient gas which is soon dissipated. To prevent our radiation solver from resolving this shock in terms of radiative energy exchange (which would result in rather small time steps), we do not couple the radiation field to the hydrodynamics outside of R_0 but rather keep the ambient gas and radiation temperature fixed.
The initial conditions result in a gravitationally unstable cloud which contains nearly two Jeans masses. To ensure a proper resolution and avoid artificial fragmentation during the collapse, we use the Jeans condition by Truelove et al. (1997) as the refinement criterion of the AMR grid. In our case, we use at least $\mathrm{N_j} = 9$ grid cells per Jeans length (Equation 1.7). To resolve the first hydrostatic core properly, we allow a maximum linear resolution of $\Delta x \approx 0.07\mathrm{AU}$ which requires the AMR grid to cover 11 levels of resolution.
The summarized initial conditions are:

$$\begin{aligned}
\text{Mass} \quad & M = 1.0\,\mathrm{M}_\odot, \\
\text{Density} \quad & \rho_0 = 1.38 \times 10^{-18}\,\mathrm{g\,cm^{-3}}, \\
\text{Temperature} \quad & T = 10\,\mathrm{K}, \\
\text{Angular Velocity} \quad & \Omega = 0.0\,\mathrm{rad\,s^{-1}}, \\
\text{Radius} \quad & R = 7.07 \times 10^{16}\,\mathrm{cm}, \\
\text{Free Fall Time} \quad & t_{\mathrm{ff}} = 56.67\,\mathrm{kyrs}.
\end{aligned}$$

Results

The cloud core starts to collapse and as soon as the maximum density in the cloud exceeds about $10^{-13}\mathrm{g\,cm^{-3}}$, the central regions of the cloud core become optically thick. At this point, the central temperature starts to rise rapidly and the following evolution proceeds almost adiabatically with more gas falling onto the central hydrostatic core (see also Section 1.3.1). Since the simulation does not contain any rotation or turbulence, the 3D solution is spherically symmetric, and we present the results in the form of averaged radial profiles. The profiles for density, radial velocity, temperature, optical depth, and central mass after $1.036 \times t_{\mathrm{ff}}$ are shown in Figure 5.1. The resulting hydrostatic core has a mass of $M_{\mathrm{fc}} \approx 1 \times 10^{-2}\mathrm{M}_\odot$, a radius of $R_{\mathrm{fc}} \approx 4\mathrm{AU}$, and a central temperature of $T_{\mathrm{c}} \approx 186K$. The boundary of the core can be identified easily in the velocity profile, where there is a sudden decrease in the infall velocity (the accretion shock). Inside the core, the infall does not stop completely indicating that the core is only quasi-hydrostatic.

Reference	R_{fc} [AU]	$M_{fc}[M_\odot]$	T_{fc}[K]	T_c [K]
This work	4	1×10^{-2}	50	186
Commerçon et al. (2011)	8	2.1×10^{-2}	81	396
Masunaga et al. (1998)	8	$\approx 10^{-2}$	60	200
Larson (1969)	4	1×10^{-2}	-	170

Table 5.1: Comparison of simulation results; R_c is the radius of the first core, M_{fc} is the core mass, T_{fc} the central temperature and T_{fc} is the temperature at R_{fc}.

Our results are quantitatively very similar to those of Larson (1969) and qualitatively very similar to the more recent works by Masunaga et al. (1998) and Commerçon et al. (2011). Table 5.1 shows an overview of the characteristic temperature, mass and radius of the first core in comparison to these works (the common reference point is when the maximum central density of the first core reaches $\rho_{fc} \approx 2 \times 10^{-10}\mathrm{gcm}{-}3$). Apparently, our computations produce qualitatively similar results, although the methods invoked in the other works are quite different and use different initial conditions and opacity models.

5.2 Collapse with Rotation and Turbulence

This simulation run has very similar initial conditions as described in the previous section except that we add some rotational and turbulent energy. The cloud is initially in a rigid body rotation around the z-axis at the center of the simulation box. The ratio of rotational and gravitational energy is given by

$$\beta = \frac{1}{3}\frac{R_0^3\,\Omega_0^2}{\mathrm{G}\,\mathrm{M}_0}. \tag{5.1}$$

We choose $\beta = 0.03$ which gives an initial angular velocity of $\Omega_0 = 1.886 \times 10^{-13}\,\mathrm{rad\,s^{-1}}$ and agrees with typically observed values of molecular cloud cores (Goodman et al., 1993). In addition, we superimpose a turbulent velocity perturbation on the initial uniform angular velocity field. The construction of the velocity perturbation is based on the theory for incompressible turbulence by Kolmogorov (1941), in which the kinetic energy E of the velocity fluctuation with wave number k is described by a power spectrum

$$E(k) \propto k^p. \tag{5.2}$$

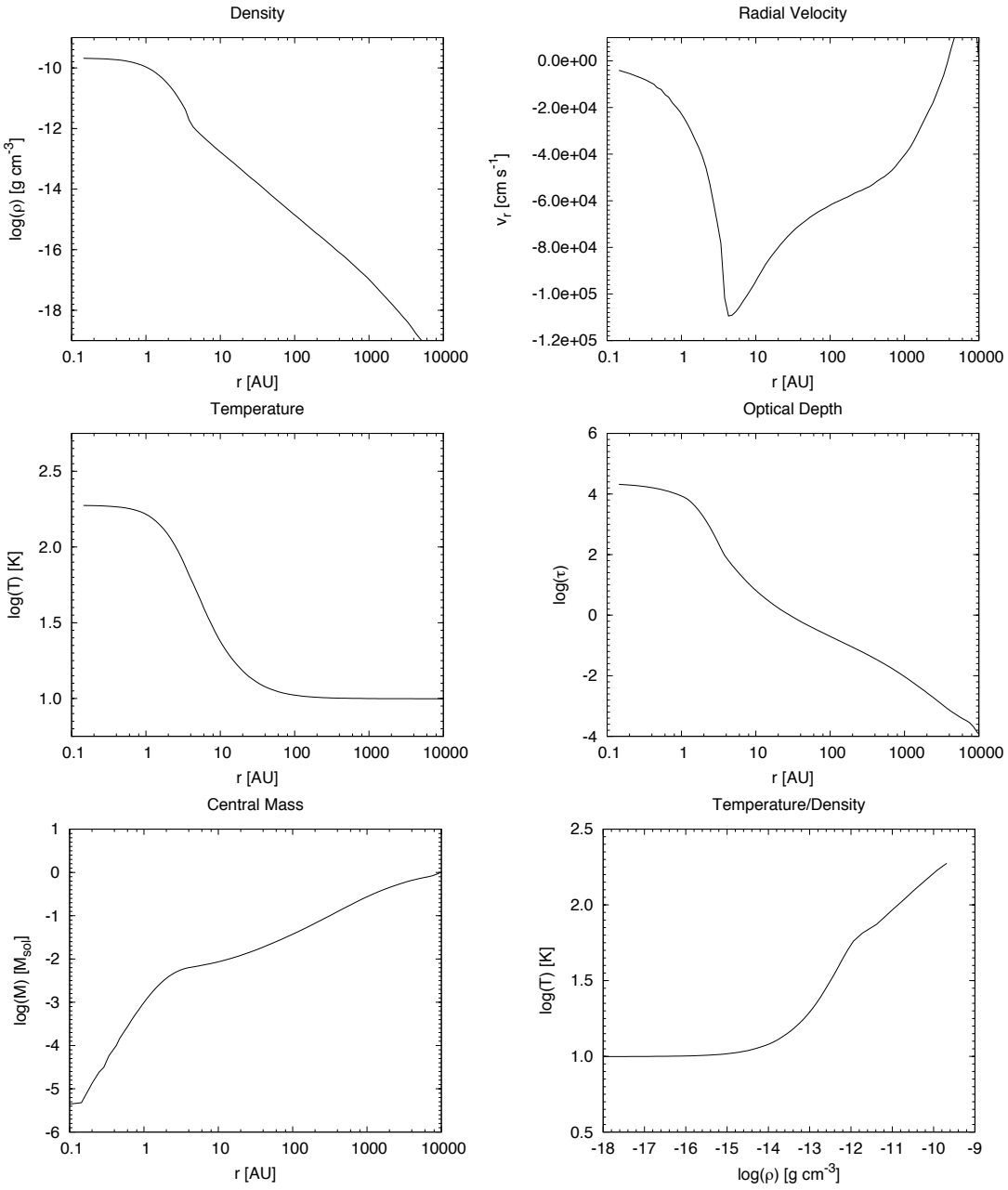

Figure 5.1: Profiles of the collapse simulation after $t = 1.036\, t_{\rm ff}$; the maximum density at the core center is $\rho_c \approx 2.0 \times 10^{-10}$ g cm^{-3} with a temperature of $T_{\rm c} \approx 186$ K, a radius of $R_{\rm fc} \approx 4$ AU and a mass of $M_{\rm c} \approx 10^{-2}\, {\rm M}_\odot$

The wave number $k = 2\pi/l$ is the inverse of the length scale l of a turbulent fluctuation (sometimes called *eddy*). In our case, the spectrum has a power law index of $p = -2$ resembling a Burgers type model of turbulent energy decay. The geometries and density distribution of the initial cloud core are the same as for the simulation without rotation and turbulence.
In addition to the simulation run with FLASH/RT, we also run the simulation without modelling radiative transfer. Instead, we use a barotropic EOS with a density-dependent effective adiabatic exponent γ that mimics radiative cooling. The internal energy/temperature is fixed at $T = 10\,\mathrm{K}$ as long as the gas density is less than $\rho \approx 10^{-15}\,\mathrm{g\,cm^{-3}}$ (isothermal). Above this threshold density, the temperature rises slowly with $\gamma = 1.1$ until the adiabatic exponent becomes $\gamma = 4/3$ above $\rho \approx 10^{-13}\,\mathrm{g\,cm^{-3}}$ (adiabatic). We ran the simulation including radiative transfer as well as the reference run with the barotropic EOS until the formation of the first hydrostatic core with a central density of $\rho \approx 10^{-11}\,\mathrm{g\,cm^{-3}}$. At this point, both simulations cover 9 different levels of resolution in the AMR grid with a maximum linear resolution of $\Delta x \approx 0.57\,\mathrm{AU}$ while the whole simulation box has a linear extent of $18903\,\mathrm{AU}$.
The summarized initial conditions are:

$$
\begin{aligned}
\text{Mass} \quad & M = 1.0\,\mathrm{M_\odot}, \\
\text{Density} \quad & \rho_0 = 1.38 \times 10^{-18}\,\mathrm{g\,cm^{-3}}, \\
\text{Temperature} \quad & T = 10\,\mathrm{K}, \\
\text{Angular Velocity} \quad & \Omega = 1.886 \times 10^{-13}\,\mathrm{rad\,s^{-1}}, \\
\frac{\text{Rotational Energy}}{\text{Gravitational Energy}} \quad & \beta = 0.03, \\
\text{Radius} \quad & R = 7.07 \times 10^{16}\,\mathrm{cm}, \\
\text{Free Fall Time} \quad & t_\mathrm{ff} = 56.67\,\mathrm{kyrs}.
\end{aligned}
$$

Results

The rotational energy and the superimposed turbulent velocity perturbations break the symmetry of the simulation. Figure 5.2 shows the column densities along the main axes of the inner region where the dense first core has formed after about $60\,\mathrm{kyrs}$ ($\approx 1.07\,t_\mathrm{ff}$) with a maximum gas density of $\rho_\mathrm{fc} \approx 10^{-11}\,\mathrm{g\,cm^{-3}}$. Because of the additional rotational and turbulent energy, the formation of the first core is deferred and forms later than in the previous simulation (Section 5.1). The conservation of angular momentum causes the first core to be flattened roughly

along the z-axis and the density distribution shows a flat disc-like structure revolving around the central compact hydrostatic core. The resulting density distribution is roughly the same as in the reference run without radiative transfer. The initial collapse which seeds the formation of the central core does mostly occur in the isothermal phase, hence, modelling radiative feedback does not influence the initial formation of the core significantly. However, Figure 5.3 shows the resulting density weighted temperature averages along the main axes in the central regions around the first core (e.g $\int \rho T \, dz / \int \rho \, dz$). The left column shows the results including radiative transfer (FLASH/RT) while the right column shows results from the reference run. The FLASH/RT model clearly shows how the central core heats the surrounding gas to a temperature roughly 30% higher than in the reference run (like in Price and Bate (2010)). The resulting temperature-density distribution in comparison to the barotropic EOS is shown in Figure 5.4.
Unfortunately, our FLASH/RT simulations are very costly (see Section 4.3 for more details) and currently, it is not feasible to continue these simulations without coupling the radiative transfer solver to a subgrid model for the formation of the central core, e.g., sink-particles (see Section 3.4). However, our current test simulations show the first stages of disc formation and the importance of modelling radiative transfer accurately. Since the thermodynamics of the gas significantly influence the fragmentation behaviour of the disc, modelling radiative transfer is indispensable to study the further evolution of the disc and the surrounding gas envelope.

5.3 Binary Formation

An important problem in the theory of star formation is the fragmentation of a molecular cloud into at least two or more protostellar cores. This case was investigated by Boss and Bodenheimer (1979) who addressed the problem by comparing 2D hydrodynamical simulations with two different numerical methods (fixed and moving mesh) but without explicitly modelling radiative transfer. Whitehouse and Bate (2006) repeated those simulations using an SPH code and modelling radiative transfer in the FLD approximation. They found that a barotropic EOS underestimates the temperature by a factor of 2-3 in the density maximum and up to an order of magnitude in other regions of the cloud. Since the temperature has an important influence on the fragmentation behaviour (see Section 1.3.3), Whitehouse and Bate (2006) emphasized the importance of modelling radiative transfer explicitly.
In this section, we show our results from a radiation hydrodynamical simulation based on the

initial conditions by Boss and Bodenheimer (1979), which are:

$$
\begin{aligned}
\text{Mass} \quad & M = 1.0\,\mathrm{M}_\odot, \\
\text{Density} \quad & \rho_0 = 1.44 \times 10^{-17}\,\mathrm{g\,cm^{-3}}, \\
\text{Temperature} \quad & T = 10\,\mathrm{K}, \\
\text{Angular Velocity} \quad & \Omega = 1.6 \times 10^{-12}\,\mathrm{rad\,s^{-1}}, \\
\frac{\text{Rotational Energy}}{\text{Gravitational Energy}} \quad & \beta = 0.2, \\
\text{Radius} \quad & R = 3.2 \times 10^{16}\,\mathrm{cm}, \\
\text{Free Fall Time} \quad & t_{\mathrm{ff}} = 17.54\,\mathrm{kyrs}.
\end{aligned}
$$

The main difference to our previous calculations is that the initial cloud core has a much higher rotational energy of $\beta = 0.2$. Furthermore, we do not include turbulence but a non-axisymmetric density perturbation of mode $m = 2$ with an amplitude of 0.5, which depends only on the azimuthal angle ϕ:

$$\rho = \rho_0(1 + 0.5\cos(2\phi)). \tag{5.3}$$

The cloud core has the same mass as in the previous runs but only about half of its radius. Hence, the initial cloud core is about an order of magnitude denser and the initial free-fall time is shorter ($t_{\mathrm{ff}} \approx 17.54\mathrm{kyrs}$). The fast rotation of the dense core together with the density perturbation seed the formation of a binary system.

Results

Figure 5.5 shows the time evolution of the column densities along the rotation axis (z-axis) in the FLASH/RT run. The initial cloud fragments and forms two cores. Figure 5.6 shows the inner region ($\approx$ 2000 AU) at the end of the simulation run after $t \approx 21\,\mathrm{kyrs} \approx 1.2\,\mathrm{t_{ff}}$ when both cores have reached a maximum density of about $10^{-11}\,\mathrm{g\,cm^3}$. At this point, the simulation covers 7 levels of refinement with a maximum linear resolution of $\Delta x \approx 1\,\mathrm{AU}$. The formation of the binary system is seeded very early in the simulation through the density perturbation and the high angular momentum of the cloud. While in this early phase the cloud is still in its isothermal phase, radiative feedback does not have a large impact on the early fragmentation behaviour. However, Figure 5.7 shows a comparison between the density weighted mean temperature along the rotation axis of both the simulation with radiative transfer (top) and with a barotropic EOS

(bottom), and Figure 5.9 shows the resulting temperature-density distribution. Modelling the energy transport with radiative transfer causes the cores to heat up their surroundings very similar to the previous simulation in Section 5.2. Since the thermodynamical properties of the gas determine its fragmentation behaviour, this has a significant influence on the fragmentation behaviour of a circumstellar disc.

Figure 5.8 shows the early process of disc formation around one of the cores. Again, the temperature structure reveals a hotter region where the infalling gas hits the emerging disc which can not be modelled using the barotropic EOS. This radiation shock is caused by the infalling gas which is abruptly slowed down when it reaches the dense disc structure. The infalling gas encounters a hydrodynamical shock front while radiation, which is transported through the shock front, preheats the infalling gas before and after passing the shock.

5.4 Summary

We have shown the first results from 3D radiation hydrodynamical simulations with our FLASH/RT code which explicitly models the effects of radiative transfer in a star formation simulations. We are able to follow the collapse until about $t \approx 1.2\, t_{\mathrm{ff}}$ when the first hydrostatic cores with a circumstellar disc emerge. However, modelling radiative transfer is a rather costly computation (Section 4.3) in comparison to the solution of the Euler equations. To study the long term evolution of the protostar including the circumstellar disc, we have to restrict the spatial resolution which significantly reduces the communication overhead in the radiative transfer solver (see also our discussion on the communication overhead in the following chapter). This requires a subgrid model for the protostellar core evolution, e.g., by using the sink-particle implementation by Federrath et al. (2009) and the protostellar evolution model by Offner et al. (2009). This requires to couple our radiative transfer solver to these modules in FLASH to improve the feasibility of 3D simulations with FLASH/RT.

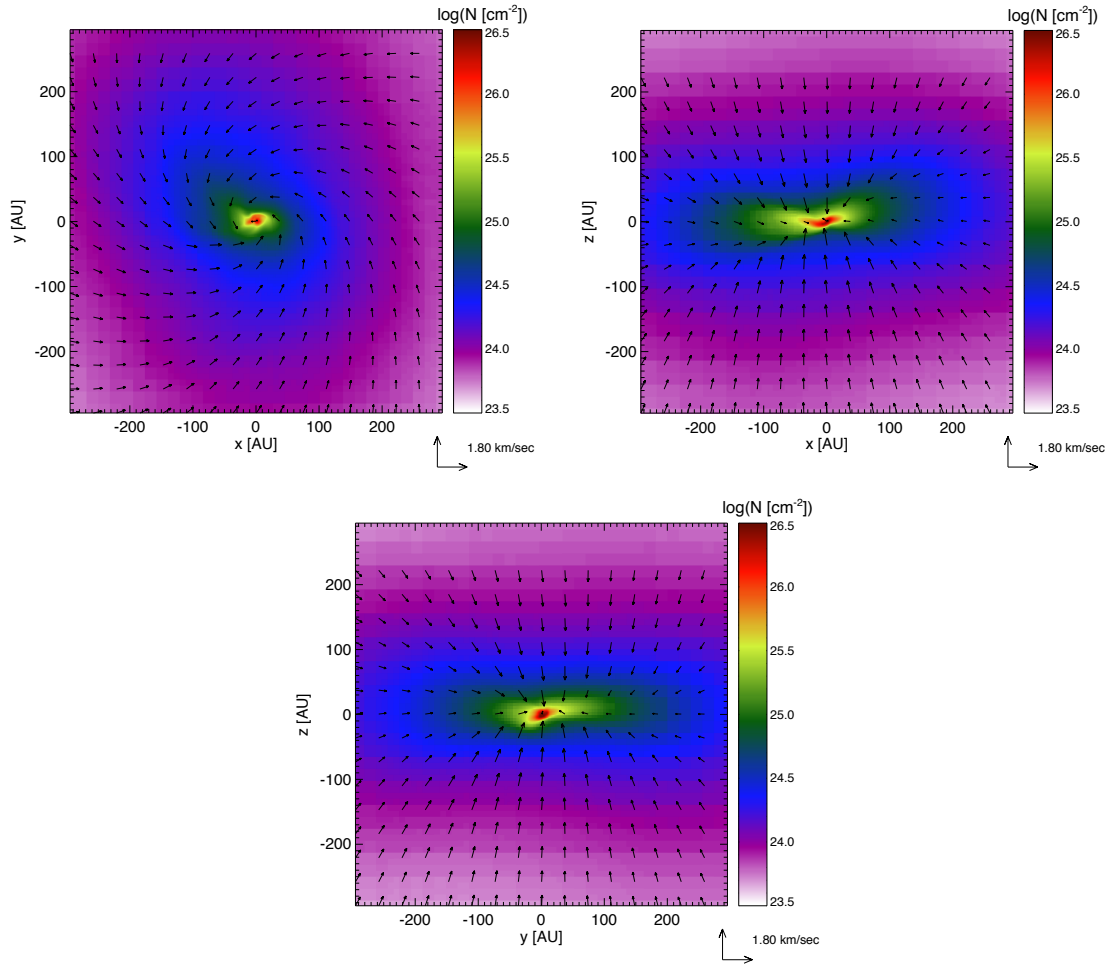

Figure 5.2: Column densities along the main axes of the simulation box after the formation of the first hydrostatic core at $t \approx 60\,\mathrm{kyrs} \approx 1.07\,\mathrm{t_{ff}}$. The rotational energy forces the gas to accumulate in a circumstellar disc (in the xy-plane) around the first core.

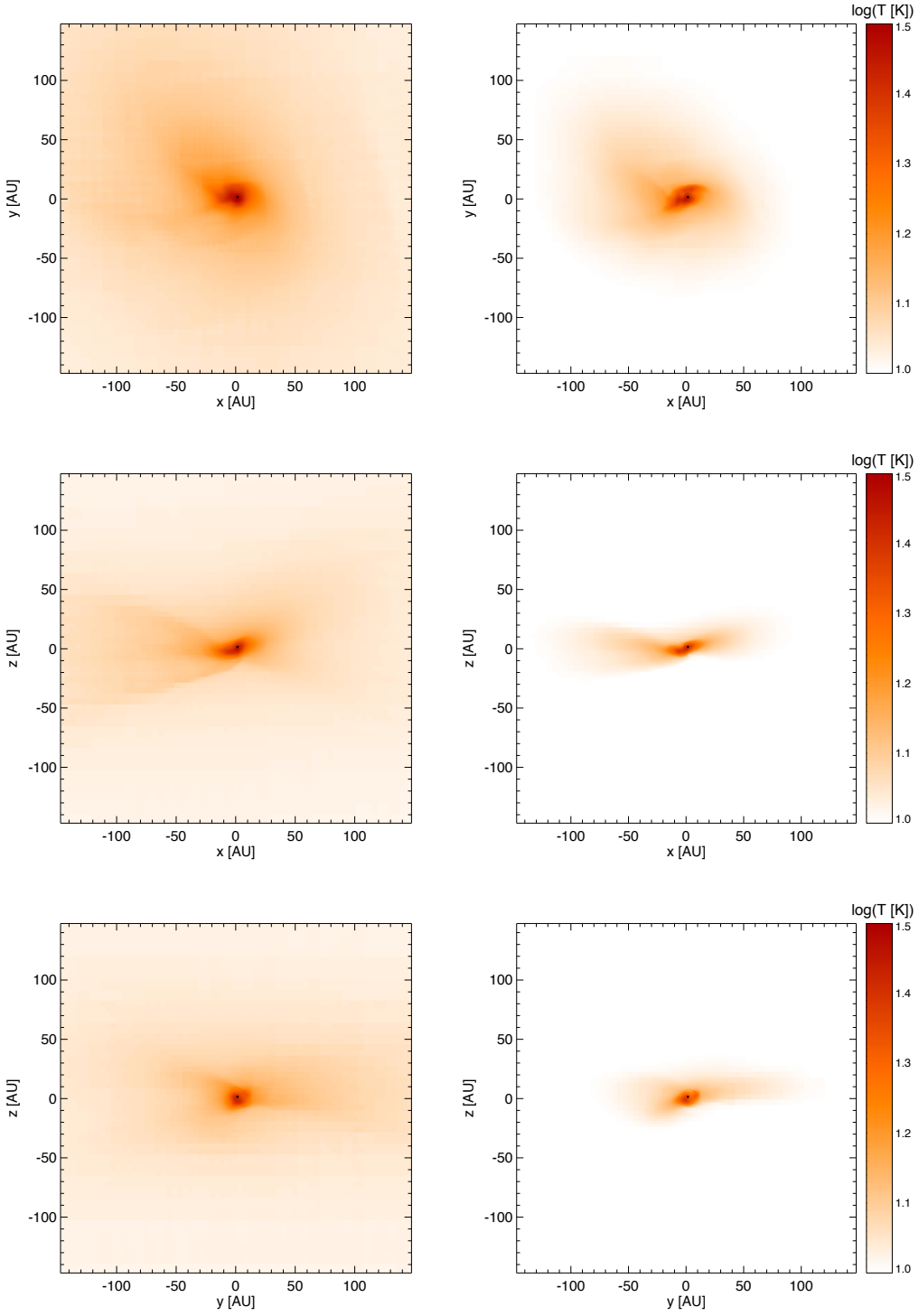

Figure 5.3: The plots show density weighted temperature averages (e.g., $\int \rho T \, dz / \int \rho \, dz$) from hydrodynamical collapse calculations. *Left:* Results from the FLASH/RT calculations including radiative transfer. *Right:* Results from FLASH calculations using a barotropic equation of state. The ambient gas temperature in the FLASH/RT models is about 30% higher.

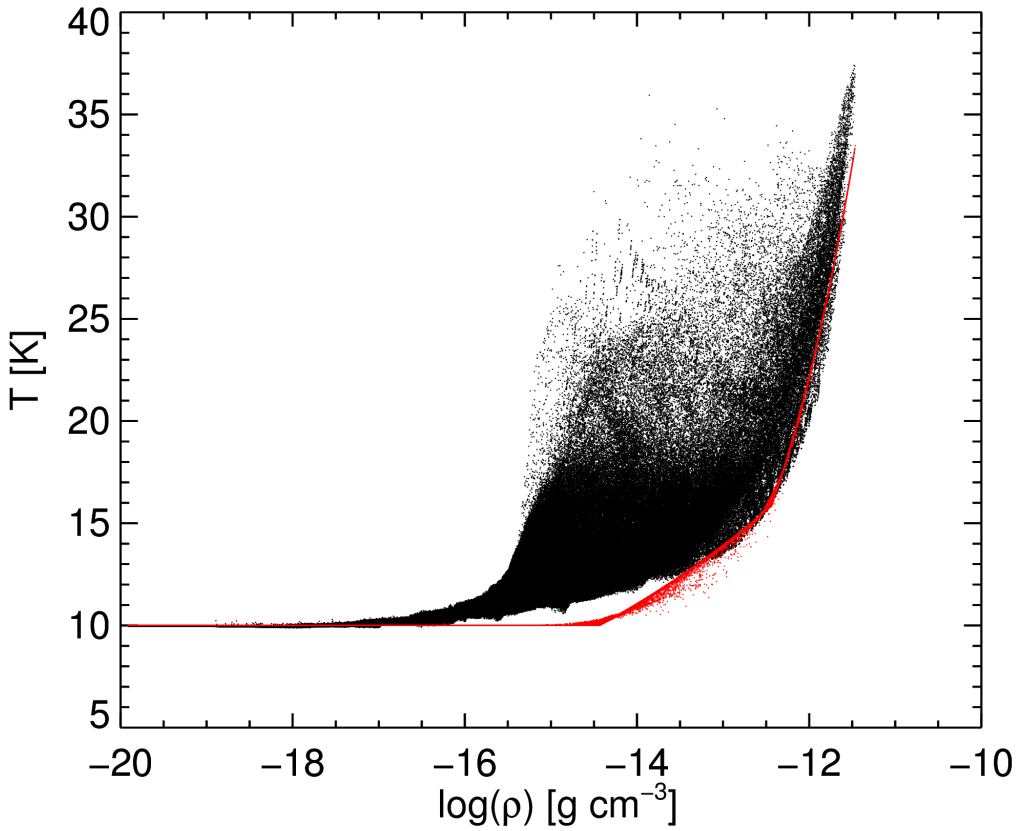

Figure 5.4: Temperature distribution with respect to the gas density in the simulation box at the end of the binary simulation. Black dots show the temperature distribution from the FLASH/RT run, red dots show the temperature-density dependence of the barotropic equation of state.

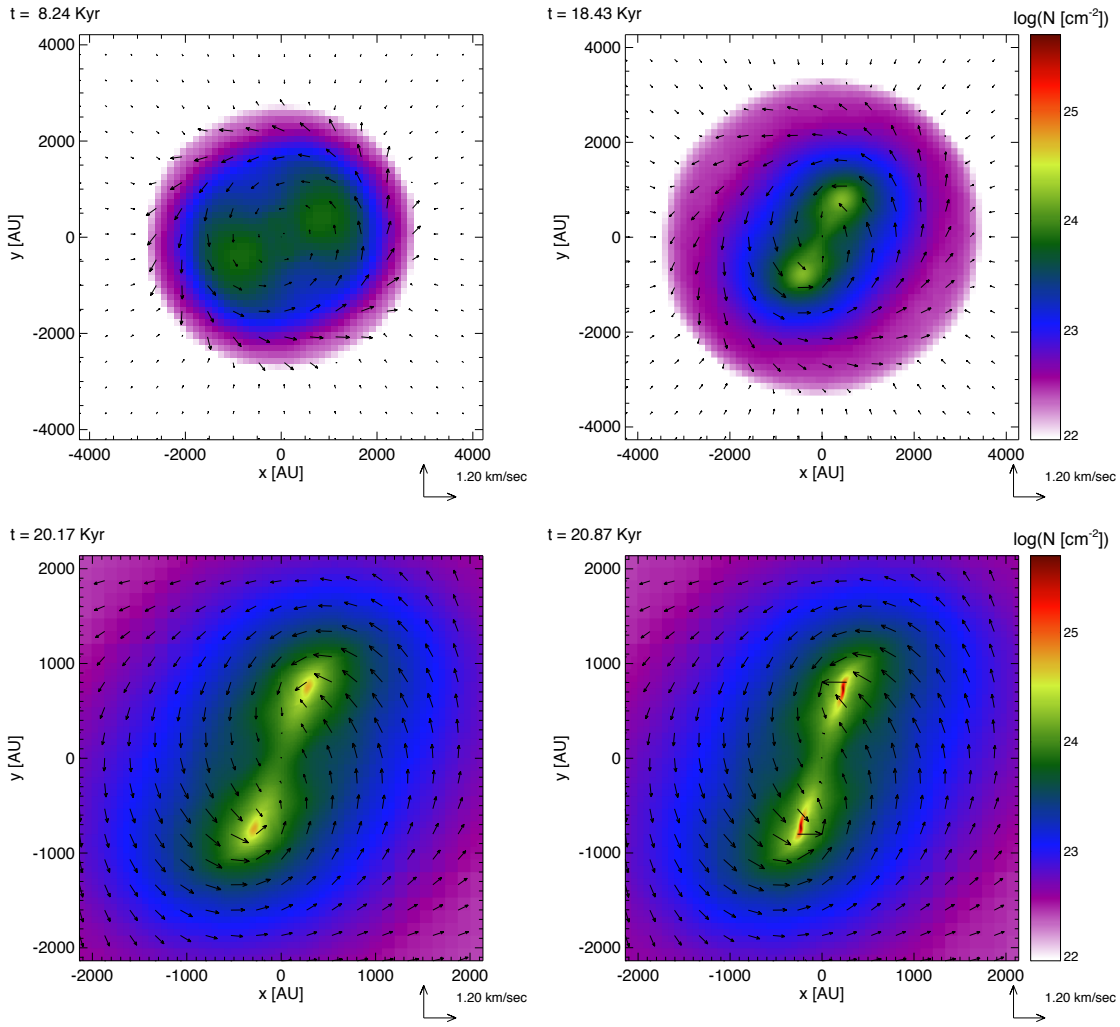

Figure 5.5: Snapshots of the time evolution from the FLASH/RT calculations of the formation of a binary system. Initial conditions are based on the work by Boss and Bodenheimer (1979). The snapshots show the evolution of the column densities along the rotation axis (z-axis) at $t = 0.46\,t_{\rm ff}$ (top left), $t = 1.05\,t_{\rm ff}$ (top right), $t = 1.15\,t_{\rm ff}$ (bottom left) and $t = 1.19\,t_{\rm ff}$ (bottom right).

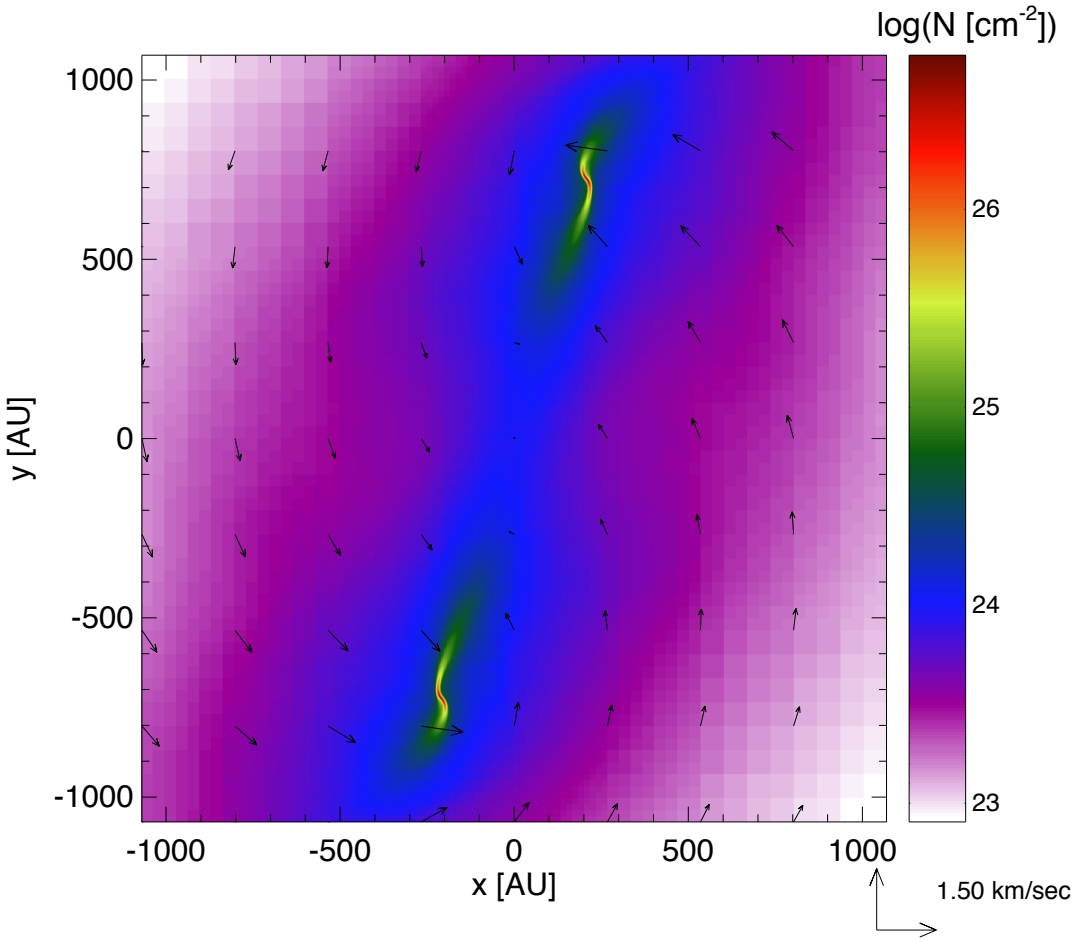

Figure 5.6: Detailed view of the inner region of the simulation box at the end of the binary simulation run based on the initial conditions by Boss and Bodenheimer (1979). The plot shows column densities along the rotation axis (z-axis) after the formation of the first hydrostatic cores at $t \approx 21\,\mathrm{kyrs} \approx 1.2\,\mathrm{t_{ff}}$ with a maximum density of $\rho \sim 10^{-11}\,\mathrm{g\,cm^{-3}}$. At the end of the simulation run, the simulation covers 7 levels of refinement with a maximum linear resolution of $\Delta \approx 1\mathrm{AU}$.

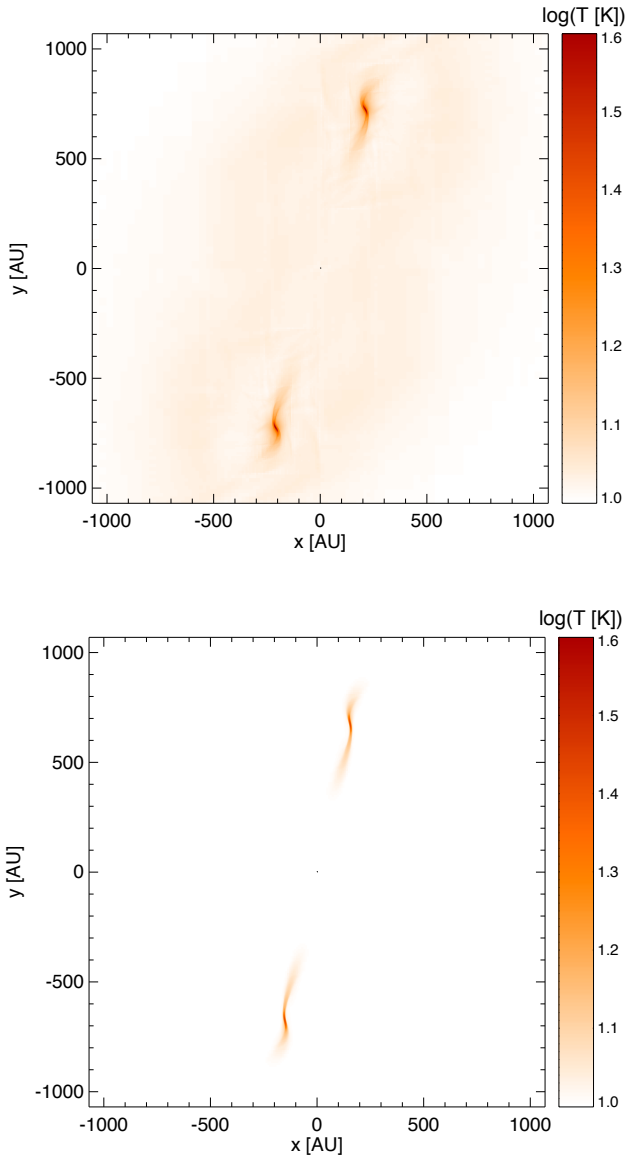

Figure 5.7: Effects of radiative transfer on the gas temperature: The plots show density weighted temperature averages ($\int \rho T \, dz / \int \rho \, dz$) from our hydrodynamical collapse calculations of the binary system formation at the end of the simulation runs at $t \approx 1.2 \, t_{\rm ff}$. At this point, the hydrostatic cores have reached densities of about $\rho \sim 10^{-11} \, {\rm g \, cm^{-3}}$ at temperatures of $T \approx 40 \, {\rm K}$. *Top:* Results from the FLASH/RT calculations including radiative transfer. *Bottom:* Results from FLASH calculations using a barotropic equation of state. Modelling radiative transfer with FLASH/RT accounts for radiative heating by the two cores which results in an ambient gas temperature of up to 30% higher than in the reference run.

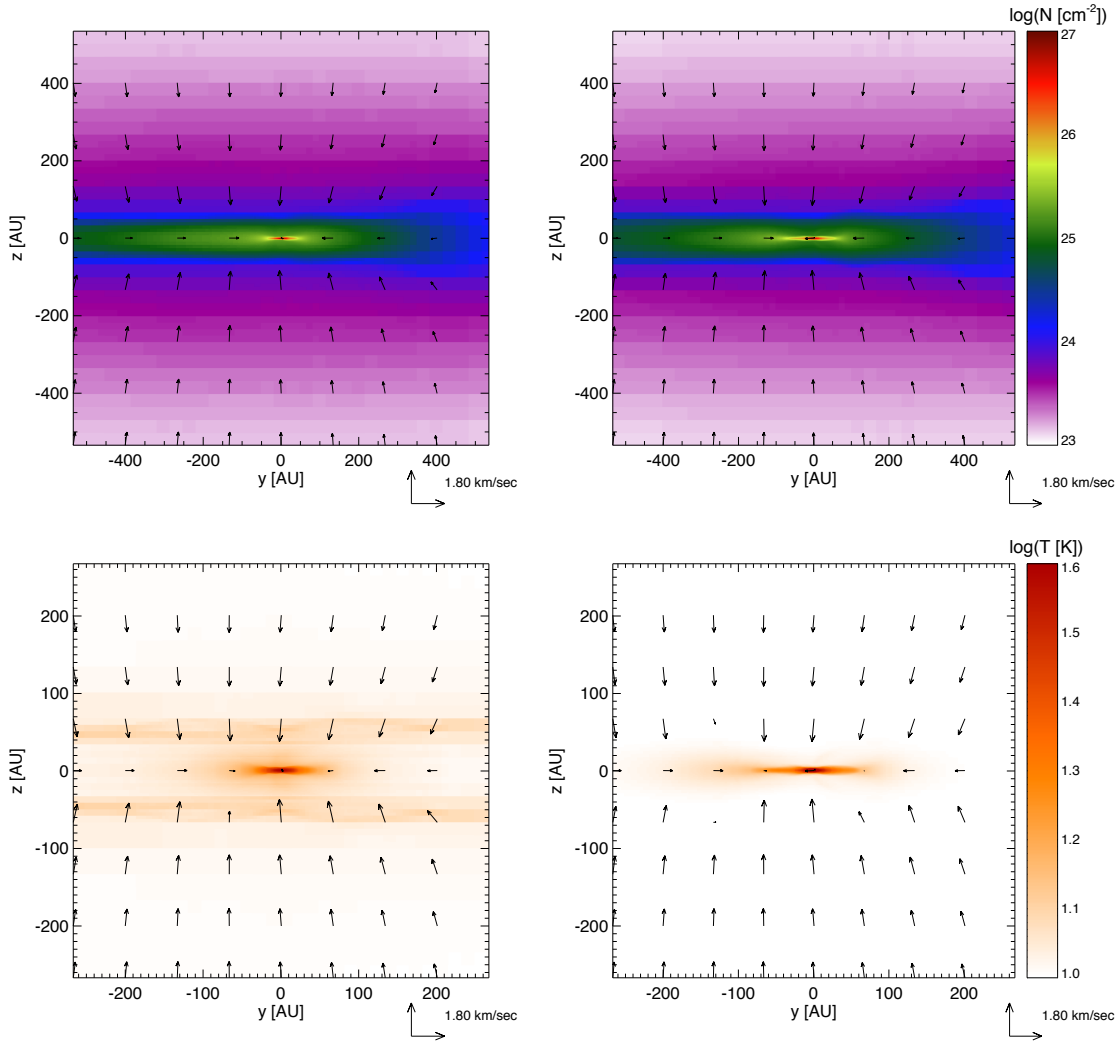

Figure 5.8: Effects of radiative transfer on the ambient gas temperature for one of the cores in the binary formation simulation. The plots show column densities and density weighted temperature averages ($\int \rho T \, dx / \int \rho \, dx$) after $t \approx 21\,\mathrm{kyrs} \approx 1.2\,\mathrm{t_{ff}}$. *Left:* Column densities and temperatures from the FLASH/RT calculations including radiative transfer. *Right:* Column densities and temperatures from FLASH calculations using a barotropic equation of state. The FLASH/RT simulations show the radiation shock where gas falls onto the circumstellar disc.

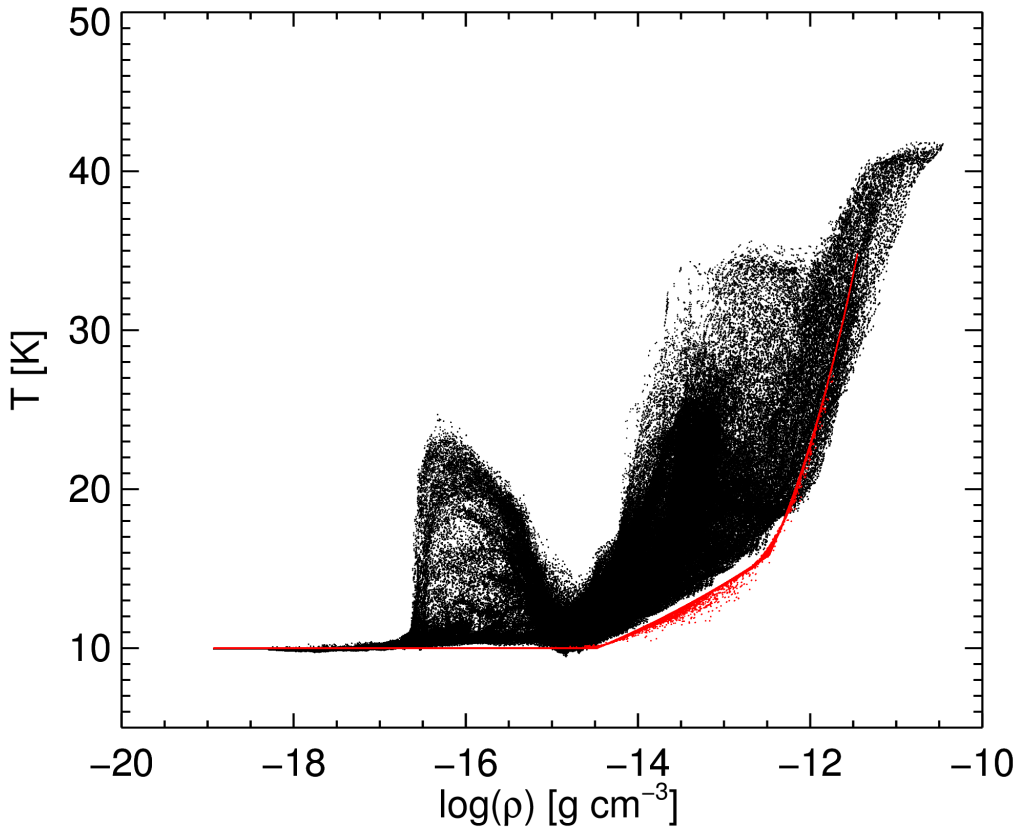

Figure 5.9: Temperature distribution with respect to the gas density in the simulation box at the end of the binary simulation. Black dots show the temperature distribution from the FLASH/RT run, red dots show the temperature density dependence of the barotropic equation of state.

6

Discussion

We have implemented a new radiative transfer solver based on the method of hybrid characteristics. The solver successfully reproduces solutions of standard radiative transfer problems, including NLTE and continuum radiative transfer as well as the diffusion limit. We proved the feasibility of the method in a series of collapse simulation, where radiative transfer is the dominant cooling process during the formation of the first protostellar core. In contrast to the FLD approximation, our method preserves the anisotropy of the radiation field, which becomes crucial in the transition from optically thin to optically thick regions (e.g, a protostellar disc). The radiation solver is implemented in the framework of the MHD code FLASH which allows for a straightforward coupling of both codes (e.g., the collapse simulations). Our implementation fits very well into the parallel design of the FLASH code which combines AMR with domain decomposition.

However, the culprit of the hybrid characteristics algorithm mainly lies in its rather large communication overhead which is caused by the communication of non-local radiative contributions. By now, this is done without explicitly checking how large these contributions might be. One alternative is to communicate the radiation field successively between subdomains similar to the

method by Davis et al. (2012). We implemented this idea for testing purposes by using only guard cell information for the irradiation of a subdomain. The communication has to be repeated until the radiation field converges for each direction of the specific intensity field. If the whole computational domain is optically thick, the radiation field converges very fast. However, especially the transition regions from optically thin to optically thick regimes can easily require a lot of additional communication to transport radiation through the whole domain which causes a communication overhead even larger than for the hybrid characteristics method, especially if a high angular resolution is required. However, a combination of both methods might be possible.
Our method has the significant advantage of working in an AMR framework with domain decomposition for parallelization. Methods like Monte Carlo simulation are usually parallelized by simulating the propagation of several photon packets at the same time, which requires information about the whole domain to be communicated. This causes rather strong limitations concerning the resolution and range of scales if a radiative transfer solver is coupled to a hydrodynamical code. Our method overcomes this problem and gives rise to a number of possible improvements to solve some of the problems we encountered during this work. In the following, we discuss the most important.

6.1 The Problem with Time Dependence

This work mainly deals with the implementation of an adaptive raytracer which is used to perform a formal solution of the RTE. More precisely, we solve the time-independent RTE which causes some problems, especially in the way the solver is coupled to the MHD integrator in FLASH. First, we can not account for the transport of radiation by gas advection in the dynamic diffusion limit (see also our discussion on reference frames in Section 6.3) since this requires the implicit solution of the time-dependent radiative energy term in the FLD approximation (e.g. Commerçon et al., 2011; Flock et al., 2013). However, the FLD approximation causes the problems discussed in Section 1.4 and 3.1. Therefore, it is more desirable to solve both the time-dependent hyperbolic system of moment equations for the radiation energy and flux (Equations (2.27) and (2.28)). This requires a closure relation in the form

$$\mathsf{P}_\mathrm{r} = \mathsf{f}\, E_\mathrm{r}, \tag{6.1}$$

with

$$\mathsf{f} = \frac{\mathsf{P}_r}{E_r} = \frac{\int I \mathbf{nn}\, d\Omega}{\int I d\Omega}, \tag{6.2}$$

where f is the *variable Eddington tensor*. Equation (6.1) is a generalization of the Eddington approximation in which $P_r = 1/3 E_r$. The Eddington tensor is 3×3 matrix in which the diagonal gives the bulk radiation pressure while non-diagonal elements account for shear forces. Therefore, it appears as a part of the stress-tensor in the combined momentum conservation Equation (2.48). However, since the solution of the moment equations has to be done on the hydrodynamical timescale, this approach requires an *implicit* solution scheme and a hybrid Godunov method for radiation MHD (e.g. Sekora and Stone, 2010; Jiang et al., 2012) and a much more fundamental modification of the hydrodynamical and MHD solvers in FLASH.

Another possibility to regain time dependence would be the time-discretization of the RTE itself as described in (Jack et al., 2012). In their approach, the implicit discretization is achieved by introducing an effective optical depth and a source function which contains intensity contributions from the previous time step. Neglecting any relativistic terms of order v/c, the modifications are

$$\Delta\hat{\tau} \equiv \hat{\chi}\Delta s \equiv \left(\chi + \frac{1}{c\Delta t}\right)\Delta s, \tag{6.3}$$

$$\hat{S}_n \equiv \frac{\chi}{\hat{\chi}}\left(S_n + \frac{1}{\chi}\frac{1}{c\Delta t} I_{n-1}\right). \tag{6.4}$$

The modifications are very easy to implement since the solution scheme stays the same. But this approach requires a lot of additional memory since the complete scalar field of angle-dependent specific intensities has to be stored (I_{n-1} in the effective source function). Nevertheless, this is an interesting approach in a code with parallelization based on domain decomposition which reduces the memory requirement significantly.

6.2 The Problem with Energy Exchange

We already discussed the explicit energy coupling in Section 3.4.1. The coupling follows the approach by Davis et al. (2012) and requires some restrictions on the time step since the CFL time step, in principle, can be much larger than the radiative cooling time which can lead to negative or unphysically high internal energies in the gas. The time steps in our simulations were mostly restricted to about one order of magnitude smaller than the CFL time step to overcome the prob-

lem of large internal energy fluctuations. A much more robust approach is to couple the term describing energy exchange implicitly. To emphasize this, we denote the monochromatic energy source term from Equation (3.26) here in terms of the gas temperature:

$$\frac{\partial e_{\mathrm{int}}}{\partial t} = -\kappa_a c(a_{\mathrm{R}} T^4 - E_r). \tag{6.5}$$

The source term is coupled to the internal specific gas energy e_{int} which determines the temperature itself through the equation of state (Section 2.2.1) which reads

$$e_{\mathrm{int}} = c_{\mathrm{V}} T. \tag{6.6}$$

Combining both, we can write the temperature in discretized form

$$\frac{T^{n+1} - T^n}{\Delta t} = -\frac{\kappa_a c}{c_V} \left(a_{\mathrm{R}} (T^{n+1})^4 - E_r^{n+1} \right). \tag{6.7}$$

This form defines the new temperature at time step T^{n+1} implicitly. Handling the energy exchange in the form of Equation (6.7) is used in the context of the FLD approximation (e.g. Commerçon et al., 2011; Kolb et al., 2013). In these works, the gas-radiation energy exchange is solved implicitly and simultaneously with the diffusion equation for the radiative energy. However, since the source term depends on the fourth power of the temperature, this requires a linearization so that standard methods for solving large systems of coupled linear equations can be used (e.g. preconditioning, successive over-relaxation). In our approach, this would require a Lambda iteration at each time step to find a new internal energy and temperature that are consistent with the radiative energy. This is not yet feasible and emphasizes the importance of using, e.g., the VET method to handle the *evolution* of the radiative energy.

6.3 The Problem with Reference Frames

There is a problem in deriving the inertial frame equations of radiation hydrodynamics (Equations (2.48) and (2.49)) in the way we discussed and which is often disregarded. The emissivity and opacities that appear in the exchange rates have values that are measured in the comoving frame of the radiating fluid. If we use, for instance, line opacities from a table that is a result of a laboratory experiment, those opacities are only valid in the fluid frame and *not* in the fixed frame of the Eulerian grid. Strictly speaking, one would have to solve the RTE in the comoving

fluid frame and transform the solution back into the fixed frame. The correct exchange rates to first order in $\beta = v/c$ would then be the Lorentz transformations of Equation (2.48) and (2.49) according to

$$g^0 = g^0_{(0)} + \frac{\mathbf{v}}{c^2} \cdot \mathbf{g}_{(0)}, , \tag{6.8}$$

$$\mathbf{g} = \mathbf{g}_{(0)} + \mathbf{v} g^0_{(0)}, \tag{6.9}$$

where $g^0_{(0)}$ and $\mathbf{g}_{(0)}$ are the components of the radiation four-force in the fluid frame

$$g^0_{(0)} = \int d\nu \int d\Omega \, (\eta^0_\nu - \chi^0_\nu I^0_\nu), \tag{6.10}$$

$$\mathbf{g}_{(0)} = \frac{1}{c} \int d\nu \int d\Omega \, \mathbf{n} \, (\eta^0_\nu - \chi^0_\nu I^0_\nu), \tag{6.11}$$

and the (0)-notation denotes quantities in the comoving fluid frame. The fluid velocity term in Equation (6.8) originates from the work done by the force exerted on the radiation by the fluid. The relativistic correction in the momentum exchange rate (6.9) accounts for the change of momentum caused by a relativistic increase of mass/energy. While these are the correct exchange rates for the *material* momentum (2.46) and energy equations (2.47), the *combined* equations of radiation hydrodynamics require a thorough derivation of the comoving moment equations of the radiation field.

However, our approach does not solve the combined set of equations but, instead, solves the Euler equations and the RTE successively while the coupling is done according to Equation (2.47). Furthermore, we focus on non-relativistic radiative transfer ($\beta \ll 1$) and do not solve the RTE in the fluid frame. Nevertheless, relativistic effects can still be non-negligible in regimes of high optical depths even in the case of $\beta \ll 1$. To quantify the importance of relativistic effects, Mihalas and Weibel Mihalas (1984) define three regimes of radiation hydrodynamics dependent on the optical depth and the relativistic speed in the fluid $\beta = v/c$. The cases are

$$\tau\beta \ll 1 \quad \text{streaming limit,} \tag{6.12}$$

$$\tau \gg 1, \quad \beta\tau \ll 1 \quad \text{static diffusion limit,} \tag{6.13}$$

$$\tau \gg 1, \quad \beta\tau \gg 1 \quad \text{dynamic diffusion limit.} \tag{6.14}$$

Problems arise in the dynamic diffusion limit because terms of the order of β in the radiation hydrodynamical equations can no longer be neglected if they are multiplied by quantities of order τ. A good example for the dynamic diffusion limit would be the interior of the sun. Typical rotational and convective velocities are of the order of a few $0.1\,\mathrm{cm\,s^{-1}}$ while the mean free path of a photon is about $0.01\,\mathrm{cm}$ (Mitalas and Sills, 1992). This means that in the dynamic diffusion limit, radiation is principally transported by the advection of gas. In that case, terms describing work done by radiation on the gas and the radiation enthalpy flux have to be taken into account. However, applications handling radiative transfer in the ISM, which is dominated by dust continuum opacities, are usually well in the streaming or static diffusion limit in which we neglect any relativistic contributions. Although this approach is widely used in radiation hydrodynamical simulations in the field of star formation, it is a matter of debate if this naive approach is actually reasonable. (see also chapter 6 of Castor (2007) and Krumholz et al. (2007b)).

6.4 The Problem with the Communication Overhead

Our method requires the communication of the face values which is the radiation leaving a subdomain (Section 3.2.2 and Figure 3.3). This is currently done using the OpenMPI implementation of the MPI_ALLGATHER subroutine. This involves MPI to block any further computations during the sending and receiving of data from the MPI communicator group. Figure 6.1 shows that this results in a rather large communication overhead. The problem for this is not the actual speed of data exchange but some MPI tasks waiting for other members of their communication group to become ready. This is caused by the subdomain decomposition which is handled using a Morton space-filling curve. MPI tasks handling, e.g., subdomains at the upper boundary of the computational domain need more time to walk through the AMR tree than MPI tasks handling the lower boundary *for rays that start at the lower boundary*. Consequently, the MPI_ALLGATHER subroutine blocks the MPI task that are faster in their local AMR tree walk. The alternative is to use non-blocking MPI subroutines, e.g., MPI_ISEND and MPI_IRECV, which allow MPI task to continue computations while the data exchange is handled in the background. For test purposes, we implemented a version of our raytracer replacing the MPI_ALLGATHER call through a series of non-blocking MPI_ISEND and MPI_IRECV calls so that the communication is handled in parallel with the tree walk (the tree walk is independent of the face values). However, even though the tree walk is successfully handled in parallel with the communication, it turns out that the explicit call of successive MPI_ISEND and MPI_IRECV subroutines

is almost an order of magnitude slower than the call of the blocking MPI_ALLGATHER subroutine. The communication with MPI_ISEND and MPI_IRECV requires the communication to be acknowledged by a call of the MPI_WAIT subroutine. The combined runtime of all MPI_ISEND, MPI_IRECV and MPI_WAIT calls in our test cases has always been larger than the runtime for one single blocking MPI_ALLGATHER call. The MPI_ALLGATHER subroutine actually shows the best performance for handling all-to-all communication, especially when a large number of tasks is involved and inter-node communication is required on a large supercomputer. Figure 6.2 shows the comparison of blocking and nonblocking communication for a very simple test program. In this test program, we use 12 MPI task (6 per node) which send a message of 160 MB to each other. Afterwards, each task has to sweep a large grid and do a simple calculation per grid point. The upper chart in Figure 6.2 shows the runtime using a blocking MPI_ALLGATHER call and the grid traversal is done afterwards. The lower chart shows an approach using non-blocking MPI_ISEND and MPI_IREVC calls while traversing the grid in between. Although the initial SEND and RECV calls are negligible in their runtime, the final MPI_WAIT calls, required to check for consistent communication, show a larger runtime than for the blocking MPI_ALLGATHER calls. These computations were conducted on two nodes (each with 2x Intel Xeon Hexa-Core CPUs, 2.40 GHz) of our local computing cluster "Golem" in Hamburg and using the the Intel OpenMPI (version 1.4.3) implementation. We also performed the same tests on the computing cluster "Kolob" in Heidelberg with a comparable architecture and found similar results. Several tests with our raytracer show the same significant loss in performance if non-blocking MPI communication is involved.

Instead of using non-blocking communication, we solved this problem partly by introducing *angular groups*. In this approach, all MPI tasks first compute their face values for a certain number of angles before the communication step is done. By this, the different times needed for the tree walk cancel each other out and the communication overhead is reduced. Optimally, all angles should be computed in one single MPI_ALLGATHER step, but this is restricted by the available memory. However, in our implementation the size of the angular groups can be chosen so that the user can optimally exploit available memory.

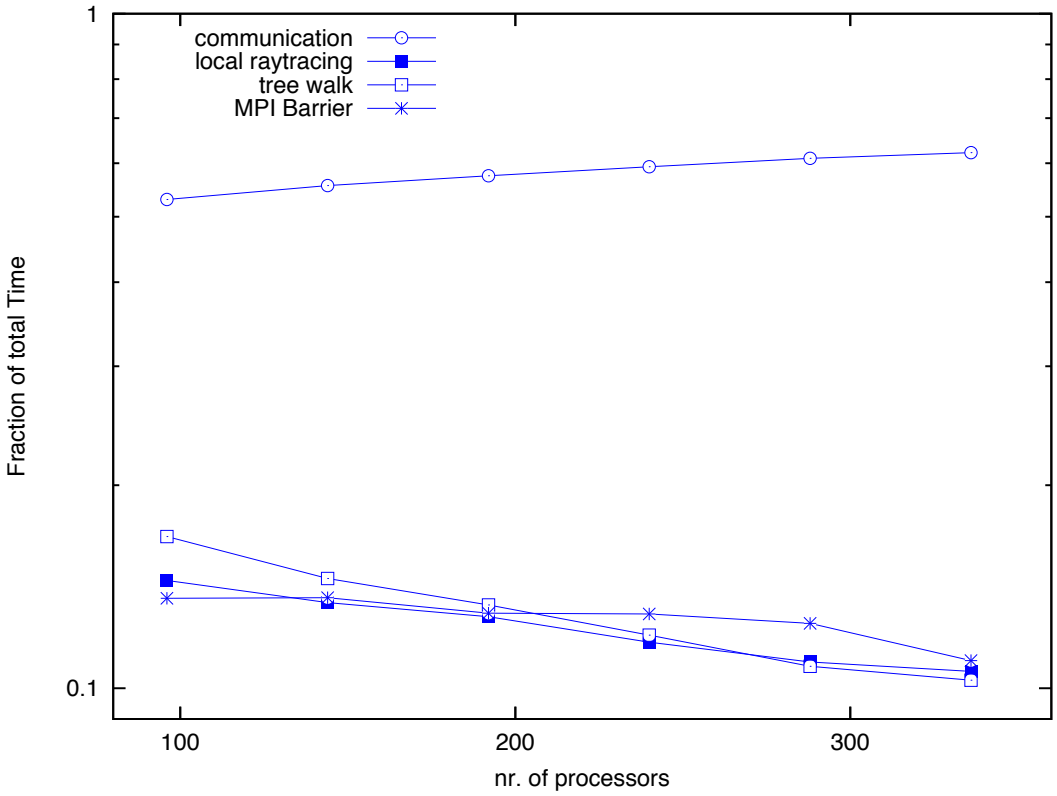

Figure 6.1: The problem with the communication overhead: the plot shows fractional runtimes of the different steps involved in the radiation transfer solver for the collapse simulations from Chapter 5. The solution is clearly dominated by a large communication overhead because of the communication of face values.

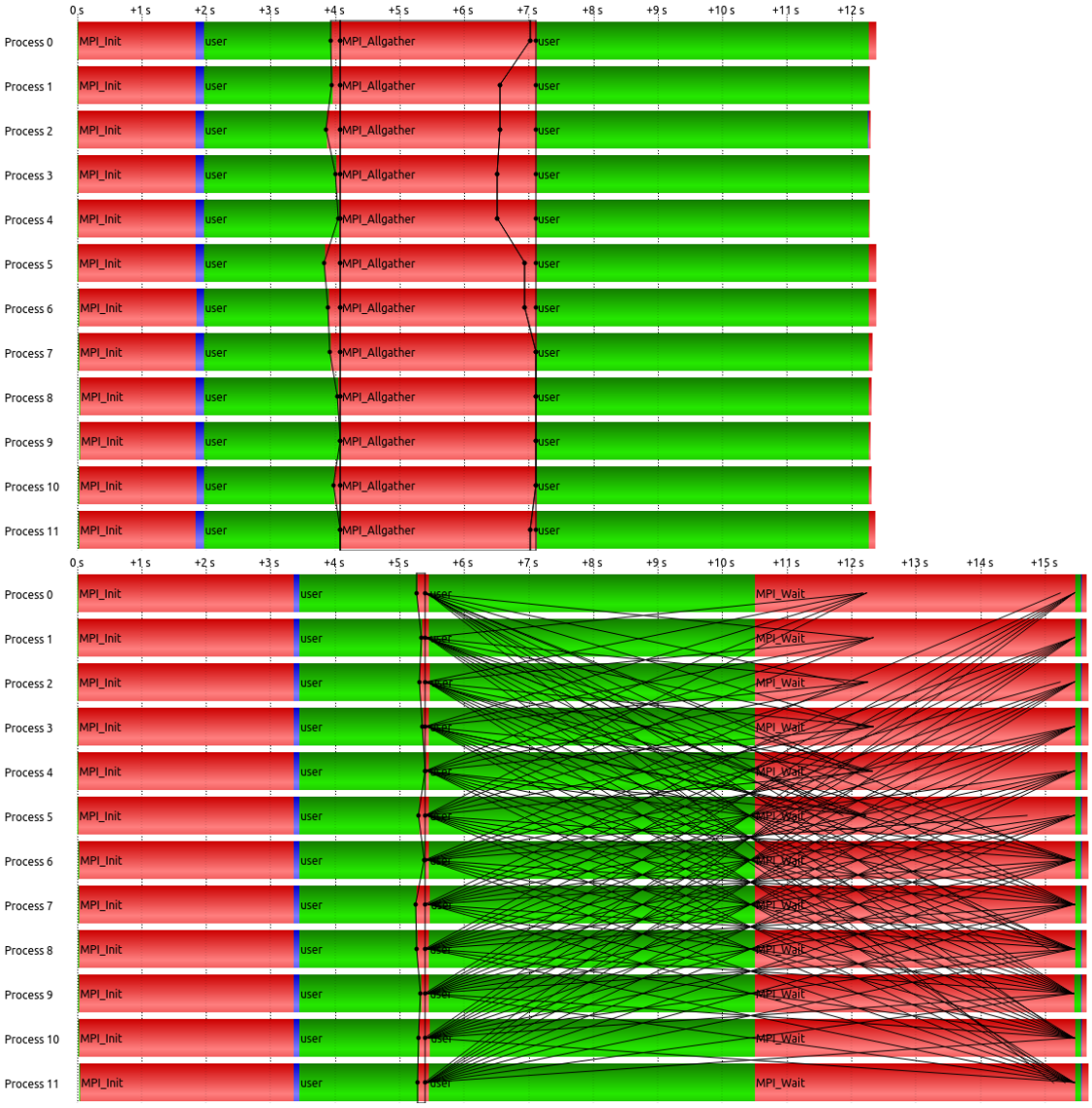

Figure 6.2: Comparison of the runtime of basic non-blocking and blocking MPI Communication with an independent grid sweep using 12 MPI task on 2 computational nodes. Each MPI task sends a message of 160 MB to each other task and sweeps a grid afterwards which is independent of the message data. *Top:* Using MPI_ALLGATHER to first communicate and sweep afterwards. *Bottom:* Using a series of 11 MPI_ISEND and MPI_IRECV to manually exchange data while simultaneously sweeping the grid. The non-blocking communication requires the call of the MPI_WAIT subroutine in the end to check for successful communication. Black lines in the bottom chart show the individual data exchanges between the task. MPI calls are marked in red, local computations are marked in green.

A Appendix

A.1 Accelerated Lambda Iteration

The lambda operator Λ describes the task to compute the radiation field from the source function. It is usually written as

$$J = \Lambda[S]. \tag{A.1}$$

Formally, we can solve this by inverting the lambda operator. When we arrange the cells of a 3D domain successively in a 1D vector, we can write the operator as a matrix. But the complete operator for *one cell* in the computational domain contains all radiative contributions from each other cell. Hence, the Lambda matrix is far from being sparse. The explicit construction and storage of the lambda matrix would easily reach computational limits in terms of memory requirements. Furthermore, the inversion of the Lambda operator is far too costly to be used in 3D radiative transfer. Instead, the formal solution (2.20) is used. Since the source function may depend on the mean intensity, this task requires iteration over Equations (2.18) to (2.20). This is called *lambda iteration* but it usually fails in optically thick regimes. This happens because photons can be trapped and scattered many times, if a single cell of the computational domain is

optically thick. The ordinary lambda iteration is not able to account for these processes on scales smaller than the spatial resolution.

The idea behind the accelerated lambda iteration (ALI), is to extract these sub-cell scattering contributions from the lambda operator (and hence from the iteration), because we are not able to resolve them anyway. The extracted part of the ordinary lambda operator is then put into a new *approximated* lambda operator, which is solved quasi-analytically. Since the approximated lambda operator usually only contains a small part of the whole lambda operator (the subgrid part so to say), it is easy to compute, store and solve. Mathematically, the lambda operator becomes split

$$\Lambda = (\Lambda - \Lambda^*) + \Lambda^*, \tag{A.2}$$

where Λ^* denotes the approximated lambda operator. Inserting this into equation A.1 and using the source function for isotropic scattering (Equation 4.3), we get

$$S = \epsilon B + (1 - \epsilon)(\Lambda - \Lambda^*)S + (1 - \epsilon)\Lambda^* S. \tag{A.3}$$

Since the Λ^*-operator consists of only a small part of the whole lambda-operator, it is sparse and easy to solve. We bring it on the left-hand side

$$[1 - (1 - \epsilon)\Lambda^*]S = \epsilon B + (1 - \epsilon)(\Lambda - \Lambda^*)S. \tag{A.4}$$

We introduce the iteration scheme, because there is still a contribution of the source function on the right-hand side. This remaining contribution can be regarded as the non-local contribution of the radiation field, which is solved by iteration. Inverting the approximated lambda-operator then yields

$$S^{n+1} = [1 - (1 - \epsilon)\Lambda^*]^{-1}(\epsilon B + (1 - \epsilon)(\Lambda - \Lambda^*)S^n). \tag{A.5}$$

The scheme in Equation A.5 is a combination of iteration and analytic solution. The non-local contributions (in the lambda matrix $(\Lambda - \Lambda^*)$) are accounted for by iteration while the local subgrid scattering is handled by an inversion of the approximated lambda operator (Λ^*). The computational cost of the inversion of the Λ^*-operator depends on its bandwidth, which determines the range on which we solve analytically. Obviously, a diagonal Λ^* is trivial to invert. But since the diagonal part of the lambda operator describes only the local scattering in a single cell, it is not the best choice in terms of iterative performance. Usually, a tri-diagonal operator yields the best compromise between fast convergence and computational cost. But this requires the solu-

tion of a coupled set of linear equations, which is complex to implement. For now, we stay with a diagonal local Λ^*-operator, since it is the easiest one to implement and still has a tremendous effect on the convergence rate.

Acknowledgments

Most of all, I want to thank my supervisor Prof. Dr. Robi Banerjee for his support, guidance, help and patience during this work.
I am also very thankful to Prof. Dr. Peter Hauschildt and Prof. Dr. Stefan Dreizler, my additional supervisors of the Graduiertenkolleg 1351.
Furthermore, I would like to thank Dr. Thomas Peters at the ETH Zürich and Mikhail Klassen at the McMaster University in Hamilton for very helpful discussions on the details of the code develompment for this work.
Many thanks also go to my colleagues Daniel Seifried and Bastian Körtgen for discussions on the FLASH code and my office mate Gunther Lukat for lively debates on code parallelization.

Special thanks belong to my family and friends, who never let me down and always encouraged me, not only during the last three years.

Bibliography

Acreman, D. M., Harries, T. J., and Rundle, D. A. (2010). Modelling circumstellar discs with three-dimensional radiation hydrodynamics. *MNRAS*, 403:1143–1155.

Amanatides, J. and Woo, A. (1987). A fast voxel traversal algorithm for ray tracing. In *In Eurographics '87*, pages 3–10.

Banerjee, R. and Pudritz, R. E. (2006). Outflows and jets from collapsing magnetized cloud cores. *ApJ*, 641:949–+.

Banerjee, R., Pudritz, R. E., and Holmes, L. (2004). The formation and evolution of protostellar discs; three-dimensional adaptive mesh refinement hydrosimulations of collapsing, rotating Bonnor-Ebert spheres. *MNRAS*, 355:248–272.

Bate, M. R. (2009). The importance of radiative feedback for the stellar initial mass function. *MNRAS*, 392:1363–1380.

Bate, M. R., Bonnell, I. A., and Price, N. M. (1995). Modelling accretion in protobinary systems. *MNRAS*, 277:362–376.

Bate, M. R., Tricco, T. S., and Price, D. J. (2013). Collapse of a molecular cloud core to stellar densities: stellar-core and outflow formation in radiation magnetohydrodynamic simulations. *MNRAS*.

Bjorkman, J. E. and Wood, K. (2001). Radiative Equilibrium and Temperature Correction in Monte Carlo Radiation Transfer. *ApJ*, 554:615–623.

Bodenheimer, P. (2011). *Principles of Star Formation*. Springer-Verlag Berlin Heidelberg 2011.

Bolton, C. T. (1972). Identification of Cygnus X-1 with HDE 226868. *Nature*, 235:271–273.

Boss, A. P. and Bodenheimer, P. (1979). Fragmentation in a rotating protostar - A comparison of two three-dimensional computer codes. *ApJ*, 234:289–295.

Bryan, G. L., Norman, M. L., O'Shea, B. W., Abel, T., Wise, J. H., Turk, M. J., Reynolds, D. R., Collins, D. C., Wang, P., Skillman, S. W., Smith, B., Harkness, R. P., Bordner, J., Kim, J.-h., Kuhlen, M., Xu, H., Goldbaum, N., Hummels, C., Kritsuk, A. G., Tasker, E., Skory, S., Simpson, C. M., Hahn, O., Oishi, J. S., So, G. C., Zhao, F., Cen, R., Li, Y., and The Enzo Collaboration (2014). ENZO: An Adaptive Mesh Refinement Code for Astrophysics. *ApJS*, 211:19.

Castor, J. I. (2007). *Radiation Hydrodynamics*.

Chiang, E. I. and Goldreich, P. (1997). Spectral Energy Distributions of T Tauri Stars with Passive Circumstellar Disks. *ApJ*, 490:368.

Colella, P. and Woodward, P. R. (1984). The Piecewise Parabolic Method (PPM) for Gas-Dynamical Simulations. *Journal of Computational Physics*, 54:174–201.

Commerçon, B., Teyssier, R., Audit, E., Hennebelle, P., and Chabrier, G. (2011). Radiation hydrodynamics with adaptive mesh refinement and application to prestellar core collapse. I. Methods. *A&A*, 529:A35+.

Courant, R., Friedrichs, K., and Lewy, H. (1928). Über die partiellen Differenzengleichungen der mathematischen Physik. *Mathematische Annalen*, 100:32–74.

Dapp, W. B., Basu, S., and Kunz, M. W. (2011). Bridging the gap: disk formation in the Class 0 phase with ambipolar diffusion and Ohmic dissipation. *ArXiv e-prints*.

Davis, S. W., Stone, J. M., and Jiang, Y.-F. (2012). A Radiation Transfer Solver for Athena Using Short Characteristics. *ApJS*, 199:9.

Duffin, D. F. and Pudritz, R. E. (2008). Simulating hydromagnetic processes in star formation: introducing ambipolar diffusion into an adaptive mesh refinement code. *MNRAS*, 391:1659–1673.

Dullemond, C. P. (2002). The 2-D structure of dusty disks around Herbig Ae/Be stars. I. Models with grey opacities. *A&A*, 395:853–862.

Dullemond, C. P. (2012). RADMC-3D: A multi-purpose radiative transfer tool. Astrophysics Source Code Library.

Dullemond, C. P. and Monnier, J. D. (2010). The Inner Regions of Protoplanetary Disks. *ARA&A*, 48:205–239.

Evans, II, N. J., Dunham, M. M., Jørgensen, J. K., Enoch, M. L., Merín, B., van Dishoeck, E. F., Alcalá, J. M., Myers, P. C., Stapelfeldt, K. R., Huard, T. L., Allen, L. E., Harvey, P. M., van Kempen, T., Blake, G. A., Koerner, D. W., Mundy, L. G., Padgett, D. L., and Sargent, A. I. (2009). The Spitzer c2d Legacy Results: Star-Formation Rates and Efficiencies; Evolution and Lifetimes. *ApJS*, 181:321–350.

Federrath, C., Banerjee, R., Clark, P. C., and Klessen, R. S. (2010). Modeling Collapse and Accretion in Turbulent Gas Clouds: Implementation and Comparison of Sink Particles in AMR and SPH. *ApJ*, 713:269–290.

Federrath, C., Clark, P. C., Banerjee, R., and Klessen, R. S. (2009). Implementation of Sink Particles in the FLASH Code. *in preparation*.

Flock, M., Fromang, S., González, M., and Commerçon, B. (2013). Radiation magnetohydrodynamics in global simulations of protoplanetary discs. *A&A*, 560:A43.

Forgan, D. and Rice, K. (2013). The possibility of a self-gravitating disc around L1527 IRS? *MNRAS*, 433:1796–1801.

Fryxell, B., Olson, K., Ricker, P., Timmes, F. X., Zingale, M., Lamb, D. Q., MacNeice, P., Rosner, R., Truran, J. W., and Tufo, H. (2000). FLASH: An Adaptive Mesh Hydrodynamics Code for Modeling Astrophysical Thermonuclear Flashes. *ApJS*, 131:273–334.

Goodman, A. A., Benson, P. J., Fuller, G. A., and Myers, P. C. (1993). Dense cores in dark clouds. VIII - Velocity gradients. *ApJ*, 406:528–547.

Górski, K. M., Hivon, E., Banday, A. J., Wandelt, B. D., Hansen, F. K., Reinecke, M., and Bartelmann, M. (2005). HEALPix: A Framework for High-Resolution Discretization and Fast Analysis of Data Distributed on the Sphere. *ApJ*, 622:759–771.

Harries, T. J. (2011). An algorithm for Monte Carlo time-dependent radiation transfer. *MNRAS*, 416:1500–1508.

Hartmann, L., Calvet, N., Gullbring, E., and D'Alessio, P. (1998). Accretion and the Evolution of T Tauri Disks. *ApJ*, 495:385.

Hayek, W., Asplund, M., Carlsson, M., Trampedach, R., Collet, R., Gudiksen, B. V., Hansteen, V. H., and Leenaarts, J. (2010). Radiative transfer with scattering for domain-decomposed 3D MHD simulations of cool stellar atmospheres. Numerical methods and application to the quiet, non-magnetic, surface of a solar-type star. *A&A*, 517:A49.

Heinemann, T., Dobler, W., Nordlund, Å., and Brandenburg, A. (2006). Radiative transfer in decomposed domains. *A&A*, 448:731–737.

Hennebelle, P. and Fromang, S. (2008). Magnetic processes in a collapsing dense core. I. Accretion and ejection. *A&A*, 477:9–24.

Hewish, A. (1970). Pulsars. *ARA&A*, 8:265.

Jack, D., Hauschildt, P. H., and Baron, E. (2012). A 3D radiative transfer framework. IX. Time dependence. *A&A*, 546:A39.

Jiang, Y.-F., Stone, J. M., and Davis, S. W. (2012). A Godunov Method for Multidimensional Radiation Magnetohydrodynamics Based on a Variable Eddington Tensor. *ApJS*, 199:14.

Kolb, S. M., Stute, M., Kley, W., and Mignone, A. (2013). Radiation hydrodynamics integrated in the PLUTO code. *A&A*, 559:A80.

Kolmogorov, A. (1941). The Local Structure of Turbulence in Incompressible Viscous Fluid for Very Large Reynolds' Numbers. *Akademiia Nauk SSSR Doklady*, 30:301–305.

Krumholz, M. R., Klein, R. I., and McKee, C. F. (2007a). Radiation-Hydrodynamic Simulations of Collapse and Fragmentation in Massive Protostellar Cores. *ApJ*, 656:959–979.

Krumholz, M. R., Klein, R. I., McKee, C. F., and Bolstad, J. (2007b). Equations and Algorithms for Mixed-frame Flux-limited Diffusion Radiation Hydrodynamics. *ApJ*, 667:626–643.

Kuiper, R., Klahr, H., Beuther, H., and Henning, T. (2012). On the stability of radiation-pressure-dominated cavities. *A&A*, 537:A122.

Kuiper, R., Klahr, H., Dullemond, C., Kley, W., and Henning, T. (2010). Fast and accurate frequency-dependent radiation transport for hydrodynamics simulations in massive star formation. *A&A*, 511:A81.

Larson, R. B. (1969). Numerical calculations of the dynamics of collapsing proto-star. *MNRAS*, 145:271–+.

Levermore, C. D. and Pomraning, G. C. (1981). A flux-limited diffusion theory. *ApJ*, 248:321–334.

Li, Z.-Y., Banerjee, R., Pudritz, R. E., Jørgensen, J. K., Shang, H., Krasnopolsky, R., and Maury, A. (2014). The Earliest Stages of Star and Planet Formation: Core Collapse, and the Formation of Disks and Outflows. *ArXiv e-prints*.

Lowrie, R. B. and Edwards, J. D. (2008). Radiative shock solutions with grey nonequilibrium diffusion. *Shock Waves*, 18:129–143.

Lucy, L. B. (1999). Computing radiative equilibria with Monte Carlo techniques. *A&A*, 344:282–288.

Lynden-Bell, D. and Pringle, J. E. (1974). The evolution of viscous discs and the origin of the nebular variables. *MNRAS*, 168:603–637.

Machida, M. N., Inutsuka, S.-i., and Matsumoto, T. (2010). Formation Process of the Circumstellar Disk: Long-term Simulations in the Main Accretion Phase of Star Formation. *ApJ*, 724:1006–1020.

Masunaga, H., Miyama, S. M., and Inutsuka, S.-I. (1998). A Radiation Hydrodynamic Model for Protostellar Collapse. I. The First Collapse. *ApJ*, 495:346.

Matthews, T. A. and Sandage, A. R. (1963). Optical Identification of 3c 48, 3c 196, and 3c 286 with Stellar Objects. *ApJ*, 138:30.

Mellon, R. R. and Li, Z. (2008). Magnetic Braking and Protostellar Disk Formation: The Ideal MHD Limit. *ApJ*, 681:1356–1376.

Mihalas, D. and Weibel Mihalas, B. (1984). *Foundations of radiation hydrodynamics*. New York: Oxford University Press, 1984.

Min, M., Dullemond, C. P., Dominik, C., de Koter, A., and Hovenier, J. W. (2009). Radiative transfer in very optically thick circumstellar disks. *A&A*, 497:155–166.

Mitalas, R. and Sills, K. R. (1992). On the photon diffusion time scale for the sun. *ApJ*, 401:759.

Offner, S. S. R., Klein, R. I., McKee, C. F., and Krumholz, M. R. (2009). The Effects of Radiative Transfer on Low-Mass Star Formation. *ApJ*, 703:131–149.

Olson, G. L., Auer, L. H., and Buchler, J. R. (1986). A rapidly convergent iterative solution of the non-LTE line radiation transfer problem. *J. Quant. Spec. Radiat. Transf.*, 35:431–442.

Olson, K. M., MacNeice, P., Fryxell, B., Ricker, P., Timmes, F. X., and Zingale, M. (1999). PARAMESH: A Parallel, Adaptive Mesh Refinement Toolkit and Performance of the ASCI/FLASH code. *Bulletin of the American Astronomical Society*, 31:1430–+.

Pascucci, I., Wolf, S., Steinacker, J., Dullemond, C. P., Henning, T., Niccolini, G., Woitke, P., and Lopez, B. (2004). The 2D continuum radiative transfer problem. Benchmark results for disk configurations. *A&A*, 417:793–805.

Penzias, A. A. and Wilson, R. W. (1965). A Measurement of Excess Antenna Temperature at 4080 Mc/s. *ApJ*, 142:419–421.

Peters, T., Banerjee, R., Klessen, R. S., Mac Low, M., Galván-Madrid, R., and Keto, E. R. (2010). H II Regions: Witnesses to Massive Star Formation. *ApJ*, 711:1017–1028.

Peters, T., Banerjee, R., Klessen, R. S., and Mac Low, M.-M. (2011). The Interplay of Magnetic Fields, Fragmentation, and Ionization Feedback in High-mass Star Formation. *ApJ*, 729:72–+.

Price, D. J. and Bate, M. R. (2010). Magnetic fields and radiative feedback in the star formation process. In Bertin, G., de Luca, F., Lodato, G., Pozzoli, R., and Romé, M., editors, *American Institute of Physics Conference Series*, volume 1242 of *American Institute of Physics Conference Series*, pages 205–218.

Rijkhorst, E.-J., Plewa, T., Dubey, A., and Mellema, G. (2006). Hybrid characteristics: 3D radiative transfer for parallel adaptive mesh refinement hydrodynamics. *A&A*, 452:907–920.

Roe, P. L. (1981). Approximate Riemann Solvers, Parameter Vectors, and Difference Schemes. *Journal of Computational Physics*, 43:357–372.

Rosdahl, J., Blaizot, J., Aubert, D., Stranex, T., and Teyssier, R. (2013). RAMSES-RT: radiation hydrodynamics in the cosmological context. *MNRAS*, 436:2188–2231.

Santos-Lima, R., de Gouveia Dal Pino, E. M., and Lazarian, A. (2012). The Role of Turbulent Magnetic Reconnection in the Formation of Rotationally Supported Protostellar Disks. *ApJ*, 747:21.

Seifried, D., Banerjee, R., Klessen, R. S., Duffin, D., and Pudritz, R. E. (2011). Magnetic fields during the early stages of massive star formation - I. Accretion and disc evolution. *MNRAS*, 417:1054–1073.

Seifried, D., Banerjee, R., Pudritz, R. E., and Klessen, R. S. (2012). Disc formation in turbulent massive cores: circumventing the magnetic braking catastrophe. *MNRAS*, 423:L40–L44.

Seifried, D., Banerjee, R., Pudritz, R. E., and Klessen, R. S. (2013). Turbulence-induced disc formation in strongly magnetized cloud cores. *MNRAS*, 432:3320–3331.

Sekora, M. D. and Stone, J. M. (2010). A hybrid Godunov method for radiation hydrodynamics. *Journal of Computational Physics*, 229:6819–6852.

Semenov, D., Henning, T., Helling, C., Ilgner, M., and Sedlmayr, E. (2003). Rosseland and Planck mean opacities for protoplanetary discs. *A&A*, 410:611–621.

Shakura, N. I. and Sunyaev, R. A. (1973). Black holes in binary systems. Observational appearance. *A&A*, 24:337–355.

Sod, G. A. (1978). A survey of several finite difference methods for systems of nonlinear hyperbolic conservation laws. *Journal of Computational Physics*, 27:1–31.

Springel, V., White, S. D. M., Jenkins, A., Frenk, C. S., Yoshida, N., Gao, L., Navarro, J., Thacker, R., Croton, D., Helly, J., Peacock, J. A., Cole, S., Thomas, P., Couchman, H., Evrard, A., Colberg, J., and Pearce, F. (2005). Simulations of the formation, evolution and clustering of galaxies and quasars. *Nature*, 435:629–636.

Stone, J. M., Mihalas, D., and Norman, M. L. (1992). ZEUS-2D: A radiation magnetohydrodynamics code for astrophysical flows in two space dimensions. III - The radiation hydrodynamic algorithms and tests. *ApJS*, 80:819–845.

Tobin, J. J., Hartmann, L., Chiang, H.-F., Wilner, D. J., Looney, L. W., Loinard, L., Calvet, N., and D'Alessio, P. (2012). A ˜0.2-solar-mass protostar with a Keplerian disk in the very young L1527 IRS system. *Nature*, 492:83–85.

Toomre, A. (1964). On the gravitational stability of a disk of stars. *ApJ*, 139:1217–1238.

Toro, E. F. (2009). *Riemann Solvers and Numerical Methods for Fluid Dynamics*. Springer, 2009.

Truelove, J. K., Klein, R. I., McKee, C. F., Holliman, J. H., Howell, L. H., and Greenough, J. A. (1997). The Jeans Condition: A New Constraint on Spatial Resolution in Simulations of Isothermal Self-gravitational Hydrodynamics. *ApJ*, 489:L179+.

Trujillo Bueno, J. and Fabiani Bendicho, P. (1995). A Novel Iterative Scheme for the Very Fast and Accurate Solution of Non-LTE Radiative Transfer Problems. *ApJ*, 455:646.

van Noort, M., Hubeny, I., and Lanz, T. (2002). Multidimensional Non-LTE Radiative Transfer. I. A Universal Two-dimensional Short-Characteristics Scheme for Cartesian, Spherical, and Cylindrical Coordinate Systems. *ApJ*, 568:1066–1094.

Vogelsberger, M., Genel, S., Springel, V., Torrey, P., Sijacki, D., Xu, D., Snyder, G., Bird, S., Nelson, D., and Hernquist, L. (2014). Properties of galaxies reproduced by a hydrodynamic simulation. *Nature*, 509:177–182.

Whitehouse, S. C. and Bate, M. R. (2006). The thermodynamics of collapsing molecular cloud cores using smoothed particle hydrodynamics with radiative transfer. *MNRAS*, 367:32–38.

Yorke, H. W., Bodenheimer, P., and Laughlin, G. (1993). The formation of protostellar disks. I - 1 M(solar). *ApJ*, 411:274–284.

Zhang, Y., Tan, J. C., and McKee, C. F. (2013). Radiation Transfer of Models of Massive Star Formation. II. Effects of the Outflow. *ApJ*, 766:86.

Zinnecker, H. and Yorke, H. W. (2007). Toward Understanding Massive Star Formation. *ARA&A*, 45:481–563.

Eidesstattliche Versicherung

Hiermit erkläre ich an Eides statt, dass ich die vorliegende Dissertationsschrift selbst verfasst und keine anderen als die angegebenen Quellen und Hilfsmittel benutzt habe.

Hamburg, den 01.10.2015 Unterschrift